Propagation de fissures dans des milieux élastiques avec énergie de surface anisotrope : expériences, simulations de champ de phase et mécanique de la rupture élastique linéaire

Xinyuan Zhai

INSTITUT POLYTECHNIQUE DE PARIS

ENSTA IP PARIS

NNT : 2023IPPAE010

Thèse de doctorat

Crack propagation in elastic media with anisotropic fracture toughness : experiments and numerical modeling

Thèse de doctorat de l'Institut Polytechnique de Paris
préparée à l'ENSTA Paris

École doctorale n°626 l'Institut Polytechnique de Paris (ED IP Pairs)
Spécialité de doctorat : Mécanique des fluides et des solides, acoustique

Thèse présentée et soutenue à Palaiseau, le 07 Décembre 2023, par

Xinyuan ZHAI

Composition du Jury :

Fabien Szmytka Professeur, ENSTA Paris	Président
Corrado Maurini Professeur, Sorbonne-Université	Rapporteur
Benoit Roman Directeur de Recherche, ESPCI Paris	Rapporteur
Jeremy Bleyer Chargé de recherche, École nationale des ponts et chaussées	Examinateur
Véronique Lazarus Professeure, ENSTA Paris	Directrice de thèse
Stella Brach Chargée de recherche, IBM Zurich	Co-encad. de thèse
Thomas Corre Ingénieur de recherche, École Centrale de Nantes	Invité
Andrés A. León Baldelli Chargé de recherche, CNRS	Invité (Co-encad.)

Dedicated to my parents and my grandmother.

" When nothing seems to help, I go and look at a stone-cutter hammering away at his rock perhaps a hundred times without as much as a crack showing in it. Yet at the hundred and first blow it will split in two, and I know it was not that blow that did it – but all that had gone before." – Jacob Riis

Acknowledgements

First of all, I would like to thank my supervisor for accepting me as her graduate intern and PhD student. Over the past three and a half years, she has been extremely supportive and encouraging in every way. I am not a very confident person and often self-doubt. At the beginning of my PhD program, I did not know how to carry out my research work. Especially in the weekly meetings, I had a hard time presenting my research progress clearly. My supervisor patiently guided me from the beginning, whether it was writing a report or participating in a discussion, she would always make suggestions for improvement. She took the trouble to review and provide feedback time and time again. She provided significant help and encouragement when my work seemed to be stagnating. Without her support, it would not have been possible to complete this thesis.

I would like to thank Thomas Corre, a former postdoc in our group, who built most of the experimental platforms and patiently taught me how to use them. As the old Chinese saying goes, "One generation plants the trees, and the next enjoys the shade." Thanks to his dedication and help, at my early stage of PhD, especially the experimental work, went smoothly. When I encountered problems, especially when things did not go well in the initial group meetings, he would take time out a day in advance to help me rehearse and suggest improvements. This has benefited me greatly.

I would also like to thank my two other advisors, Andrés León Baldelli and Stella Brach, for their invaluable help with phase field simulation. My first exposure to phase field simulation was during the graduate program course given by Andrés, and it was his course that sparked my strong interest in this field. Also, since this was my first exposure to simulation, Stella provided a lot of helpful advice on the details and guided my research in the right direction.

In addition, I would like to thank David Roucou, the current postdoc in our group, for his frequent discussions, listening to my problems, and providing valuable advice. I would also like to thank Julie Triclot and Jean-Michel Scherer for their help with my experimental and numerical work.

I would like to thank the contributions of my research collaborators at Northeastern University, Prof Alain Karma and Dr Ataollah Mesgarnejad whose collaboration and expertise greatly enhanced the depth of this study.

I would also like to thank my thesis committee members Prof. Corrado Maurini, Prof. Benoit Roman, Prof. Fabien Szmytka and Prof. Jeremy Bleyer. I am honored to have them as reviewers and jury members of my thesis. I would like to thank them for their valuable comments and constructive criticism, which greatly improved the quality of this thesis.

I would like to express my gratitude to all the faculty, staff, PhD students and postdocs at IMSIA. Nicolas Thurieau, thank you for your support in the use of experimental equipment. Baris Telmen, thank you for your support in the use of the server. Thierry Pichon, thank you for in both software and hardware. Cécile Callo-labbe and Catherine Prieur, thank you for your help with travel arrangements and related administrative procedures. Lahcène Cherfa, thank you for your help with sample processing. Abdelfattah Halim, thank you for your help with the server MecaMat. Habibou MAITOURNAM and Yongjun HE, thank you for the advice and concern. Louis David, Sébastien Ballésio, Élodie Doyen, Xiaofei Ju, Chengguan Zhang, Silin Fu, Xiang Zhang, Yikun Yang and Shuaichen Guo, I'm delighted to have shared these three years with all of you.

I want to thank my closest friends, Haotian Zeng, Fengming Guo and Jiaheng Ruan, who have consistently listened to my concerns and provided me with emotional support.

Finally, I would like to thank my parents for your unconditional support all along. I would like to thank my girlfriend Qiqi Tao for her constant companionship and enduring my temper. Also, I would like to thank my two cats, Sunny and Sven for helping me relieve stress and maintain mental health.

Résumé

La prévention des défaillances structurelles dues à des défauts de fabrication est une préoccupation majeure en ingénierie. Pour mieux comprendre la propagation des fissures dans les structures ou les solides et éviter les effondrements, il est essentiel d'étudier l'impact de la microstructure sur la propagation des fissures. Les progrès en science des matériaux et en technologie de fabrication ont élargi la gamme de matériaux disponibles, notamment les matériaux composites, les matériaux structurels, les méta-matériaux et les matériaux poreux. Ces avancées ont également rendu possible la modification de la microstructure par divers processus de fabrication. En conséquence, un nombre croissant d'études ont été menées pour comprendre l'impact des changements microstructuraux sur la sélection du trajet de la fissure.

Une avancée notable dans la technologie de fabrication est la fabrication additive, qui gagne en popularité dans diverses industries. La fabrication additive offre une flexibilité de conception et la possibilité de modifier les microstructures grâce à la technologie d'impression. Elle remplace progressivement les processus de fabrication traditionnels pour des composants spécifiques ayant des exigences uniques dans de nombreux domaines. L'utilisation croissante de la fabrication additive dans diverses industries a conduit à des recherches approfondies sur l'impact des paramètres d'impression sur les propriétés des matériaux, avec une attention particulière portée à l'amélioration de la résistance des matériaux et de la ténacité à la rupture pour prévenir l'amorçage des fissures. Cependant, du point de vue de l'ingénierie, il est tout aussi crucial de comprendre comment la fissure se propage, car cette connaissance peut orienter la conception structurelle et faciliter le contrôle de l'extension de la fissure dans des directions souhaitées. Malgré les progrès dans des études connexes, telles que l'étude des effets de différentes techniques ou stratégies d'impression sur l'extension et la sélection du chemin de la fissure, le domaine est encore en exploration.

Cette thèse explore la propagation des fissures dans des échantillons imprimés présentant une isotropie en élasticité et une anisotropie en ténacité à la rupture. Nous avons utilisé une combinaison d'approches expérimentales, numériques et théoriques pour examiner la sélection des trajets de fissure dans des échantillons de Polycarbonate fabriqués

par dépôt de fil fondu.

Pour la partie expérimentale, en adoptant le motif d'impression en croix, l'échantillon imprimé présente un comportement de rupture anisotrope. Après une procédure de pré-fissuration, nous avons réalisé des expériences de rupture sous des conditions de chargement en Mode I et Mode I+II en utilisant des échantillons de Compact tension et des échantillons Compact tension shear. À travers l'examen des résultats expérimentaux, nous avons déduit l'existence d'une direction interdite dans notre échantillon imprimé, comme en témoigne la propagation cohérente de la fissure le long de la direction d'impression. À un niveau microscopique, la propagation de la fissure se produit en raison de la rupture de la jonction fondue entre deux fils adjacents parallèles. Nous avons utilisé la corrélation d'images pour déterminer l'energie de surface critique G_c de la 'plan faible' en utilisant le facteur d'intensité de contrainte mesuré après le déviation de la fissure. De plus, nous avons noté que la direction d'impression influence également de manière significative la charge critique associée au comportement de rupture.

Pour mieux comprendre l'influence microstructurale sur le comportement de rupture, la modélisation de champ de phase de la rupture fragile est utilisée comme méthode numérique dans cette thèse. Le modèle de champ de phase a gagné en popularité dans la communauté de la rupture computationnelle en raison de son efficacité et de sa fiabilité dans la simulation de la nucléation et de la propagation des fissures. De plus, sa polyvalence pour incorporer divers mécanismes de rupture, y compris le comportement de rupture anisotrope, en fait un outil très souhaitable pour cette étude. Malgré les progrès rapides dans l'application numérique du modèle de champ de phase, plusieurs questions controversées restent à étudier et à discuter. L'une des questions les plus importantes est le choix du paramètre de régularisation ℓ dans le modèle de champ de phase.

Pour répondre à cette question, nous commençons d'abord par le modèle de champ de phase isotrope et faiblement anisotrope (modèle de champ de phase d'ordre deux), en comparant les prédictions du trajet de fissure numérique et de la charge critique associée aux données expérimentales de la littérature pertinente. Les résultats des prédictions numériques ont montré une bonne concordance avec les données expérimentales fournies. La validation du modèle de champ de phase AT1 revêt une importance significative, car elle sert de transition en douceur vers le modèle de champ de phase d'ordre supérieur. Du point de vue théorique, nous avons validé la procédure de prédiction du GMERR en comparant le chemin de fissure prédit et la contrainte critique avec des données expérimentales pertinentes.

Par la suite, nous avons utilisé un modèle de champ de phase d'ordre supérieur avec une énergie de surface fortement anisotrope pour simuler la propagation des fissures

dans nos échantillons imprimés. Nous avons commencé par calibrer les paramètres numériques, puis avons procédé à la comparaison du trajet de la fissure et de la force critique pertinente avec les résultats expérimentaux, révélant un degré notable d'accord entre les deux. Importamment, nous avons démontré que ces prédictions peuvent être efficacement réalisées grâce à l'application des critères GMERR dans le cadre de la mécanique de la rupture élastique linéaire. De plus, guidée par les résultats des enquêtes numériques, notre exploration s'est plongée dans une discussion sur la sélection du paramètre de régularisation ℓ dans le contexte du modèle de champ de phase. En menant des expériences numériques avec différentes géométries d'échantillons (compact tension et compact tension shear), nous avons constaté que la régularisation ℓ peut être reconnue comme une longueur interne du matériau qui est proche de la taille du fil imprimé.

Enfin, nous avons introduit une série d'investigations préliminaires visant à identifier des configurations d'échantillons appropriées pour observer la propagation de fissures en zig-zag. De plus, nous avons fait une découverte intrigante concernant les comportements de rupture divergents démontrés par les échantillons imprimés soumis à des conditions de chargement monotones et cycliques. Pour élucider davantage ce phénomène, nous avons utilisé un modèle de champ de phase de fatigue présentant une énergie de surface faiblement anisotrope, reproduisant avec succès les résultats expérimentaux et renforçant notre compréhension de ce comportement complexe.

Mots clés: Fabrication additive, Rupture, Champ de phase, Energies surface anisotropie

Introduction

Preventing structural failure due to manufacturing defects is a major concern in engineering. To better understand how crack propagates in structures or solids and prevent collapse, it is essential to study the impact of microstructure on crack propagation. Advancements in material science and manufacturing technology have expanded the range of available materials, including composite material, structural material, metamaterial, and porous materials. These advancements have also made it feasible to alter the microstructure through various manufacturing processes. As a result, a growing number of studies have been carried out to understand the impact of microstructural changes on crack path selection.

One notable advancement in manufacturing technology is Additive manufacturing (AM), which is gaining increasing popularity in various industries. AM offers design flexibility and the ability to modify microstructures through printing technology. It is gradually replacing traditional manufacturing processes for specific components with unique requirements in many fields. The growing utilization of AM in various industries has led to extensive research on the impact of printing parameters on material properties, with a predominant focus on enhancing material strength and fracture toughness to prevent crack initiation. However, from an engineering perspective, it is equally crucial to understand how crack propagates, as this knowledge can guide structural design and facilitate the control of crack extension in desired directions. Despite progress in related studies, such as studying the effects of different printing techniques or strategies on crack extension and crack path selection, the field is still being explored.

Recently, Corre and Lazarus 2021 reported a material printed by Fused Deposition Modeling (FDM) possess a strongly anisotropic fracture toughness, meanwhile it remains isotropy in elasticity. To illustrate this effect, they conducted experiments using two Tapered Double Cantilever Beam (TDCB) specimens printed in Polycarbonate (PC), one with a (0°/90°) deposit pattern and the other with a (+45°/-45°) criss-crossed deposit pattern, as shown in Figure 1. Interestingly, the crack propagation in the specimen with (0°/90°) deposit pattern was found to be stable and followed along the 0° direction, while

the crack propagation in the specimen with (+45°/-45°) deposit pattern was stable at first, following the 45° direction, but later became unstable and changed direction towards the perpendicular to the direction of loading. It is important to highlight that the printed PC specimens with a criss-cross pattern retained their brittleness and did not display the ductile fracture behavior observed in certain prior studies (Cantrell et al., 2017; Corre and Lazarus, 2021). This limited ductility was especially noticeable when the fill rate reached approximately 100 %, as the deformation of the thread was not discernible prior to failure. Instead, the stability of crack propagation and crack path selection were found to vary with different printing patterns. This finding has important implications for investigating the relationship between brittle fracture and microstructure.

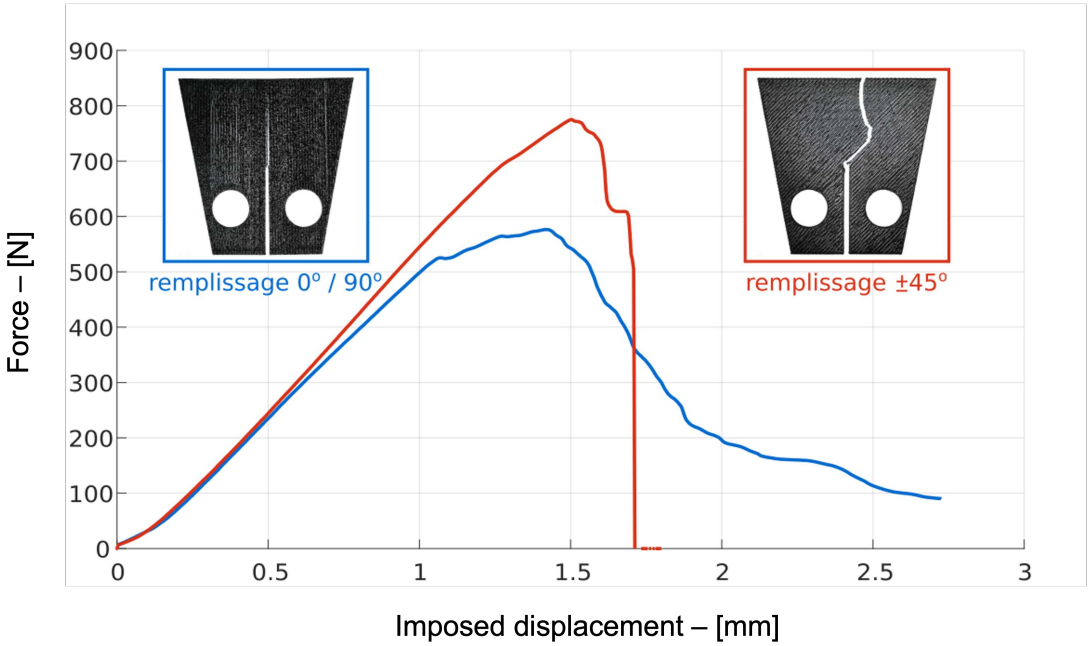

Figure 1 Loading curve and crack path in TDCB specimen with different microstucture obtained by FDM. (Corre and Lazarus 2021's experiments and image)

To gain a deeper understanding of the microstructural influence on brittle fracture behavior, the phase-field modeling of brittle fracture is employed as a numerical method in this dissertation. The phase-field model has gained popularity in the computational fracture community due to its efficiency and reliability in simulating crack nucleation and propagation. Moreover, its versatility in incorporating various fracture mechanisms, including anisotropic fracture behavior, makes it a highly desirable tool for this study. Despite the rapid progress in the numerical application of the phase-field model, several controversial issues remain to be studied and discussed. One of the most important issues is the choice of the regularization parameter ℓ in the phase-field model. Theoretically, as

ℓ approaches 0, the damage energy function in the phase-field model tends towards the Griffith-type brittle fracture model in a Gamma-convergence sens for both second order (Bourdin et al., 2000) and higher-order phase-field functionals (Burger et al., 2015; Negri, 2020)[1]. However, in numerical practice, ℓ is considered more than a common numerical parameter. It is often regarded as a material parameter or a physical internal length that relates to the critical force for crack nucleation. Whether ℓ can be denoted as an internal length is still being debated in the community (Pham et al., 2011; Tanné et al., 2018). Several studies have been carried out to address this issue accompany with experimental results, but research in this area is still ongoing.

Furthermore, when anisotropic fracture toughness is involved, the regularization parameter $\ell(\theta)$ may become orientation-dependent. This further complicates matters, as more numerical parameters need to be determined to take into account the anisotropic fracture toughness. To the best of our knowledge, there is a lack of research in this area.

This thesis aims to fill the gap by investigating the fracture behavior in elastic media with anisotropic fracture toughness using the phase-field model. The study is divided into two parts: experiments and numerical simulation. In the experimental part, we utilize the Fused Deposition Modeling method with a specific printing strategy to form a criss-cross printing pattern. Different specimen geometries will be used to investigate crack propagation under different loading conditions, including Mode I and Mode I+II. In the numerical part, we initially employed a finite element model based on classical approach to validate the experimentally measured Stress Intensity Factors. Then we adopt the phase-field modeling of brittle fracture based on a variational approach, using experimental data for calibrating and identification of the numerical parameters. With these comprehensive approaches, we aim at promoting a better understanding of the relation between printing pattern and crack path selection, which has significant implications for guiding and controlling crack extension in AM made parts. Besides, we adopted the classical based criteria Generalized Maximum Energy Release Rate to enhance our understanding of crack path selection and the relevant critical force.

This thesis is organized as follows: Chapter 1 is devoted to provide a comprehensive introduction to fracture mechanics, including the classical and variational approach to Linear Elastic Fracture Mechanics. Our objective is to discuss how the fracture issue was addressed through two distinct approaches, particularly focusing on evolution of crack propagation and selection of the crack path. We will subsequently present how to solve the fracture problem numerically through these two approaches, with particular

[1]It is important to note that this result holds only for isotropic surface energy, whether the result of Γ-convergence holds for anisotropic model requires further rigorous mathematical analysis.

emphasis on the occurrence of a kink resulting from the anisotropic fracture toughness.

Chapter 2 is devoted to the experimental investigation on fracture behavior of printed sample with anisotropic fracture toughness. The chapter begins by introducing the FDM process and reviewing relevant literature. Then the sample preparation, experimental setup and post-processing method are described in detail. Finally, the chapter presents the results of the fracture experiments conducted on different samples.

Chapter 3 is dedicated to the validation of the numerical implementations for the model based on both classic and variational approaches. To accomplish this, we compare the numerical results obtained through our implementation with experimental and theoretical results from literature. This allows us to validate the accuracy and reliability of our numerical implementation.

Chapter 4 presents the main results and discusses for various cases, including a comparison between experimental and numerical results for materials with different fracture anisotropic properties under various loading conditions. The chapter highlights the ability of the phase-field model to predict crack trajectories and relevant critical force for crack propagation, and also discusses the selection of numerical parameters, particularly the regularization parameter ℓ in the phase-field model with strongly anisotropic surface energy.

Chapter 5, we shift our attention to some preliminary investigations regarding the potential emergence of a Zig-Zag crack pattern in 3D printed specimens. This study involves conducting numerical simulations on various sample geometries to explore this phenomenon. Furthermore, we delve deeper into the fracture behavior of the printed specimens under cyclic loading, presenting a comprehensive comparison between experimental observations and numerical predictions.

Finally, we conclude the thesis by summarizing the findings and offering future research perspectives.

Contents

List of Figures

Nomenclature

List of symbols

$\boldsymbol{u}$	Displacement
$[\![\boldsymbol{u}]\!]$	Jump of the displacement
Γ	Crack set
$\boldsymbol{n}$	Normal vector
$\underset{\sim}{\boldsymbol{\sigma}}$	Stress tensor
$\underset{\sim}{\boldsymbol{\varepsilon}}$	Strain tensor
$\mathbb{A}$	Stiffness tensor
$\mathbb{S}$	Compliance tensor
$\partial_D\Omega$	Dirichlet region
f	Volumetric force
$\boldsymbol{T}^d$	Surface force
$\partial_N\Omega$	Neumann region
G	Energy release rate
$\mathcal{E}_p$	Potential energy
l	Created crack surface
K_I, K_{II}, K_{III}	Stress intensity factors of three modes
T	T-stress

κ	Kolossov's constant
ν	Poisson's ratio
μ	Shear modulus
E	Young's modulus
K_q	Stress intensity factor before kinking
$K_p(s, \varphi)$	Stress intensity factor after kinking with kink length s and kink angle φ
$F_{pq}(\varphi), G_p(\varphi)$	Universal function depend on the kink angle φ
$G(\varphi)$	Energy release rate for all potential direction
K_{IC}	Fracture toughness of the material (Mode I)
G_C	Critical energy release rate
$\mathcal{E}(\boldsymbol{u}, \Gamma)$	Total energy
$\mathcal{E}_s(\Gamma)$	Surface energy
$\mathcal{H}^{n-1}(\Gamma)$	(n-1) dimensional Hausdroff measure of the crack
$S(\boldsymbol{u})$	Jump set of $\boldsymbol{u}$
$G_c(\theta)$	Orientation-dependent surface energy
$F_c(\theta)$	Critical force with crack direction θ
$\mathcal{L}$	Loading
$\hat{G}(\theta)$	Energy release rate in the direction θ at unit load $F = 1$
$\gamma(\boldsymbol{n}(\theta)$	Dimensionless functional of surface energy
$\underset{\sim}{\boldsymbol{E}}$	Eshelby tensor
W	Strain energy density
$\underset{\sim}{\boldsymbol{I}}$	Unit tensor
$\boldsymbol{\theta}(\boldsymbol{x})$	Fictitious velocity field

η	Virtual time variable
δ_{ij}	Kronecker delta
$u_i^{aux}, \sigma_{ij}^{aux}$	Displacement and stress auxiliary field
J^{aux}	$J-$integral of auxiliary field
$I^{(I)}, I^{(II)}$	Interaction integral of Mode I and Mode II
α	Damage variable
ℓ	Regularization parameter
$a(\alpha), w(\alpha)$	Stiffness modulation function and dissipation penitential
c_w	Normalization parameter
$\mathcal{C}, \mathcal{D}$	Set of admissible displacement and damage fields
A_t	Anisotropic indicator for two-fold symmetric model
G_0	Scaling factor of energy per unit surface
ℓ_0	Scaling factor of regularization parameter
$\mathbb{C}$	Anisotropic surface energy tensor
A_f	Anisotropic coefficient for four-fold symmetric model
$\mathbb{K}$	Transformation matrix for fourth-order tensor
$\mathbb{A}(\alpha_i)$	Damage-degraded tensor
κ_r	Residual stiffness
β	Penalization parameter
$\underset{\sim}{\boldsymbol{B_i}}$	Second-order tensor correspond to different damage variable i
$\overline{K_I^*}, \overline{K_{II}^*}$	Average value of the SIFs of mode I and mode II after kinking
σ_c	Critical stress
h	Mesh size

θ_0	Material axis
f_v	Volume fraction of fibers in composite material

List of abbreviations

AM	Additive Manufacturing
FDM	Fused Deposition Modeling
LEFM	Linear Elastic Fracture Mechanics
TDCB	Tapered Double Cantilever Beam
PC	Polycarbonate
BVP	Boundary Value Problem
SIFs	Stress Intensity Factors
FPZ	Fracture Process Zone
CT	Compact Tension
SENB	Single Edge Notch Bend
MTS	Maximum Tangential Stress criterion
SED	Strain Energy Density criterion
MER	Maximum Energy Release
PLS	Principle of Local Symmetry
SBV	Special functions with bounded variation
GMERR	Generalized Maximum Energy Release Rate
AMR	Adaptive Mesh Refinement
XFEM	Extend Finite Element Method
PLA	Polylactic acid
ABS	Acrylonitrile butadiene styrene
PA	Polyamide

CTS	Compact Tension Shear
DIC	Digital Image Correlation
ASTM	American Society for Testing and Materials
CN	Centred Notched
SEN	Single Edge Notch
PMMA	Polymethyl Methacrylate
COD	Crack Opening Displacement
MITC	Mixed Interpolation of Tensorial Components

Chapter 1

State of the art in Linear Elastic Fracture Mechanics

This chapter is devoted to the introduction of LEFM, including both classical approach and variational approach, spanning the transition from materials with isotropic fracture toughness to those exhibiting anisotropic fracture behavior. We aim to discuss how the problem of fracture was solved using these two different approaches, with a specific focus on the evolution of crack propagation and the determination of the crack path. Subsequently, we present numerical models derived from both approaches, dedicated to addressing isotropic and anisotropic fracture challenges.

Contents

1.1 Hypothesis of brittle fracture problem

Fracture mechanics is a field dedicated to the investigation and prediction of crack initiation and propagation in solid materials. Its roots trace back to the early 1920s, primarily focusing on the study of brittle materials. This led to the development of Linear Elastic Fracture Mechanics (LEFM), a sub-field that specifically examines the behavior of crack initiation and propagation in brittle solids under loading conditions. Subsequently, in the 1960s, the scope of fracture mechanics expanded to include ductile materials as well. In this dissertation, our primary focus is on the brittle fracture problem. In the following section, we will provide a concise overview of the assumptions and notation used in this study.

Brittle fracture refers to the phenomenon where a material undergoes cracking without experiencing substantial irreversible deformation. A crack is commonly represented as a narrow separation within a medium, resulting in discontinuous displacement surfaces. In a cracked solid, the displacements are permitted to be discontinuous across the crack, and the jump of the displacement $[\![\boldsymbol{u}]\!](\boldsymbol{x})$ at a specific position $\boldsymbol{x}$ located on a crack Γ is denoted as:

$$[\![\boldsymbol{u}]\!](\boldsymbol{x}) = \boldsymbol{u}^{+}(\boldsymbol{x}) - \boldsymbol{u}^{-}(\boldsymbol{x}), \quad \boldsymbol{x} \in \Gamma \tag{1.1}$$

Furthermore, we neglect the cohesive forces between the crack lips and assume that they are not in contact to avoid any overlapping phenomena:

$$[\![\boldsymbol{u}]\!] \cdot \boldsymbol{n} > 0, \text{ and } \underset{\sim}{\boldsymbol{\sigma}} \cdot \boldsymbol{n} = \boldsymbol{0} \tag{1.2}$$

where $\boldsymbol{n}$ is the normal vector to the crack lips. The second hypothesis is related to the constitutive behavior, where we assume that the material exhibits linear elastic behavior, the stress-strain relation can be described as follows:

$$\underset{\sim}{\boldsymbol{\sigma}} = \mathbb{A} : \underset{\sim}{\boldsymbol{\varepsilon}} \quad \text{or} \quad \underset{\sim}{\boldsymbol{\varepsilon}} = \mathbb{S} : \underset{\sim}{\boldsymbol{\sigma}} \tag{1.3}$$

where $\underset{\sim}{\boldsymbol{\sigma}}$ and $\underset{\sim}{\boldsymbol{\varepsilon}}$ are stress and strain tensor, respectively. $\mathbb{A}$ and $\mathbb{S}$ are stiffness tensor and compliance tensor, respectively. Additionally, we assume that the evolution of cracking in a solid subjected to a time-dependent load is quasi-static, ensuring that the solid remains in equilibrium under the current load and state of cracking. With these assumptions, we can determine the displacement field in equilibrium based on the current state of cracking and loading at each moment.

Consider a 2D body Ω with a known crack state Γ and subjected to a displacement

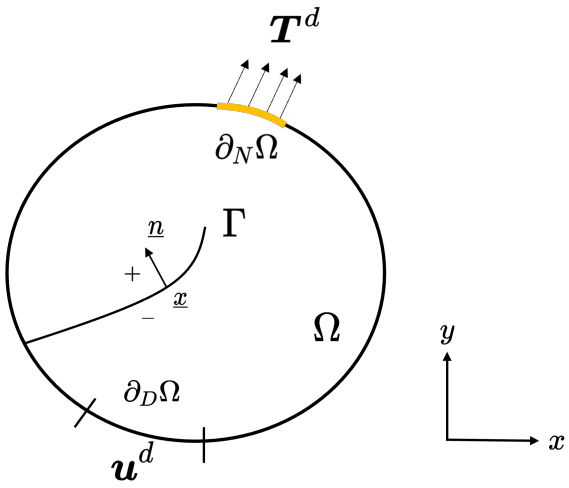

Figure 1.1 Boundary value problem

$\boldsymbol{u}^d$ on the Dirichlet region $\partial_D\Omega$. The volumetric force $\boldsymbol{f}$ acts within Ω, and the surface forces $\boldsymbol{T}^d$ are applied on the Neumann region $\partial_N\Omega$. $(\boldsymbol{u}^d, \boldsymbol{T}^d, \boldsymbol{f})$ are supposed to be applied in-plane. We solve the following Boundary Value Problem (BVP) to determine the unknowns ($\boldsymbol{u}$, $\underset{\sim}{\boldsymbol{\sigma}}$, $\underset{\sim}{\boldsymbol{\varepsilon}}$) combined with the boundary condition on the crack eq. (1.1) - (1.2):

1. **Equilibrium condition**: $\operatorname{div}\underset{\sim}{\boldsymbol{\sigma}} + \boldsymbol{f} = \boldsymbol{0} \quad \text{in} \quad \Omega\backslash\Gamma$

2. **The elasticity relationship**: $\underset{\sim}{\boldsymbol{\sigma}} = \mathbb{A} : \underset{\sim}{\boldsymbol{\varepsilon}} \quad \text{with} \quad 2\underset{\sim}{\boldsymbol{\varepsilon}} = \nabla\boldsymbol{u} + \nabla^T\boldsymbol{u} \quad \text{in} \quad \Omega\backslash\Gamma$

3. **Boundary conditions**: $\underset{\sim}{\boldsymbol{\sigma}} \cdot \boldsymbol{n} = \boldsymbol{T}^d \quad \text{on} \quad \partial_N\Omega, \quad \boldsymbol{u} = \boldsymbol{u}^d \quad \text{on} \quad \partial_D\Omega$, and $\underset{\sim}{\boldsymbol{\sigma}} \cdot \boldsymbol{n} = 0 \quad \text{on} \quad \Gamma$

The weak formulation of the BVP can be denoted as:

$$\int_{\Omega\backslash\Gamma} \frac{1}{2}\underset{\sim}{\boldsymbol{\varepsilon}}(\boldsymbol{u}) : \mathbb{A} : \underset{\sim}{\boldsymbol{\varepsilon}}(\boldsymbol{v})\mathrm{d}x - \int_{\Omega\backslash\Gamma} \boldsymbol{f}\,\boldsymbol{v}\,\mathrm{d}\Omega - \int_{\partial_N\Omega} \boldsymbol{T}^d \cdot \boldsymbol{v}\,\mathrm{d}s = 0 \quad \forall \boldsymbol{v} \in C_0\,(\boldsymbol{v} = \boldsymbol{0} \text{ on } \partial_D\Omega) \tag{1.4}$$

where $\boldsymbol{v}$ is the virtual displacement field, and C_0 is a set of admissible displacement fields. The solution $\boldsymbol{u}$ of the weak problem can be obtained by minimizing the energy $\mathcal{E}(\boldsymbol{u})$.

1.2 Media with isotropic surface energy

1.2.1 Classical approach

1.2.1.1 Griffith's concept of energy release rate

The fundamental work of LEFM was first proposed by A.A. Griffith in 1921, where he utilized classical mechanics and thermodynamics energy theorem to explain the brittle fracture behavior based on the concept of energy balance (Griffith, 1921). According to Griffith's criterion, the propagation of a crack is regarded as the creation of new surfaces that results in an increase in the surface energy. A cracked solid Ω is subjected to a mechanical loading, the total energy of the system $\mathcal{E}$ can be divided into two parts: stored elastic energy and surface energy. The crack propagation is the result of a competition between these two energies, coupled with the principle of minimization of the total energy of the system. When the stored elastic energy exceeds the energy required for creating new surfaces, crack propagation occurs. The decrease in the potential energy $\mathcal{E}_p$ of the cracked solid is defined as the energy release rate G:

$$G \equiv - \left. \frac{\partial \mathcal{E}_p}{\partial l} \right|_{\text{fixed loading}} \tag{1.5}$$

where l is the created crack surface. The potential energy comprises of the elastic energy, external work force $\boldsymbol{T}^d$ acting on $\partial_N \Omega$, denoted as follows:

$$\mathcal{E}_p(\boldsymbol{u}, \Gamma) := \int_{\Omega \setminus \Gamma} \frac{1}{2} \underset{\sim}{\boldsymbol{\varepsilon}}(\boldsymbol{u}) : \mathbb{A} : \underset{\sim}{\boldsymbol{\varepsilon}}(\boldsymbol{u}) \, \mathrm{d}x - \int_{\partial_N \Omega} \boldsymbol{T}^d \cdot \boldsymbol{u} \, \mathrm{d}s \tag{1.6}$$

1.2.1.2 Irwin's concept of Stress Intensity Factors

Griffith's theory was then refined by Irwin in 1950s, who introduced the concept of the Stress Intensity Factors (SIFs) (Irwin, 1957). SIFs are parameters that describe the intensity of stress at the crack tip in a material and can be used to determine whether a crack will propagate under different loading conditions. In Fracture mechanics, when performing a stress analysis for the crack surface, it is beneficial to differentiate three basic fracture modes, as illustrated in fig. 1.2:

1. Mode I (opening mode) corresponds to the normal separation of the crack surface under the tensile stresses.

2. Mode II (sliding mode) corresponds to shear stress acting parallel to the plane of the crack and perpendicular to the crack front.

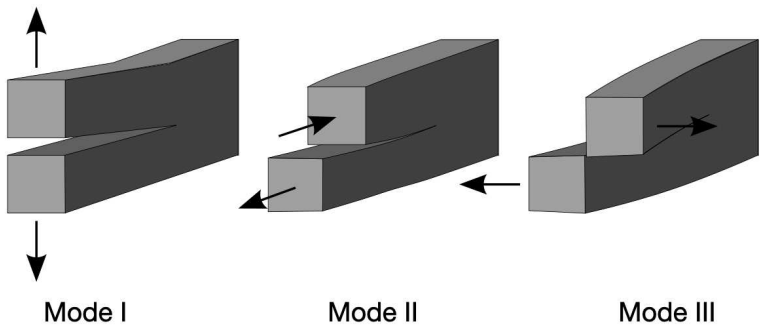

Figure 1.2 Modes of fracture

3. Mode III (tearing mode) corresponds to lateral shearing parallel to the crack front

A crack can be subjected to one or a combination of these three modes of loading. Consider the 2D elasticity BVP presented in previous section, we can disregard the tearing mode since $\boldsymbol{u}^d, \boldsymbol{T}^d$ have no out plane component and the stress field near the crack tip in xy coordinate (as illustrated in fig. 1.1) verifies for $r \to 0$ (Owen and Fawkes, 1983):

$$\begin{aligned}
\sigma_{xx} &= \frac{K_I}{\sqrt{2\pi r}} \cos\frac{\theta}{2}\left(1 - \sin\frac{\theta}{2}\sin\frac{3}{2}\theta\right) - \frac{K_{II}}{\sqrt{2\pi r}} \sin\frac{\theta}{2}\left(2 + \cos\frac{\theta}{2}\cos\frac{3\theta}{2}\right) + T \\
\sigma_{yy} &= \frac{K_I}{\sqrt{2\pi r}} \cos\frac{\theta}{2}\left(1 + \sin\frac{\theta}{2}\sin\frac{3}{2}\theta\right) + \frac{K_{II}}{\sqrt{2\pi r}} \sin\frac{\theta}{2}\cos\frac{\theta}{2}\cos\frac{3}{2}\theta \\
\sigma_{xy} &= \frac{K_I}{\sqrt{2\pi r}} \sin\frac{\theta}{2}\ \cos\frac{\theta}{2}\cos\frac{3}{2}\theta + \frac{K_{II}}{\sqrt{2\pi r}} \cos\frac{\theta}{2}\left(1 - \sin\frac{\theta}{2}\sin\frac{3}{2}\theta\right)
\end{aligned} \tag{1.7}$$

where K_I and K_{II} are known as the SIFs of modes I and II, respectively. The SIFs depends only on the geometry and the loading condition of the solid. The T is the higher-order term stands for T-stress, which is interpreted as the stress acting parallel to the crack tip along x-direction (Gupta et al., 2015). This parameter plays a crucial role in the selection of the crack path (Cotterell and Rice, 1980; Mesgarnejad et al., 2020).

The corresponding displacement field is denoted as follows (Owen and Fawkes, 1983):

$$\begin{aligned}
u_x &= \frac{K_I}{2\mu}\sqrt{\frac{r}{2\pi}}\cos\frac{\theta}{2}\left(\kappa - 1 + 2\sin^2\frac{\theta}{2}\right) + \frac{K_{II}}{2\mu}\sqrt{\frac{r}{2\pi}}\sin\frac{\theta}{2}\left(\kappa + 1 + 2\cos^2\frac{\theta}{2}\right) + \frac{T}{8\mu}r(\kappa+1)\cos\theta \\
u_y &= \frac{K_I}{2\mu}\sqrt{\frac{r}{2\pi}}\sin\frac{\theta}{2}\left(\kappa + 1 - 2\cos^2\frac{\theta}{2}\right) - \frac{K_{II}}{2\mu}\sqrt{\frac{r}{2\pi}}\cos\frac{\theta}{2}\left(\kappa - 1 - 2\sin^2\frac{\theta}{2}\right) + \frac{T}{8\mu}r(\kappa-3)\sin\theta
\end{aligned} \tag{1.8}$$

where κ is the Kolossov's constant, with $\kappa = (3-\nu)/(1+\nu)$ for plane stress assumption, $\kappa = (3-4\nu)$ for plane strain assumption, ν and μ is the Poisson's ratio and Shear modulus,

respectively. According to Irwin 1957, the stress intensity factors (SIFs) play a critical role in determining the potential for crack propagation by indicating the magnitude of stress at the crack tip. In a general case, the energy release rate can be calculated using the SIFs with the following equation:

$$G = \frac{1}{E'}(K_I^2 + K_{II}^2) \tag{1.9}$$

where $E' = E$ for plane stress assumption and $E' = \frac{E}{1-\nu^2}$ for plane strain assumption, where E represents the Young's modulus and ν represents the Poisson's ratio of the material.

The stress field near the crack tip is theoretically infinite, according to the asymptotic linear elastic solution. However, in reality, materials cannot endure an infinite stress state, rendering the asymptotic linear elastic solution inaccurate when approaching the crack tip due to material non-linearity and other factors. This region in the vicinity of the crack tip is known as the Fracture Process Zone (FPZ). Outside of the FPZ, the stress state is accurately described by the asymptotic solution in a region known as the K-dominant zone.

1.2.1.3 SIFs across a kink

The presence of anisotropic material properties can cause the crack to deviate from its original path and alter its direction, resulting in a crack kink. At the kink position, the SIFs are not continuous (Leblond, 1989). However, the Amestoy-Leblond's formula proposed by Amestoy and Leblond 1992, provides a relationship between SIFs before and after kinking, which allows for determination of SIFs at the kinked crack tip.

Consider a crack in an isotropic homogeneous elastic solid Ω subjected to a constant load between two states: a state without a kink and a state with a kink as shown in Fig. 1.3. The SIFs before and after kinking are denoted by K_q and $K_p(s, \varphi)$ respectively. For $s \to 0$, the relationship can be described by Amestoy-Leblond's formula as follows:

$$K_p(s, \varphi) = F_{pq}(\varphi)K_q + T\sqrt{s}\, G_p(\varphi) + O(s) \tag{1.10}$$

where $F_{pq}(\varphi)$ and $G_p(\varphi)$ are universal functions that depend on the kink angle φ. s represents the kink length, and T is the T-stress prior to the occurrence of kink, which appears in the stress field near crack tip, as shown in eq. (1.7).

By introducing the limit $s \to 0$:

$$K_p^*(\varphi) = \lim_{s \to 0} K_p(s, \varphi) \tag{1.11}$$

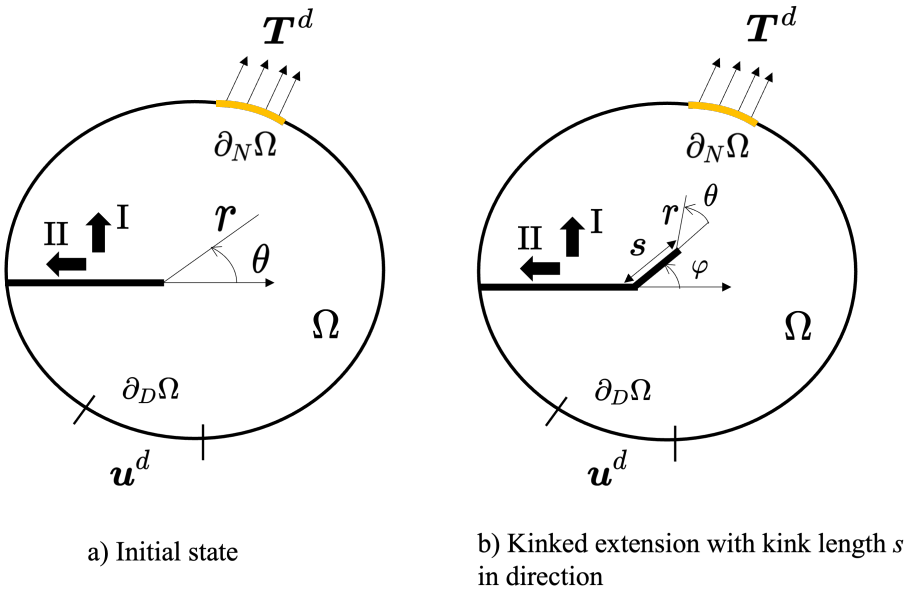

a) Initial state

b) Kinked extension with kink length s in direction

Figure 1.3 Crack kink in a linear elastic body

The relation can be denoted as following expression:

$$K_p^*(\varphi) = F_{pq}(\varphi)K_q \tag{1.12}$$

The expressions and graphs of $F_{pq}(\varphi)$ and $G_p(\varphi)$ have been provided by Amestoy and Leblond 1992. They are recalled in Appendix. A. By substituting the SIFs after kinking $K_p^*(\varphi)$ into Irwin's formula eq. (1.9), we can obtain the energy release rate for all potential direction:

$$G(\varphi) = \frac{1}{E'}((K_I^*(\varphi))^2 + (K_{II}^*(\varphi))^2) \tag{1.13}$$

In Section 3.1.1, we will test the accuracy of our numerical model in calculating the SIFs across a kink using the Amestoy-Leblond's formula.

1.2.1.4 Propagation threshold

To determine if a crack will propagate or not, we compare the critical surface energy G_c with the energy release rate G. G_c is regarded as a material property that signifies its resistance to fracture. Propagation becomes feasible when the condition $G = G_c$ is met. This comparison aligns with Irwin's formula, which equates to assessing the SIFs against a critical value known as the fracture toughness of the material K_{IC}. For mode I loading, when $K_I \geq K_{IC}$, the crack can propagate. Irwin also demonstrated that criteria

for crack propagation based on either the energy release rate or the SIFs are equivalent only in mode I. Consequently, the propagation threshold according to Irwin's law can be expressed as follows:

$$\begin{cases} K_I < K_{IC} & \text{no propagation} \\ K_I \geq K_{IC} & \text{possible propagation} \end{cases} \tag{1.14}$$

The parameter K_{IC} is referred to as a material property under mode I loading, namely toughness, which characterizes the material's resistance to crack propagation. It can be determined through standardized fracture tests conducted on Compact Tension (CT) or Single Edge Notch Bend (SENB) specimens. On the contrary, the SIF K_I is a structural property that relies on the geometry, material behavior, and loading of the entire structure. It is commonly obtained through numerical simulations by assuming linear elasticity.

1.2.1.5 Quasi-static propagation: Griffith's evolution law

To determine the crack evolution under imposed loading, we first recall the Griffith's evolution law. At a specific time t, the energy release rate is represented as $G(t, l)$, which signifies the rate at which energy is released during the progression of a crack with a length of l along a pre-defined crack path. During quasi-static evolution, the time t solely serves as a loading parameter that describes the loading history. For a linear elastic isotropic 2D body under quasi-static assumption, the Griffith's evolution law can be expressed through the following three criteria (Marigo, 2010):

1. **Irreversibility**: $l(0) = l_0$, $t \mapsto l(t)$ is increasing
2. **Yield criterion**: $G(t, l(t)) \leq G_c$
3. **Energy balance**: $(G(t, l(t)) - G_c)\, \dot{l}(t) = 0$

It is crucial to emphasize that the aforementioned formulation is specifically applicable to the smooth evolution of cracks. Additionally, this formulation assumes the existence of an initial crack and its propagation along a pre-determined path. Consequently, it does not provide a means to address crack initiation or the selection of crack paths. Therefore, the question regarding the determination of the crack path becomes a consequential consideration.

1.2.1.6 Question of the path: additional criterion

Griffith's evolution law assumes that the crack propagation path is known *a priori*, and therefore it cannot be used alone to predict the trajectory of crack propagation. An

additional criterion is needed in conjunction with Griffith's law to predict the crack path. Various criteria have been proposed and classified into different categories: stress-based criteria such as the Maximum Tangential Stress criterion (MTS) (Erdogan and Sih, 1963), strain-based criteria like the Strain Energy Density criterion (SED) (Sih, 1974), and energy-based criteria, including the widely used Maximum Energy Release rate ($G_{\max}$) (Hussain et al., 1973). The $G_{\max}$ criterion states that the crack extension direction maximizes the release rate of potential energy, the predicted direction θ^* can be therefore obtained by maximizing the eq. (1.13). Furthermore, the Principle of Local Symmetry (PLS) (Goldstein and Salganik, 1974) criterion is based on the assumption that if a crack is in Mode I during propagation, the crack tip's local symmetry prevents the crack from changing direction. It is known that the $G_{\max}$ and PLS criteria are among the most commonly used methods to determine the crack path. For isotropic materials, they can accurately predict the angle of crack kink with only minor differences. Therefore, these two criteria are essentially equivalent (Amestoy and Leblond, 1992).

1.2.2 Variational approach

Up until now, we have presented the classical approach to fracture, which has demonstrated its ability to address various fracture problems. However, this approach still relies on certain prerequisites, such as a predefined pre-crack or a well-defined criterion for path selection (Bourdin, 1998). Furthermore, when dealing with 3D effects, anisotropic materials, or heterogeneous materials, the complexity of the problem increases, necessitating the extension of fracture criteria to a more general framework for crack path prediction. To overcome these limitations of the classical approach and provide a physically meaningful framework for fracture problems in a broader context, the variational approach was proposed by Francfort and Marigo 1998. This approach involved a reevaluation of Griffith's concept using the mathematical tools provided by the Calculus of Variations. It builds upon Griffith's notion that crack evolution arises from the interplay between bulk energy and surface energy. The concept of variational approach is described as follows: let $\Omega \subset \mathcal{R}^n$ be a solid with a time-dependent displacement $\boldsymbol{u} = \boldsymbol{u}^d(x,t)$ applied to its boundary $\partial_D\Omega$, the surface forces $\boldsymbol{T}^d(x,t)$ are applied on the Neumann region $\partial_N\Omega$, and Γ represents the crack set. The energy functional of the cracked solid can be expressed as the sum of the potential energy and the surface energy:

$$\mathcal{E}(\boldsymbol{u},\Gamma) := \mathcal{E}_p(\boldsymbol{u},\Gamma) + \mathcal{E}_s(\Gamma) \tag{1.15}$$

where $\mathcal{E}_s(\boldsymbol{u}, \Gamma)$ refers to the dissipated energy that arises from the creation of surface. For brittle solid, the dissipated energy or surface energy $\mathcal{E}_s$ is defined as:

$$\mathcal{E}_s(\Gamma) := G_c \mathcal{H}^{n-1}(\Gamma) \tag{1.16}$$

where $\mathcal{H}^{n-1}(\Gamma)$ denotes the $(n-1)$ dimensional Hausdroff measure of the crack. For each time step, we seek for the global minimizer $(\boldsymbol{u}, \Gamma)$ of following total energy:

$$\mathcal{E}(\boldsymbol{u}, \Gamma) = \int_{\Omega \setminus \Gamma} \frac{1}{2} \underset{\sim}{\boldsymbol{\varepsilon}}(\boldsymbol{u}) : \mathbb{A} : \underset{\sim}{\boldsymbol{\varepsilon}}(\boldsymbol{u}) \, \mathrm{d}x - \int_{\partial_N \Omega} \boldsymbol{T}^d \cdot \boldsymbol{u} \, \mathrm{d}s + G_c \mathcal{H}^{n-1}(\Gamma) \tag{1.17}$$

Meanwhile, the evolution problem should conform to the revisited Griffith's evolution law, also known as the Francfort-Marigo law (Marigo, 2010) :

1. **Irreversibility**: $t \mapsto \Gamma(t)$ increasing
2. **Stability criterion**: $\mathcal{E}(t, \Gamma(t)) \leq \mathcal{E}(t, \Gamma), \forall t \geq 0$ and $\forall \Gamma \in [\Gamma(t), \Gamma_s]$
3. **Energy balance**: $\mathcal{E}(t, \Gamma(t)) = \mathcal{E}(0, \Gamma(0)) + \int_0^t \frac{\partial \mathcal{E}}{\partial t'}(t', \Gamma(t'))\mathrm{d}t' \quad \forall t \geq 0$

It is noticed this formulation allows for the possibility of $\Gamma(0) = \varnothing$, which means that there are no requirements for a pre-existing crack. In summary, the revised Griffith's law is applicable to general cases, including 3D bodies and anisotropic settings. Besides, it incorporates a criterion for path selection.

The problem previously introduced is referred to as the strong variational evolution (Bourdin et al., 2008). To establish a more convenient formulation, it is advantageous to define the weak formulation by expanding the set of admissibility functions to a suitable space that allows for discontinuous displacement fields. Therefore the weak variational evolution is denoted as follows by introducing the function space SBV [1]:

$$\min\{\int_{\Omega} \frac{1}{2} \underset{\sim}{\boldsymbol{\varepsilon}}(\boldsymbol{u}) : \mathbb{A} : \underset{\sim}{\boldsymbol{\varepsilon}}(\boldsymbol{u}) \, \mathrm{d}x - \int_{\partial_N \Omega} \boldsymbol{T}^d \cdot \boldsymbol{u} \, \mathrm{d}s + G_c \mathcal{H}^{n-1}(S(\boldsymbol{u})), \ \boldsymbol{u} \in SBV(\Omega)\} \tag{1.18}$$

where $S(\boldsymbol{u})$ is the jump set of $\boldsymbol{u}$. The strong variational evolution problem has been proven to be equivalent to the weak one (Alessi, 2013).

[1] special functions with bounded variation, which is used to provide a weak formulation for certain variational problems with free discontinuity (Braides, 1998)

1.3 Extension to an anisotropic surface energy

In this dissertation, our primary focus is on studying the effects of anisotropic surface energy in conjunction with isotropic elasticity. This research aligns with the experimental system we have developed using 3D printing techniques (Corre and Lazarus, 2021). By investigating the anisotropy present in the surface energy, we aim to enhance our understanding of its contribution to the phenomenon of crack kinking. Next, we will present the incorporation of anisotropic surface energy in both classical approach and variational approach.

1.3.1 Generalized Maximum Energy Release Rate in classical approach

The stress-based and PLS criteria lose their relevance in an anisotropic setting. Therefore, the Generalized Maximum Energy Release Rate (GMERR) (Chambolle et al., 2009; Takei et al., 2013) has been proposed for materials with isotropic elasticity and anisotropic fracture toughness. When the energy release rate $G(\theta)$ as defined in eq. (1.13) is lower than the orientation-dependent surface energy $G_c(\theta)$, these is no possible propagation. And when $G(\theta) = G_c(\theta)$, propagation may take place in the direction θ^* that maximizes the ratio between the energy release rate $G(\theta)$ and the orientation-dependent surface energy $G_c(\theta)$:

$$\theta^* = \operatorname{argmax}\left[\frac{G(\theta)}{G_c(\theta)}\right] \tag{1.19}$$

once the load is high enough to get $G(\theta^*) = G_c(\theta^*)$.

Fig. 1.4 exhibits the visualization of GMERR in a Wulff diagram (Takei et al., 2013). The black curve represents a four-fold symmetric surface energy chosen for illustration, given by $G_c(\theta) = G_c\sqrt[4]{1 - 0.8\cos 4\left(\theta - \frac{5\pi}{36}\right)}$. The green dot-line represents the reciprocal energy release rate $\frac{1}{G(\theta)}$ before crack propagation, and the green curve is the reciprocal energy release rate $\frac{1}{G(\theta)}$ at the stage when the crack begins to propagate. As the load increases, the reciprocal of energy release rate $\frac{1}{G(\theta)}$ approaches the reciprocal surface energy, and the first intersection point gives the predicted angle θ^* and the relevant critical loading. To obtain the relation between the critical load and crack angle, with the aid of the LEFM and propagation criteria, we can write the following equation:

$$\begin{cases} F_c^2(\theta) \cdot \hat{G}(\theta) & = G_c \\ F_c^2(\theta = 0) \cdot \hat{G}(\theta = 0) & = G_c \end{cases} \tag{1.20}$$

Due to $K_p \propto$ loading $\mathcal{L}$, referring to Irwin's formula, eq (1.9), the energy release rate $G(\theta) = \mathcal{L}^2 \hat{G}(\theta)$. Therefore, we can extract the force component from the energy release rate $G(\theta)$, resulting in $F_c^2(\theta) \cdot \hat{G}(\theta)$, where $F_c(\theta)$ represents the critical force required for propagation in the direction θ, and $\hat{G}(\theta)$ denotes the energy release rate in the direction θ at unit load $F = 1$. By dividing these two equations, we can derive the following expression which describes the relationship between critical load and crack angle:

$$F_c(\theta) = \left[\frac{\hat{G}(\theta = 0)}{\hat{G}(\theta)}\right]^{0.5} \cdot F_c(\theta = 0) \tag{1.21}$$

where the energy release rate at unit load can be substituted with Irwin's formula eq. (1.9) and Amestoy-Leblond's formula eq. (1.3).

Takei et al. 2013 validated the GMERR criterion by conducting tearing experiments on bi-oriented polypropylene sheets that exhibit strongly anisotropic fracture toughness. Subsequently, Mesgarnejad et al. 2020 investigated crack propagation in materials with weakly anisotropic surface energy using a combination of experiments and phase-field modeling. The study revealed the importance of considering the T-stress term when calculating the energy release rate $G(\theta)$ in the GMERR criterion, as shown below:

$$\begin{aligned} K_p^*(\theta) &= K_q F_{pq}(\theta) + T\sqrt{s} G_p(\theta) \\ G(\theta) &= K_p^*(\theta)^2 / E \end{aligned} \tag{1.22}$$

Mesgarnejad et al. 2020 made a significant decision regarding the choice of the kink length value s. They opted to set s equal to the size of FPZ. This particular choice yielded highly accurate predictions in their experiments and phase-field modeling.

The application of GMERR will be introduced in Section 3.2.2 and Section 4.2, it is mainly used to compare with the crack path and relevant critical load obtained from experiments and simulations.

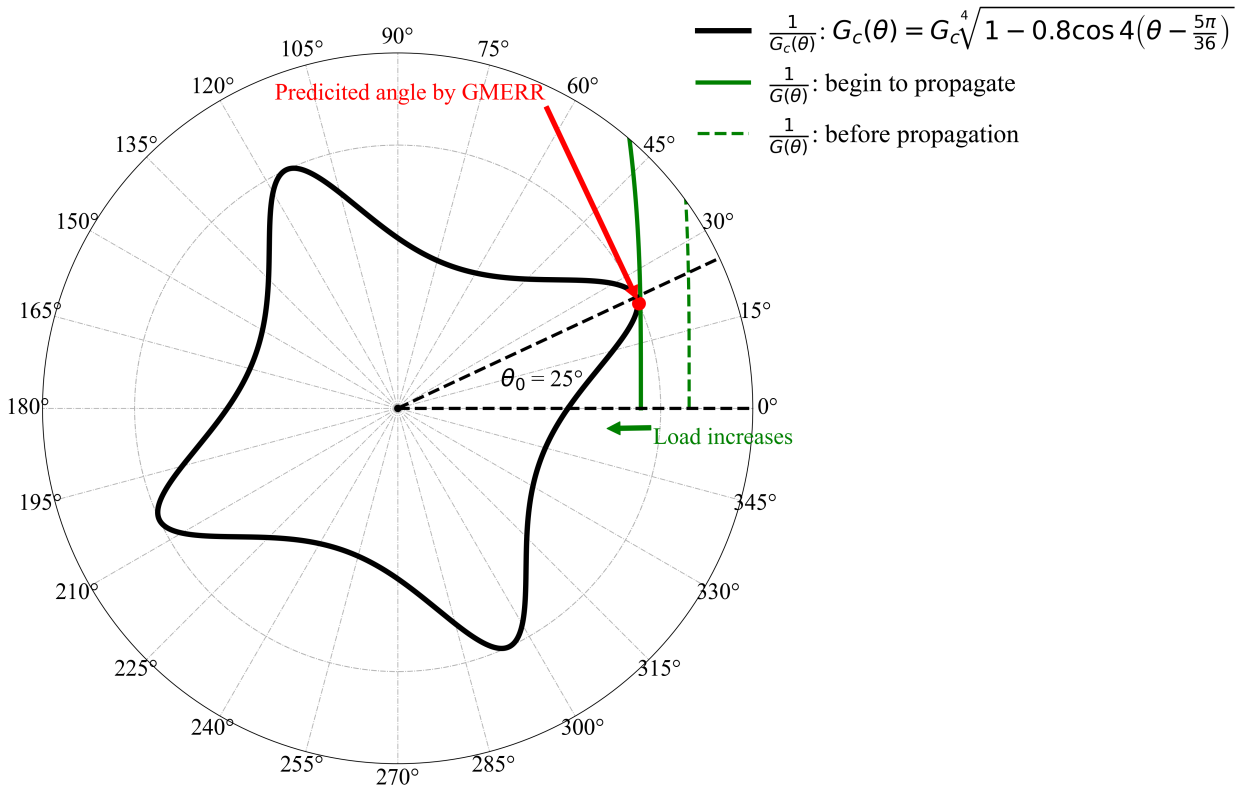

Figure 1.4 Wulff diagram: visualization of GMERR

1.3.2 Sharp model of anisotropic brittle fracture in variational approach

The energy functional of a cracked body with anisotropic surface energy is denoted as follows (Li and Maurini, 2019):

$$\mathcal{E}(\boldsymbol{u}, \Gamma) = \int_{\Omega \setminus \Gamma} \frac{1}{2} \underset{\sim}{\boldsymbol{\varepsilon}}(\boldsymbol{u}) : \mathbb{A} : \underset{\sim}{\boldsymbol{\varepsilon}}(\boldsymbol{u}) \mathrm{d}x - \int_{\partial_N \Omega} \boldsymbol{T}^d \cdot \boldsymbol{u} \, \mathrm{d}s + G_0 \int_{\Gamma} \gamma(\boldsymbol{n}) \, \mathrm{d}\mathcal{H}^{n-1} \tag{1.23}$$

where the third term represent the anisotropic surface energy, and $\boldsymbol{n}$ is the unit vector normal to the crack path. The orientation-dependent surface energy $G_c(\boldsymbol{n})$ is decomposed into a scaling factor of energy per unit surface G_0 and a dimensionless functional $\gamma(\boldsymbol{n})$. The anisotropic surface energy can be classified into two categories: weakly anisotropic, which is associated with a convex function $\gamma(\boldsymbol{n})$, and strongly anisotropic, which is related to a non-convex $\gamma(\boldsymbol{n})$. In a 2D polar coordinates, the unit normal $\boldsymbol{n}$ can be replaced a single angle θ, then we have $\gamma(\theta) = \gamma(\boldsymbol{n}(\theta))$ (Sekerka, 2005). The function $\gamma(\theta)$ becomes

non-convex when it violates the following local convexity condition (Takei et al., 2013):

$$\gamma(\theta) + \gamma''(\theta) < 0 \tag{1.24}$$

As the surface energy becomes strongly anisotropic, the presented sharp model is ill-posed due to the lack of semi-continuity (Fonseca, 1992), hence an intrinsic regularized model (Li and Maurini, 2019) will be introduced in next Section 1.4.3.2.

1.4 Numerical method for fracture problem

Computational fracture mechanics involves developing numerical methods to model the behavior of material under different loading conditions, with the aim of estimating crack initiation and propagation. Fracture modeling approaches can be classified into two categories: discontinuous and continuum crack models.

In the discontinuous crack modeling, cracks are regarded as surfaces of discontinuity, hence it faces the challenge of introducing displacement discontinuities in the numerical model. To address with this issue, Ingraffea and Saouma 1985 proposed the Adaptive Mesh Refinement (AMR) method, which introduces new boundaries as crack propagating. Alternative method consist of the Extend Finite Element Method (XFEM) (Moës et al., 1999), which introduces additional enrichment functions to capture the discontinuities or singularities in the solution. However, discontinuous models with specific techniques face not only challenges in numerical efficiency, but also in determining propagation criteria independently of the discretization technique.

The limitations of discontinuous crack models have thus led to the parallel development of continuum crack model (Wu et al., 2020). Among these, the phase-field or gradient damage model has emerged as a prominent and promising approach. In this model, the crack is represented as a diffuse field of damage concentrated within a narrow band as illustrated in fig. 1.5 b), the model incorporates a damage variable that distinguishes between intact and fractured material. Several phase-field models based on different approaches have been proposed, such as the dynamic phase-field model based on Ginzburg-Landau's equation (Karma et al., 2001), which is widely used in the physics community. Another approach based on the variational approach to fracture, which was proposed by Bourdin et al. 2000 and has gained widespread acceptance in the mechanics community.

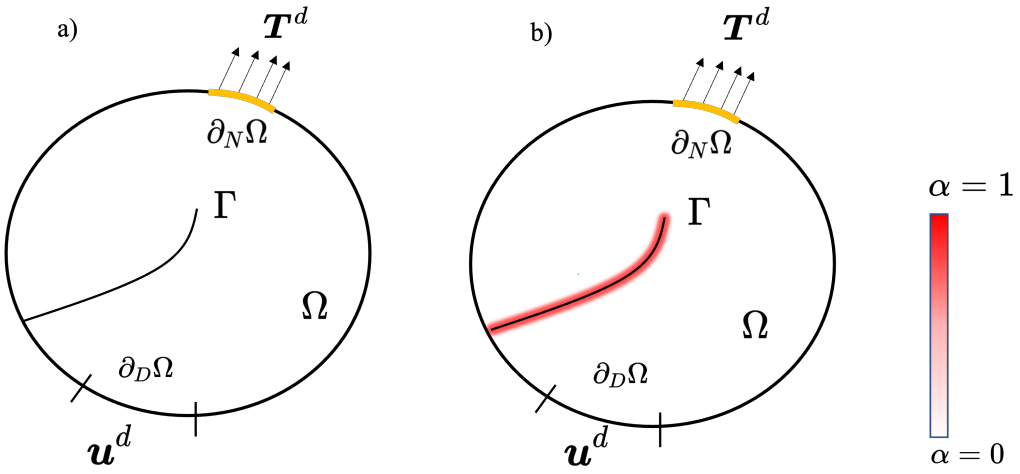

Figure 1.5 Crack set Γ a in a solid Ω : a) sharp crack, b) crack set represented by a diffused damage field

In following section, we will introduce the numerical models employed in order to solve the static elasticity problem and the damage evolution problem. The classic approach based model as presented in section 1.2.1 was used to deal with the static elasticity problem, primarily to determine the fracture parameters when crack kinking is involved due to anisotropic fracture toughness. The variational approach as presented in section 1.2.2 based model was used to solve the damage evolution problem when coupled with anisotropic settings.

1.4.1 Static elasticity problem: numerical method to determine SIFs

The FEM model based on the classic approach involves solving a linear elastic problem with a fixed geometry and calculating the SIFs at each set of the prorogation in presence of a crack kink due to the anisotropic surface energy.

1.4.1.1 G - θ method

Computing the SIF for both Mode I and Mode II in the presence of the kinked crack was achieved using the $G-\theta$ method. This method replaces the Rice integral with a surface integral based on Stokes's theorem (Destuynder et al., 1981), enabling the separation of the SIFs for different modes. The superiority of $G-\theta$ method is that it allows to bypass the numerical difficulties associated with the singularity of the deformations and stresses at the crack tip.

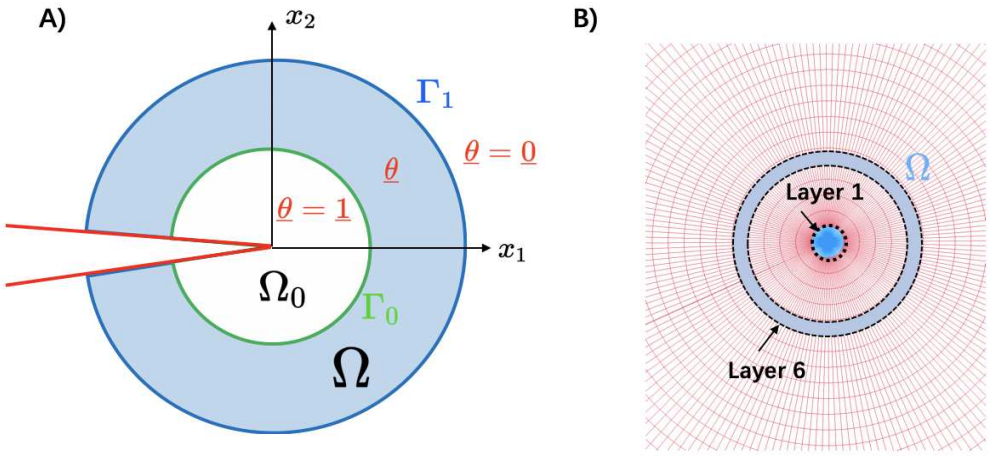

Figure 1.6 The $G-\theta$ method diagram is shown in figure A). The mesh in the vicinity of the crack tip and region where the $G-\theta$ method is applied are shown in figure B)

Consider a domain $\Omega \subseteq R^2$ shown in Fig. 1.6. The energy release rate can be expressed as:

$$G = -\int_{\Omega} \nabla \boldsymbol{\theta}^T : \underset{\sim}{\boldsymbol{E}} \mathrm{d}S$$

where $\underset{\sim}{\boldsymbol{E}}$ is Eshelby tensor is expressed:

$$\underset{\sim}{\boldsymbol{E}} = W \underset{\sim}{\boldsymbol{I}} - \nabla \boldsymbol{u}^T \cdot \underset{\sim}{\boldsymbol{\sigma}}$$

and W is the strain energy density in an isotropic elastic solid:

$$W = \frac{1}{2}(\underset{\sim}{\boldsymbol{\sigma}} : \underset{\sim}{\boldsymbol{\varepsilon}}) \tag{1.25}$$

Then we build a fictitious velocity field $\boldsymbol{\theta}(\boldsymbol{x})$ and a virtual time variable η which transforms the domain Ω_η to $\Omega_\eta + d\eta$, where $\boldsymbol{\theta}(\boldsymbol{x})$ is defined as:

$$\begin{cases} \boldsymbol{\theta}(\boldsymbol{x}) = \mathbf{1} & r = 0 \\ \boldsymbol{\theta}(\boldsymbol{x}) = \boldsymbol{\theta}(\boldsymbol{x}) & 0 < r \leq R \\ \boldsymbol{\theta}(\boldsymbol{x}) = \mathbf{0} & R < r \end{cases}$$

Finally, the SIF can be expressed following by separating different modes (taking opening mode as an example) (Bonnet and Frangi, 2007):

$$\frac{2\left(1-\nu^2\right)}{E} K_I = -\int_{\Omega} \left(\frac{1}{2} \sigma_{ij} u^{(1)}_{i,j} \theta_{k,k} - \sigma_{ij} u^{(1)}_{j,k} \theta_{k,i} \right) \mathrm{d}\Omega$$

where $\boldsymbol{u}^{(1)}$ is the displacement field near the crack tip shown in eq. (1.8) for $K_I = 1$, $K_{II} = 0$ and $K_{III} = 0$. The index i, j represents the derivative of the displacement component u_i with respect to the x_j direction.

1.4.1.2 Interaction integral

The T-stress can be determined using a direct method numerically: which involves phase subtraction of the stress field near the crack tip:

$$T = \lim_{r \to 0} \left[\sigma_{rr}(r, \theta = 0) - \sigma_{\theta\theta}(r, \theta = 0) \right] \tag{1.26}$$

However, it is worth noting that the direct method for determining the T-stress, as reported in Mesgarnejad et al. 2020, requires careful consideration of convergence, and as a result, the accuracy of the obtained T-stress may not be optimal. As an alternative, we presented the Interaction Integral or I-integral. It has demonstrated great promise in accurately determining the T-stress and has been implemented into widely used finite element software Abaqus (Abaqus, 2023). Meanwhile it can be used to separate the SIFs in mixed mode. It involves computing a contour integral inspired by Rice's J-integral (Rice, 1968) concept:

$$J = \lim_{\Gamma \to 0} \int_{\Gamma} \left(W \delta_{1i} - \sigma_{ij} u_{j,1} \right) n_i \, \mathrm{d}\Gamma \tag{1.27}$$

δ_{ij} is the Kronecker delta, and n_i is the outward normal vector to the contour Γ, as shown in fig. 1.7. Rice's J-integral has been shown to be path-independent for isotropic linear elastic homogeneous solids, and $J = G$ when crack propagation is straight.

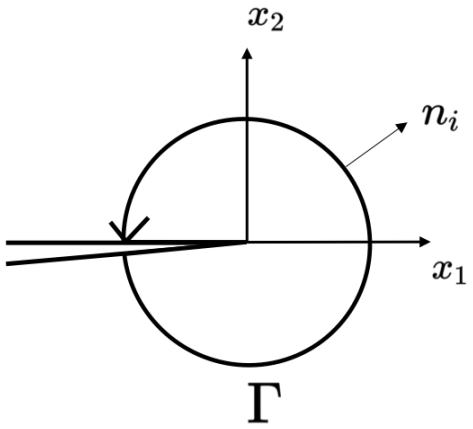

Figure 1.7 J-integral around the crack tip

However, J-integral alone cannot distinguish between the two SIFs, mode I K_I and

mode II K_{II}. Inspired by a two stated integral based on the Betti's reciprocity theorem, Chen and Shield 1977 proposed superimpose an auxiliary field on the actual field in J-integral, eq. (1.27) can be expressed as:

$$J^{sum}(u_i+u_i^{aux}) = \lim_{\Gamma\to 0}\int_{\Gamma}\left[\frac{1}{2}\left(\sigma_{jk}+\sigma_{jk}^{aux}\right)\left(\varepsilon_{jk}+\varepsilon_{jk}^{aux}\right)\delta_{1i}-\left(\sigma_{ij}+\sigma_{ij}^{aux}\right)\left(u_{j,1}+u_{j,1}^{aux}\right)\right]n_i\ \mathrm{d}\Gamma \tag{1.28}$$

Through rearrangement of the previous equation, the J^{sum} term can be separated into three components: J, J^{aux}, and I. Here, J represents the J-integral of the actual field, J^{aux} represents the J-integral of the auxiliary field, and the final term I is commonly referred to as the interaction integral or I-integral. The expression for the interaction integral is as follows:

$$I = \lim_{\Gamma\to 0}\int_{\Gamma}[\frac{1}{2}\left(\sigma_{jk}\varepsilon_{jk}^{aux}+\sigma_{jk}^{aux}\varepsilon_{jk}\right)\delta_{1i}-\sigma_{ij}^{aux}u_{j,1}-\sigma_{ij}u_{j,1}^{aux}]\ n_i\ \mathrm{d}\Gamma \tag{1.29}$$

It is crucial to note that both the actual field and auxiliary field should satisfy the equilibrium condition and be kinematically admissible. Similar to the J-integral, the I-integral is also path-independent for homogeneous materials. Notably, the I-integral can be used in both isotropic and anisotropic media with the appropriate auxiliary fields (Yu and Kuna, 2021). To separate the SIFs K_I and K_{II} under mixed mode loading, Yau et al. 1980 used the stress and displacement field near the crack tip which are given by eq. (1.7) and eq. (1.8), and the higher-order term T-stress is excluded. The J^{sum} can be therefore denoted as follows (plane stress assumption):

$$J^{sum} = \frac{1}{E'}\left[\left(K_I+K_I^{aux}\right)^2+\left(K_{II}+K_{II}^{aux}\right)^2\right] \tag{1.30}$$

where K_I^{aux} and K_{II}^{aux} are SIFs in the auxiliary field, finally the I-integral can be obtained:

$$I = \frac{2}{E'}\left(K_IK_I^{aux}+K_{II}K_{II}^{aux}\right) \tag{1.31}$$

By substituting the auxiliary fields into eq. (1.29), we can have access to the value of I-integral. Then setting the auxiliary SIFs: K_I^{aux} and K_{II}^{aux} to 0 respectively, different I-integral correspond to different fracture modes $I^{(I)}$ and $I^{(II)}$ can be obtained. The SIFs K_I and K_{II} can be computed using the following equations:

$$K_I = \frac{E'}{2}I^{(I)}, K_{II} = \frac{E'}{2}I^{(II)} \tag{1.32}$$

Inspired by the solution of the concentrated force at a point of straight boundary problem (Timoshenko and Goodier, 1951), Kfouri 1986 determined the higher-order term

T-stress through the I-integral by using the following defined auxiliary field:

$$\begin{aligned} u_1^{aux} &= -\frac{F}{\pi}\frac{\kappa+1}{8\mu}\ln\frac{r}{d} - \frac{F}{\pi}\frac{1}{4\mu}\sin^2\theta, u_2^{aux} = -\frac{F}{\pi}\frac{\kappa-1}{8\mu}\theta + \frac{F}{\pi}\frac{1}{4\mu}\sin\theta\cos\theta \\ \sigma_{11}^{aux} &= -\frac{F}{\pi r}\cos^3\theta, \sigma_{22}^{aux} = -\frac{F}{\pi r}\cos\theta\sin^2\theta, \sigma_{12}^{aux} = -\frac{F}{\pi r}\cos^2\theta\sin\theta \end{aligned} \tag{1.33}$$

The point force F and reference length d are typically taken as unit value in numerical practice. Through the utilization of the defined auxiliary field, the impact of the singular and higher order components of the actual stress will be eliminated, leaving only the T-stress to contribute the I-integral (Yu and Kuna, 2021). By substituting the auxiliary field into eq. (1.29), the value of I can be determined. This value of I can subsequently be employed to calculate the T-stress using the following expression:

$$T = IE' \tag{1.34}$$

The validation of the I-integral implementation will be thoroughly discussed in Section 3.1.2.

1.4.2 Phase-field model with isotropic surface energy

The variational formulation poses a challenge in the numerical implementation of the resulting discontinuity problem. To handle this issue, Bourdin et al. 2000 regularized the formulation 1.6 and implemented it numerically by following the strategy of Ambrosio and Tortorelli's regularization of the Mumford-Shan problem in image processing (Ambrosio and Tortorelli, 1990; Mumford and Shah, 1989). This regularization can be seen as an approximation using elliptic functions and enables convergence towards the sharp model of brittle fracture. In the numerical model of variational approach to fracture, a scalar phase-field α is used to represent the cracks, with values ranging from 0 to 1, allowing for a smooth transition from intact to fractured states.

The functional of regularized energy can be denoted as:

$$\mathcal{E}_\ell(\boldsymbol{u},\alpha) = \int_\Omega a(\alpha)W(\boldsymbol{u})\mathrm{d}\Omega + \frac{G_c}{c_w}\int_\Omega\left(\frac{w(\alpha)}{\ell} + \ell\|\nabla\alpha\|^2\right)\mathrm{d}\Omega \tag{1.35}$$

where $\boldsymbol{u}$ is the displacement field, α is the damage variable that varies in $[0, 1]$ ($\alpha = 1$ meaning the material is completely fractured). The stiffness modulation function with respect to the damage variable is denoted by $a(\alpha)$, while $w(\alpha)$ is the dissipation potential and $c_w = 4\int_0^1\sqrt{w}(\alpha)d\alpha$ is the normalization parameter. $W(\boldsymbol{u})$ in first term represents

the elastic energy density refer to eq. (1.25). And the second term is regarded as the dissipation potential composed of two parts, a local term $w(\alpha)$ depending only on the damage state and a gradient damage term $\nabla\alpha$ which penalizes sharp localization of the damage. ℓ is the regularization parameter that controls the width of the damage field. As ℓ approaches 0, the isotropic damage energy function tends towards the Griffith-type brittle fracture model in a Gamma-convergence sense (Bourdin et al., 2000).

Possible choices for stiffness modulation and dissipation potential are the AT1, AT2 models (Tanné et al., 2018) and KKL model (Karma et al., 2001), denoted as follows:

$$\begin{cases} a(\alpha) = (1-\alpha)^2 \quad , \quad w(\alpha) = \alpha & \text{AT1 model} \\ a(\alpha) = (1-\alpha)^2 \quad , \quad w(\alpha) = \alpha^2 & \text{AT2 model} \\ a(\alpha) = 4(1-\alpha)^3 - 3(1-\alpha)^4 \quad , \quad w(\alpha) = 1 - a(\alpha) & \text{KKL model} \end{cases} \tag{1.36}$$

For alternative damage models, refer to Wu et al. 2020.

We denote $\mathcal{C}$ as the set of admissible displacement fields and $\mathcal{D}$ as the set of accessible damage fields:

$$\begin{aligned} \mathcal{C} &:= \left\{ \boldsymbol{u} \in H^1(\Omega), \boldsymbol{u} = \boldsymbol{u}^d(x,t) \text{ on } \partial_D\Omega \right\}, \\ \mathcal{D} &:= \left\{ \alpha \in H^1(\Omega), 0 \le \alpha_{i-1}(x) \le \alpha(x) \le 1, \forall x \in \Omega \right\}. \end{aligned} \tag{1.37}$$

where $\alpha_{i-1}(x) \le \alpha(\mathrm{x})$ represents the regularized irreversible damage evolution. The solution to the problem can be obtained using an alternate minimization algorithm. This algorithm involves solving a sequence of minimization sub-problems on the displacement $\boldsymbol{u}$ for a fixed damage variable α, and similarly solving minimization sub-problems on α for a fixed $\boldsymbol{u}$ until the convergence is achieved (Pham et al., 2011). The given solution $(\boldsymbol{u}_i, \alpha_i)$ of the local minimisation problem must adhere to what are referred to as the first-order optimality conditions, as outlined in (León Baldelli and Maurini, 2021), as following:

$$\begin{aligned} &\frac{\partial \mathcal{E}_i(\boldsymbol{u}_i, \alpha_i)}{\partial \boldsymbol{u}} = \mathbf{0}, \\ &\alpha_i - \alpha_{i-1} \ge \mathbf{0}, \quad \frac{\partial \mathcal{E}_i(\mathbf{u}_i, \alpha_i)}{\partial \alpha} \ge \mathbf{0}, \quad \frac{\partial \mathcal{E}_i(\boldsymbol{u}_i, \alpha_i)}{\partial \alpha} \cdot (\alpha_i - \alpha_{i-1}) = 0 \end{aligned} \tag{1.38}$$

The phase-field model provides a significant benefit by demonstrating that as the parameter ℓ approaches zero, the surface of the regularized crack Γ_ℓ converges to that of the sharp crack Γ through Γ-convergence, thereby approaching Griffith's brittle fracture

model. Furthermore, the phase-field model of fracture offers additional advantages. It does not require $ad-hoc$ conditions to capture the crack initiation and growth. Additionally, the phase-field model is easy to incorporate different fracture mechanisms, such as ductile fracture (Alessi et al., 2015; Ambati et al., 2015; Brach et al., 2019a), dynamic fracture (Bourdin et al., 2011; Li et al., 2016), fatigue fracture (Mesgarnejad et al., 2019; Grossman-Ponemon et al., 2022; Schreiber et al., 2020), thin film fracture (Mesgarnejad et al., 2013; León Baldelli et al., 2013, 2014), hydraulic fracture (Wilson and Landis, 2016; Xia et al., 2017). Moreover, the phase-field model can easily be coupled with other physical fields, such as thermal or drying effects (Maurini et al., 2013; Bourdin et al., 2014) or electromagnetic effects (Abdollahi and Arias, 2012; Wu and Chen, 2021). It can also be extended to anisotropic fracture (Li et al., 2015; Li and Maurini, 2019; Nguyen et al., 2017; Scherer et al., 2022).

1.4.3 Presence of anisotropic surface energy in phase-field model

From a review of the literature, it is evident that the anisotropic behavior can be incorporated into phase-field models through various approaches. For instance, one approach involves introducing an anisotropic fracture surface energy, drawing inspiration from anisotropic crystal solids (Hakim and Karma, 2005; Li et al., 2015; Teichtmeister et al., 2017), another approach involves incorporating anisotropic stiffness degradation (Bleyer and Alessi, 2018; Scherer et al., 2022). Additionally, anisotropy can be considered through the use of layered media (Brach et al., 2019b; Brach, 2020). Here, our main emphasis is on investigating the impact of anisotropic surface energy while keeping the elasticity isotropic.

1.4.3.1 Two-fold symmetric model

To extend the model to an anisotropic model, various methods can be employed resulting in different types of anisotropy. One approach involves introducing a second-order matrix into the non-local fracture energy, resulting in a weakly anisotropic surface energy or a two-fold symmetric surface energy (Hakim and Karma, 2005, 2009; Mesgarnejad et al., 2020). The energy function can be expressed as follows:

$$\mathcal{E}_\ell(\boldsymbol{u},\alpha) = \int_\Omega a(\alpha)W(\boldsymbol{u})\mathrm{d}\Omega + \frac{G_0}{c_w}\int_\Omega \left(\frac{w(\alpha)}{\ell_0} + \ell_0\, \underset{\sim}{\mathcal{A}}\, \nabla\alpha\cdot\nabla\alpha\right)\mathrm{d}\Omega \tag{1.39}$$

where $\underset{\sim}{\mathcal{A}}$ is defined as:

$$\underset{\sim}{\mathcal{A}} = \begin{bmatrix} \cos(\theta_0) & -\sin(\theta_0) \\ \sin(\theta_0) & \cos(\theta_0) \end{bmatrix} \begin{bmatrix} A_t^{-1} & 0 \\ 0 & 1 \end{bmatrix} \begin{bmatrix} \cos(\theta_0) & -\sin(\theta_0) \\ \sin(\theta_0) & \cos(\theta_0) \end{bmatrix}^T \tag{1.40}$$

with A_t represent the anisotropic indicator for two-fold symmetric model, and the surface energy becomes more anisotropic as A_t increases. In Mesgarnejad et al. 2020, they used the two-fold symmetric model to simulate the crack path in orientationally ordered composites. By comparing with the experimental results, they established relevance between the numerical anisotropic coefficient A_t and the volume fraction in their composite material. While the material axis θ_0 correspond to the fiber orientation in composite. Finally, the two-fold symmetric model results in an orientation-dependent surface energy:

$$G_c(\theta) = G_0 \sqrt{{A_t}^{-2} \sin^2(\theta - \theta_0 + \pi/2) + \cos^2(\theta - \theta_0 + \pi/2)} \tag{1.41}$$

1.4.3.2 Four-fold symmetric model

A four-fold symmetric model of anisotropy can be achieved by incorporating a fourth-order tensor $\mathbb{C}$ into the non-local fracture energy, which leads to a higher-order phase-field model (Borden et al., 2014). The validity of the Gamma-convergence result for the higher-order phase-field model, as presented in (Burger et al., 2015; Negri, 2020), has been established for the case of isotropic surface energy. As discussed in Li and Maurini 2019, such a result could potentially be extended to the weakly anisotropic case, where the function $G_c(\theta)$ is convex. However, for the strongly anisotropic case, the sharp model 1.23 is ill-posed due to the lack of semi-continuity (Fonseca, 1992). Therefore an intrinsically regularized model is proposed in (Li and Maurini, 2019), the corresponding energy functional is given as:

$$\mathcal{E}_\ell(\boldsymbol{u}, \alpha) = \int_\Omega a(\alpha) W(\boldsymbol{u}) \mathrm{d}\Omega + \frac{G_0}{c_w} \int_\Omega \left(\frac{w(\alpha)}{\ell_0} + \ell_0^3 \, \mathbb{C} \, \nabla^2 \alpha \cdot \nabla^2 \alpha \right) \mathrm{d}\Omega \tag{1.42}$$

where $\nabla^2 \boldsymbol{\alpha}$ is the Hessian of the damage variable. Different from the model presented in (Li et al., 2015), this model incorporates a linear dissipation function and does not involve any first derivatives of the phase-field (damage functional depends only on the Hessian of the damage variable α). By incorporating these changes, the model can be simplified, leading to the attainment of an analytical solution for the optimal crack profile (Li and Maurini, 2019). To obtain a cubic symmetric surface energy, it requires three constants

of matrix $\mathbb{C}$: C_{11}, C_{12} and C_{44} (Voigt notation), besides the $\mathbb{C}$ need to be positive definite. The determination of these anisotropic constants will be discussed in Section 4.2.1. As a result, we obtained a four-fold symmetric model, and the orientation-dependent surface energy can be expressed as:

$$G_c(\theta) = G_0 \sqrt[4]{a \cdot (1 - A\cos 4\,(\theta - \theta_0))} \tag{1.43}$$

where $a = (3C_{11} + C_{12} + 2C_{44})/4$ and $A = (C_{11} - C_{12} - 2C_{44})/(3C_{11} + C_{12} + 2C_{44})$. θ_0 represents the direction of weakest plane, or refers as the material axis. The anisotropic coefficient for four-fold symmetric model A_f is defined as $A_f = |A|$ and it should be noted that $A_f \in [0, 1)$. To rotate the orientation-dependent $G_c(\theta)$, we transform the matrix $\mathbb{C}$ using eq. (1.44).

$$\hat{\mathbb{C}} = \mathbb{K}\,\mathbb{C}\,\mathbb{K}^T \tag{1.44}$$

In Voigt notation (Bower, 2009), $\mathbb{K}$ represents the transformation matrix for a fourth-order tensor in 2D:

$$\mathbb{K} = \begin{pmatrix} \cos^2(\theta_0) & \sin^2(\theta_0) & 2\cdot\cos(\theta_0)\cdot\sin(\theta_0) \\ \sin^2(\theta_0) & \cos^2(\theta_0) & -2\cdot\cos(\theta_0)\cdot\sin(\theta_0) \\ -\cos(\theta_0)\cdot\sin(\theta_0) & \cos(\theta_0)\cdot\sin(\theta_0) & \cos^2(\theta_0) - \sin^2(\theta_0) \end{pmatrix} \tag{1.45}$$

Fig. 1.8 displays the reciprocal surface energy in polar coordinate for two-fold and four-fold symmetric models. As the anisotropic coefficient increases, both models exhibit increasing anisotropy in the surface energy. However, the four-fold symmetric surface energy can become non-convex when $A_f > \frac{1}{3}$, violating the local convexity condition for certain ranges of angles as shown in eq. (1.24). Consequently, a 'forbidden direction' for the crack propagation can arise, resulting in a strongly anisotropic model.

Two-fold symmetry

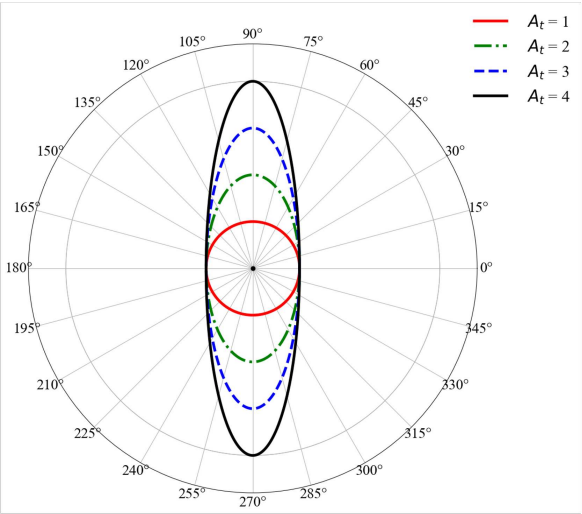

$$\frac{G_0}{G_c(\theta)} = \frac{1}{\sqrt{A_t{}^{-2}\sin^2(\theta) + \cos^2(\theta)}}$$

Four-fold symmetry

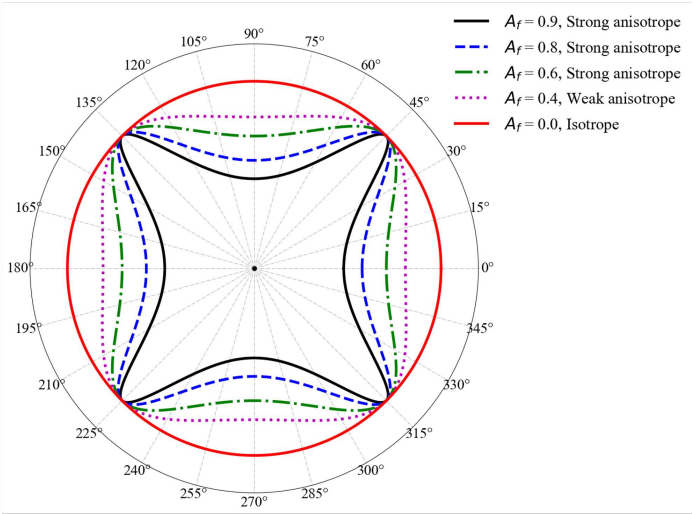

$$\frac{G_0}{G_c(\theta)} = \frac{1}{\sqrt[4]{1 - A_f \cos 4\left(\theta - \frac{\pi}{4}\right)}}$$

Figure 1.8 The illustration shows the reciprocal surface energy $\frac{G_0}{G_c(\theta)}$ in polar coordinates. The left side depicts a two-fold symmetric model eq. (1.41), while the right side shows a four-fold symmetric model eq. (1.43).

1.4.3.3 Multi-damage variable model

An alternative approach to obtain a strongly anisotropic model was employed by (Nguyen et al., 2017; Scherer et al., 2022). Their model involves the use of multi damage variables, where each variable represent a cleavage plane. This allows the model to remain a second-order model. The total energy functional is denoted as follows:

$$\mathcal{E}\left(\underset{\sim}{\boldsymbol{\varepsilon}}, \alpha_i, \nabla\alpha_i\right) = \frac{1}{2}\,\underset{\sim}{\boldsymbol{\varepsilon}} : \mathbb{A}\left(\alpha_i\right) : \underset{\sim}{\boldsymbol{\varepsilon}} + \sum_{i=1}^{m} \frac{3G_c^i}{8\ell_i}\left(\alpha_i + \ell_i^2 \underset{\sim}{\boldsymbol{B_i}} : \left(\nabla\alpha_i \otimes \nabla\alpha_i\right)\right) \tag{1.46}$$

where the damage-degraded stiffness tensor $\mathbb{A}\left(\alpha_i\right)$ can be expressed as follows:

$$\mathbb{A}\left(\alpha_i\right) = \left((1-\kappa)\prod_{i=1}^{m}\left(1-\alpha_i\right)^2 + \kappa_r\right)\mathbb{A} \tag{1.47}$$

where κ_r is a residual stiffness. The presence of second-order tensors $\underset{\sim}{\boldsymbol{B_i}}$ in the non-local term of Eq. (1.47) introduces the anisotropic setting, which can be expressed as follows

$$\underset{\sim}{\boldsymbol{B_i}} = \underset{\sim}{\boldsymbol{I}} + \beta_i\left(\underset{\sim}{\boldsymbol{I}} - \boldsymbol{n_i} \otimes \boldsymbol{n_i}\right) \tag{1.48}$$

Here the penalization parameter β is a key factor in determining the degree of anisotropy, with higher values leading to strongly anisotropic surface energy. The index i represent different fracture mechanism, with $i = 2$ the model corresponding to an fourth-fold symmetric model by setting the penalization parameter $\beta > 1$. Each damage variable can be regard as a cleavage plane. The fracture toughness G_c^i and regularization parameter ℓ_i are specific to each cleavage plane, which can be distinguished by the choice of normal vector $\boldsymbol{n_i}$. For example, $\boldsymbol{n_1} = \begin{bmatrix} 1\,, & 0 \end{bmatrix}$ corresponds to a vertical cleavage plane while $\boldsymbol{n_2} = \begin{bmatrix} 0\,, & 1 \end{bmatrix}$ represents a horizontal one. By using a rotation matrix, the orientation of the cleavage plane can be changed. Compared to the Li and Maurini 2019's higher-order model, this model provides more freedom in defining surface energy form, making it more suitable for modeling polycrystalline materials. Additionally, the model is more computationally efficient as it is a second-order model. However, in contrast to other anisotropic models that use the anisotropic constant in second or fourth-order tensors to change the degree of anisotropy by manipulating the ratio between the surface energy along the weak plane and the "forbidden direction", the physical meaning of the penalization parameter β in the multi-damage model is not clear (Scherer et al., 2022).

1.5 Motivation

LEFM is a comprehensive framework to treat the crack propagation if failure occurs in the elastic domain. For isotropic fracture toughness, the classic approach has been validated by several experiments (Erdogan and Sih, 1963; Ayatollahi et al., 2015, 2016). While for the phase-field model based on variational approach, it has been validated by comparing with fracture experiments in PMMA specimens (Pham et al., 2017; Cavuoto et al., 2022), experimental evidence has demonstrated the effectiveness of AT1 and AT2 phase-field models in accurately predicting intricate crack paths and stress state during the initial phase of crack formation. By employing the formula proposed by (Tanné et al., 2018), the regularization parameter ℓ can be computed using the material parameters, including Young's modulus E, critical surface energy G_c, and tensile strength σ_c. The utilization of the calculated regularization parameter ℓ in numerical experiments yields outstanding accuracy in providing quantitative predictions. As for the material with anisotropic fracture behavior, the classical based criteria GMERR has been validated by performing the experiments on tearing bi-oriented polypropylene sheets with strongly anisotropic fracture toughness, which resulted in a zig-zag crack patterns (Takei et al., 2013). Beside, the weakly anisotropic phase-field model is validated by conducting fracture experiments on orientationally ordered composites (Mesgarnejad et al., 2020). The inclusion of the

higher-order term T-stress was shown to be essential when applying the GMERR criteria, as demonstrated by their studies. For the regularization parameter, the same formula (Tanné et al., 2018) was employed, and it was observed that the phase-field model with the corresponding ℓ value, provided accurate predictions on the crack angle.

As for the strongly anisotropic phase-field model, despite the existence of the numerical models, until today, no one has validated these numerical models through experiments. The validation of anisotropic models is more complex compared to isotropic models, which is manifested in the following aspects: first the choice of the form of anisotropic surface energy with forbidden direction. As we know, it is almost impossible to guide the crack into a forbidden direction, hence, that surface energy form is impossible to obtain from fracture experiments. The only value that can measured is the G_c along the direction of weak plane. Such difficulty makes the selection of constants in the numerical model challenging. Second, the choice of the regularization parameter ℓ, as the higher-order phase-field is employed, there is a lack of knowledge that if the formulation to determine the ℓ for isotropic model (Pham et al., 2011; Tanné et al., 2018) holds for strongly anisotropic model. Furthermore, can ℓ be considered as an internal length parameter associated with the material? Does this regularization parameter have a connection with the macroscopic tensile strength σ_c, as well as the size of the microstructure (such as the size of the deposited filaments)? Also, should we take into account the effect of T-stress in cases where there is a strong anisotropic surface energy as in Mesgarnejad et al. 2020?

During my PhD, we aim to answer these questions for a particular material, namely PC printed by FDM with criss-cross printing pattern. The work consist of a part of fracture experiments and a part of numerical simulations using the classic approach and the strongly anisotropic phase-field model proposed in Li and Maurini 2019.

Chapter 2

Fracture experiments on FDM printed samples

This chapter is dedicated to the fracture experiments carried out on specimens made using Fused Deposition Modeling (FDM) process. It provides an overview on FDM process and its current application. The chapter then provides detailed information on the dimensions of the samples, the printing process using FDM, and the printing parameters and strategies employed. It also describes the pre-cracking procedure of the samples under cyclic loading before conducting fracture experiments, and the material parameters extracted from tensile tests. The experimental setup for fracture experiments and the post-processing methods used are also explained. The chapter concludes with the presentation of the experimental results, including the fracture experiments under mode I loading and mode I+II loading. Additionally, the critical surface energy of the weak plane will be calculated using the experimental results.

Contents

2.1 Fused Deposition Modeling

FDM is recognized as the most widely used technology of polymer-based additive manufacturing. It involves the use of thermoplastic filament to build components layer by layer, as illustrated in fig. 2.1. The main materials used in FDM include: Polylactic acid (PLA), Acrylonitrile butadiene styrene (ABS), PC or Polyamide (PA). FDM was initially used for rapid prototyping due to its ability to quick design, manipulate, and print complex geometries. In recent years, it has become more mature and widely used in industrial production with the advancement of materials and technology.

FDM has been employed in various industries, including the automotive industry for the production of components such as front frame covers, aerodynamic elements, and air scoops (Gechev, 2022). It has also found applications in the medical industry for the fabrication of biomedical implants (Singh et al., 2018). Additionally, FDM has been used in the aerospace industry, with the FDM-manufactured antenna array supports for FormoSat-7/COSMIC-2 satellite mission successfully proven to be functional in outer space (cqadmin, 2015).

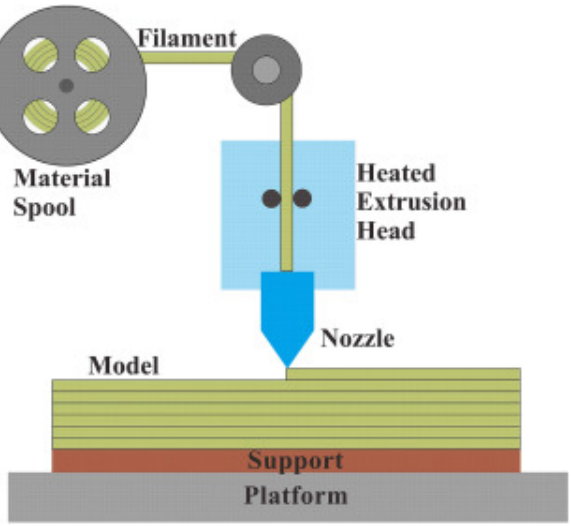

Figure 2.1 Schematic of the standard FDM process (Zou et al., 2016)

However, the FDM still faces some challenges, including anisotropic elasticity and void formation in printed components due to the layer-by-layer printing process, which can significantly affect their mechanical properties. Meanwhile, the fracture behavior of printed parts is a critical concern, as it directly affects the reliability and performance of printed parts during their life service. Due to the complexity of analyzing the factors influencing the mechanical and fracture behavior of the printed parts, numerous studies have been conducted in this area, focusing on different printing parameters such as: raster pattern orientation (Ahn et al., 2002; Cantrell et al., 2017; Ayatollahi et al., 2020), build orientation (McLouth et al., 2017; Marșavina et al., 2022), thickness and extrusion nozzle type (Maloch et al., 2018), bed temperature and nozzle temperature (Aliheidari et al., 2018), bonding features (Allum et al., 2020), printing speed (Kizhakkinan et al., 2022; Rezaeian et al., 2022) and deposition strategy (Gardan et al., 2018). For readers interested in fracture behavior, refer to the review paper of Khosravani et al. 2020, and for fatigue behavior, refer to Shanmugam et al. 2021.

The literature listed previously has primarily focused on studying the influence of printing parameters on fracture toughness and fatigue life of printed samples, particularly in terms of the material's ability to endure crack initiation and propagation. However, the unique advantages of AM such as design freedom (Ngo et al., 2018) and the ability to easily modify the microstructure, can result in a specific microstructure that leads to anisotropic fracture toughness. From an engineering standpoint, such microstructure is valuable as it provides guidance for the design of mechanical components with controlled crack propagation and facilitates more accurate nondestructive testing for locating potential damage.

Despite the potential benefits of microstructure modification in FDM, there is a lack of scientific research investigating how crack propagates in the printed solids with varying microstructure. Gardan et al. 2018 reported an optimised deposition technique that altered the fracture behavior of printed samples, resulting in a ductile-like behavior. Similarly, Kizhakkinan et al. 2022 reported a change in fracture behavior from brittle to ductile by adjusting the printing speed. These studies employed a strategy that transformed the fracture behavior of the printed samples from brittle to ductile, thereby enabling increased energy absorption and delayed structural failure.

In Corre and Lazarus 2021, they involved adapting a criss-cross printing pattern, which is able to guide and stabilize the crack propagation in printed PC sample, even the fracture behavior remains brittle. In this dissertation, we build upon the work of Corre and Lazarus 2021 by employing different geometries with the same printing pattern to investigate crack extension under various loading modes.

In this thesis, the main point is not to study the impact of different printing strategy on fracture resistance as in the paper cited above. Instead we consider FDM as a versatile and low cost way to design experiments to test fracture propagation models. As in Corre and Lazarus 2021, we adopt a criss-cross printing pattern and PC material to enter in the framework of isotropic linear elasticity with anisotropic fracture toughness.

2.2 Experimental protocol

Fracture experiment was performed on printed Compact Tension (CT Mode I) and Compact Tension Shear (CTS Mode I+II) specimens, using the identical criss-cross printing pattern as detailed in Corre and Lazarus 2021. Based on the experimental observations, the printed samples exhibited an anisotropic behavior in fracture toughness under mode I loading. The experimental setup used in previous study Corre and Lazarus 2021 was enhanced by incorporating a pre-crack though cyclic loading and by employing a new printing device (Raise3D Pro2) instead of the Raise3D N2 Plus. Our aim is to systematically investigate the fracture behavior of printed samples under different fracture mode (Mode I and Mode I+II). The displacement fields measured using Digital Image Correlation (DIC) method were post-processed to obtain the fracture parameters. The critical energy release rate G_c along the weak plane will be determined using the extracted SIFs during the crack propagation.

2.2.1 Sample preparation

2.2.1.1 Material used and printing process

The samples were fabricated with Fused Deposition Modeling using a Polycarbonate-based filament ($PC-Plus^{TM}$ from Poly-maker, diameter of filament 1.75 mm). A digital model of the sample was created using CAD software Fusion 360, based on their dimensions. The exported STL file was imported into Ideamarker and sliced layer by layer to generate a Gcode file, which contains printing actions, such as nozzle trajectory and temperature settings. The 3D printer used for printing was the Raise 3D Pro2, which read the Gcode file and executed the printing program. Prior to the printing process, the build platform was preheated to 100 °C for one hour to ensure a uniform temperature across the 3D printer. Furthermore, the warm-up process helped to prevent strong adhesion between the build platform and samples, which could potentially damage the platform when removing the samples after printing. Besides, in order to avoid warping and increase bed

adhesion, we start with printing a raft with 5 layers, which ensure proper calibration of the first layer and maintain a close proximity between the print and the bed.

The printing process begins by heating the nozzle to 260 °C, and extruding a continuous filament of Polycarbonate through a 0.4 mm diameter nozzle. The PC material is heated to a semi-liquid state and then deposited onto the platform or previous layers by moving the nozzle. As time passes, the deposited material gradually cools down and solidifies, ultimately bonding with the previously deposited thread. The printing speed for infilling the sample is 50 mm/s as suggested as Poly-maker (30-50 mm/s) and it is important to note that the cooling fan of the nozzle should be turned off during the printing. Furthermore the extruder's filament flow rate of is set to 98 %. Over-extrusion is a common issue in FDM printing that can negatively affect print quality. To address this problem, it's crucial to calibrate the printer by comparing the required extruded material to the actual extruded material. Additionally, factors such as the extruder speed for retraction and the amount of retraction need to be considered to avoid over-extrusion, which often leads to faint strings or wisps along the nozzle's path between points. In our case, the retraction speed is set to 40 mm/s, and the amount is 2.5 mm, as determined through printing a specific sample.

2.2.1.2 Geometries of CT and CTS samples

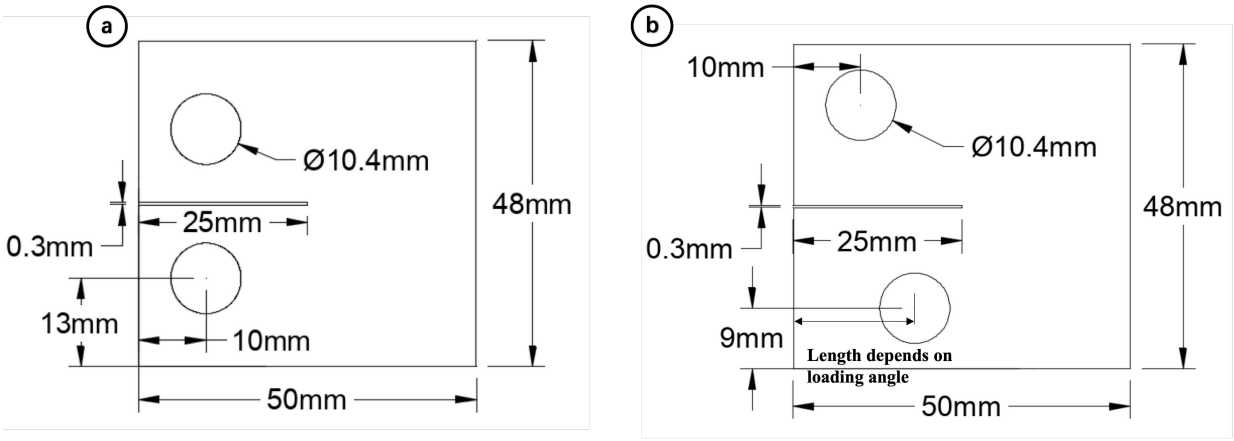

Figure 2.2 The dimensions of the specimens are as follows: a) CT sample, and b) CTS sample

To investigate the fracture behavior of 3D printed samples, CT (Mode I) and CTS (Mode I+II) sample were used. The dimensions of CT and CTS sample were illustrated in fig. 2.2. The printed CT and CTS sample are depicted in fig. 2.3 (a), (b) (c) and (d).

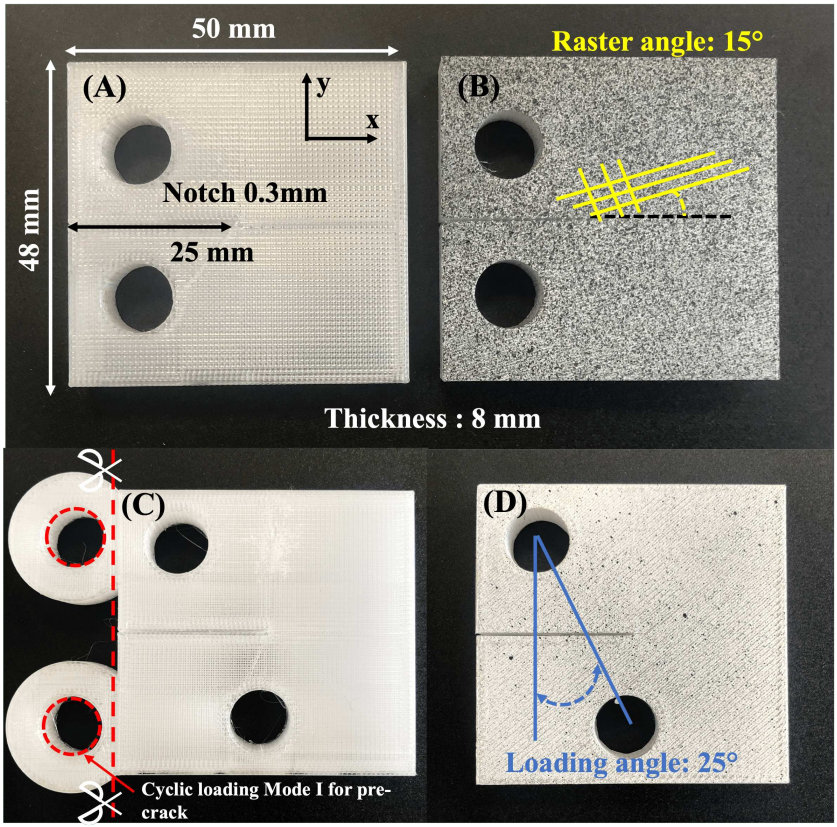

Figure 2.3 a) Dimensions of CT sample, b) CT sample with a speckle pattern for DIC analysis, c) CTS sample with adjoined pin hole to create a pre-crack for mode I fatigue loading and d) CTS sample after cyclic loading with pre-crack, mode I pin holes are removed

2.2.1.3 Printing strategy of CT and CTS sample

The printing strategy described in Corre and Lazarus 2021 was used, where each layer was filled with a selected infill angle or raster angle (angle of deposited material with respect to the notch), and successive layers were arranged orthogonally to each other. Each layer had a thickness of 0.15 mm and a fill rate of 100 % was applied. An outer shell enclosed the printing sample at each layer. Fig. 2.4 shows the printing strategy for the CT sample. To facilitate the fracture experiments, the shell near the crack tip was removed by systematically modifying the Gcode file using a python script (see appendix B).

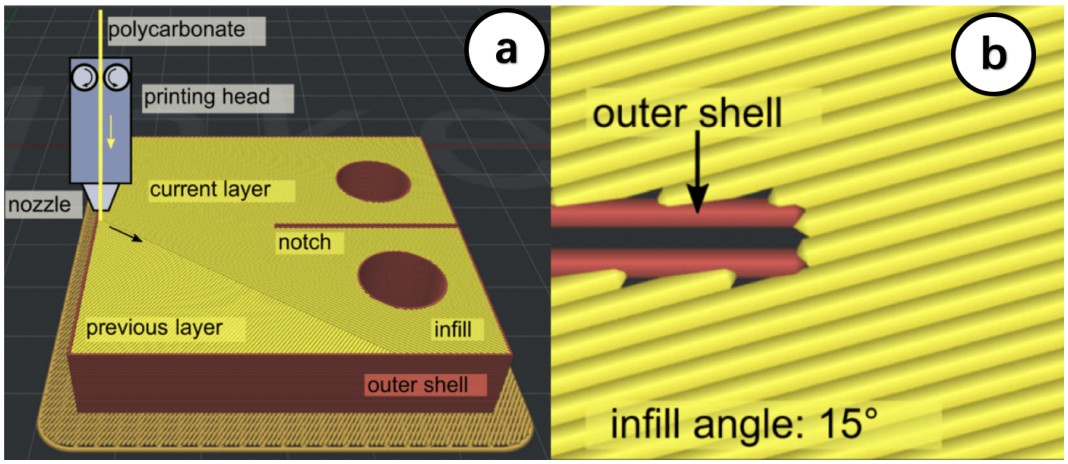

Figure 2.4 Ideamarker preview: a) shows the trajectory of the nozzle when printing a CT sample, and b) presents a closer view near the crack tip where the shell is removed at the notch extremity (Corre and Lazarus, 2021)

2.2.1.4 Pre-cracking under cyclic loading

During the printing process of CT and CTS sample, the nozzle moves near the crack tip to start printing a new layer, resulting in a more complex microstructure in the vicinity of the crack tip than initially expected. To address this issue, a pre-crack was created under mode I loading using an Instron ElectroPlus 3000 Dynamic test instrument. The specimens were subjected to a sinusoidal force at a frequency of 3 Hz, with the maximum and minimum amplitudes of the force detailed in Table 2.1. After 20000 cycles, a pre-crack of approximately 1.5 mm length was initiated. The presence of a pre-crack helps to stabilize the crack propagation, particularly under Mode I+II loading conditions. Indeed, we observed that in the absence of the pre-crack, a significant number of experiments occurred in an uncontrolled manner: once crack propagation began, it would dynamically propagate until failure. However, with the inclusion of the pre-crack, we were able to exert control over the propagation in the majority of experiments. When propagation initiated, it occurred quasi-statically as the displacement was gradually increased. It is important to note that the Mickey ears on fig. 2.3(c) served to initiate a mode I fatigue pre-crack for the CTS sample, and they were removed (d) prior to conducting the fracture test.

Table 2.1 Table of maximal and minimal force used in the pre-crack procedure

Details of pre-cracking procedure		
Sample	Maximal force (N)	Minimal force (N)
CT sample	240	80
CTS sample	160	60

2.2.1.5 Speckle pattern for DIC analysis

To perform DIC analysis, the specimens were coated with a pattern of speckles. This allowed for tracking the movement of small pixels on the specimen's surface by comparing images taken before and after deformation. By analyzing these images, the displacement and strain fields of the specimen could be accurately measured.

The specimens were first sprayed with a matte white background using paint spraying (from COLORJELT), ensuring complete coverage of the surface. After the white base dried, we used an airbrush with a 0.3 mm nozzle to spray black speckles (from CREATEX) onto the surface. The use of an airbrush enabled consistent sizing of the black speckles, ensuring a uniform appearance on the surface.

2.2.2 Mechanical tests

Fracture tests were carried out using an Instron 5596 tensile machine, with a 0.5 $mm.min^{-1}$ displacement on the bolt in upper pin hole and the lower side remained fixed. The experiment was captured using a Nikon D300s camera with an AF-S Micro NIKKOR 60 mm lens, resulting in a physical pixel size of 20 μm. The experimental setup is illustrated in the Fig. 2.5. During the experiment, the control of data collection and camera instructions was facilitated by Arduino, an open-source electronics platform. At intervals of approximately 4-6 seconds, a greyscale image with dimensions of 4288x2848 pixels was captured. Concurrently, the corresponding displacements and forces were measured by a 30KN load cell on the load head, and these values were recorded and transmitted as analog signals through Arduino to the computer via a USB port. To visualize the transmitted data, CoolTerm, a software designed for communicating with serial devices via USB, was utilized. CoolTerm enabled the display and monitoring of the received data on the computer screen, allowing for real-time observation.

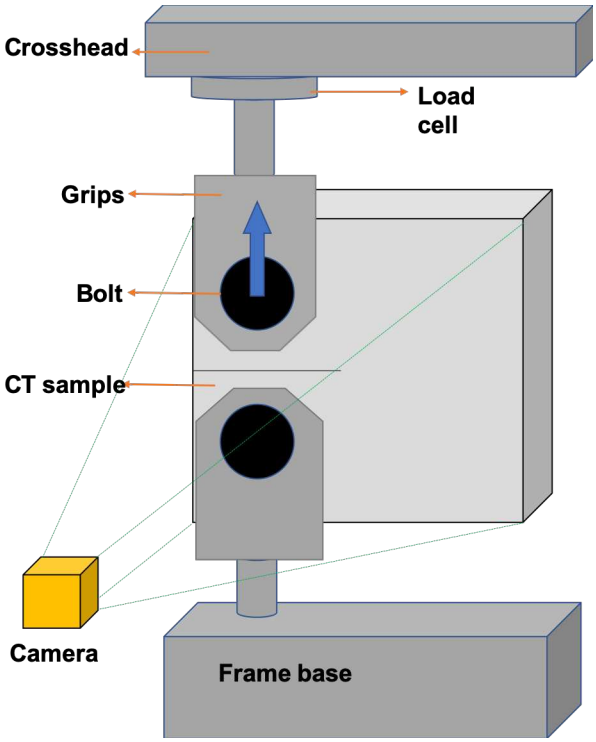

Figure 2.5 Fracture experimental setup

The elastic properties of printed sample were determined using 15 tensile specimens with five raster angles (0°, 10°, 15°, 25° and 45°). The dimensions of the tensile specimen are illustrated in fig. 2.6. The tensile test was monitored using the same equipment as described previous. The tensile tests were conducted with a displacement rate of 0.5 mm/min.

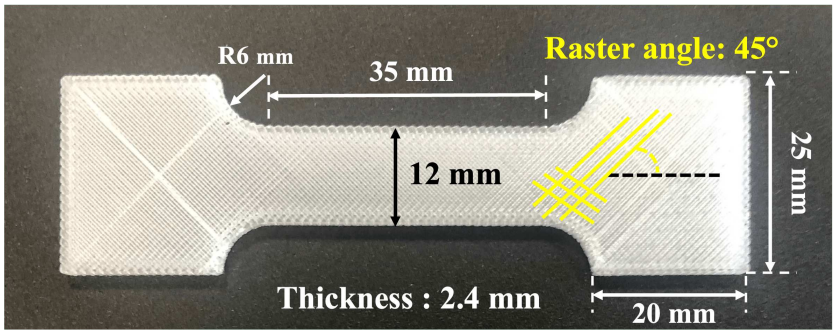

Figure 2.6 Tensile sample with 45° raster angle used for the determination of material properties

2.2.3 Post-processing by digital image correlation

The displacement and strain of the specimen surface were measured using speckle image tracking. To extract the fracture mechanics parameters, we used UFreckles20, an open-source software for DIC [1] (Roux et al., 2009; Réthoré, 2015; Corre and Lazarus, 2021). The post-processing involves the projection of the measured displacement field near the crack tip within the extraction domain onto the Williams series Eq (2.1):

$$\boldsymbol{u}(r,\theta) = \sum_{n=-\infty}^{\infty} a_I^n \psi_I^n(r,\theta) + a_{II}^n \psi_{II}^n(r,\theta) \tag{2.1}$$

where a_I^n and a_{II}^n are the asymptotic coefficients. The functions $\psi_I^n(r,\theta)$ and $\psi_{II}^n(r,\theta)$ are defined as follows:

$$\psi_I^n(r,\theta) = r^{n/2}\left(\kappa e^{in\theta/2} - \frac{n}{2}e^{i(4-n)\theta/2} + \left(\frac{n}{2} + (-1)^n\right)e^{-in\theta/2}\right)$$
$$\psi_{II}^n(r,\theta) = ir^{n/2}\left(\kappa e^{in\theta/2} + \frac{n}{2}e^{i(4-n)\theta/2} - \left(\frac{n}{2} - (-1)^n\right)e^{-in\theta/2}\right)$$

where κ is the Kolossov's constant, with $\kappa = (3-\nu)/(1+\nu)$ for plane stress assumption, $\kappa = (3-4\nu)$ for plane strain assumption, and ν is the Poisson's ratio.

In practice, it is adequate to extract the lower order coefficients such as the SIF and T-stress by selecting n values ranging from -3 to 7 (Réthoré, 2015). The extraction domain is a disk-shaped region with a radius denoted as r_{ext}, centered on the crack tip. A small region with a radius of r_{int} is removed from the extracted domain near the crack tip and along the lip of the crack. The parameters of extracted domain are $r_{ext} = 160$ pixels and $r_{int} = 32$ pixels, corresponding to 3.2 mm and 0.64 mm, respectively. A crack path is proposed based on the discontinuity of the measured displacement to aid in the detection of the crack tip. Subsequently, the displacement field of the extracted domain is projected onto the Williams series to obtain the asymptotic coefficients. Finally, the fracture mechanics parameters SIF and T-stress can be computed using the obtained asymptotic coefficients as follows:

$$K_I = 2\mu\sqrt{2\pi}a_I^1, \quad K_{II} = 2\mu\sqrt{2\pi}a_{II}^1, \quad T = 2\mu\sqrt{2\pi}a_I^2 \tag{2.2}$$

As mentioned in the study by Corre and Lazarus 2021, the SIF obtained using DIC in the vicinity of a kink position may be inaccurate due to the presence of an angular point in the crack path. The region where the inaccuracy of SIFs is observed is influenced by

[1] Link UFreckles: https://zenodo.org/record/1433776

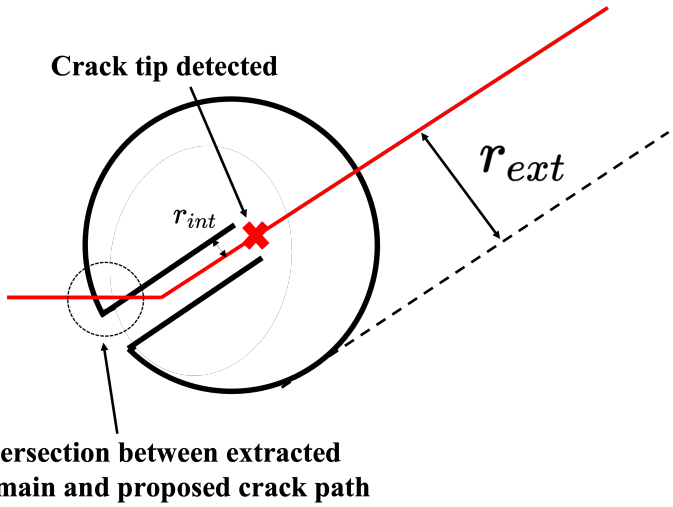

Figure 2.7 Schematic: Overlap region between the extraction domain and the proposed crack path (in red)

the selected value of r_{ext}, as illustrated in fig. 2.7, this occurs because of the intersection between the proposed crack path and the extraction domain.

2.2.4 Plane stress or Plane strain hypothesis

Inspired by the methodology outlined in Triclot et al. 2023, we performed a comparative analysis of the SIF between experimental and theoretical data. The calculation of the SIF for standard CT (Compact Tension) tests is determined using the norm specified in (ASTM, 1820).

$$K_I = \frac{F}{e\sqrt{W}} \frac{\left(2+\frac{a}{W}\right)\left(0.886+4.64\frac{a}{W}-13.32\left(\frac{a}{W}\right)^2+14.72\left(\frac{a}{W}\right)^3-5.6\left(\frac{a}{W}\right)^4\right)}{\left(1-\frac{a}{W}\right)^{3/2}} \tag{2.3}$$

In accordance with the provided equation, where F represents the applied load, e denotes the thickness, and W represents the width of the CT sample measured from the load line to the right edge, the fracture toughness K_{IC} can be determined by substituting the critical load F_c.

For the experimental investigations, three CT samples were employed, all having a raster angle of 0° to ensure mode I loading for crack propagation. Fig. 2.8 illustrates a comparison between the SIF K_I obtained through DIC under plane stress assumption and the average fracture toughness K_{IC} (grey zone). The average value of fracture toughness

K_{IC} were computed using eq. (2.3) for these three CT samples.

Observations reveal that during the crack propagation phase, the measured K_I obtained through DIC under the assumption of plane stress demonstrates good agreement with the computed fracture toughness K_{IC} employing the critical load and 8 mm thickness. These results indicate that the 2D plane stress assumption is suitable for a CT sample with 8 mm thickness as it was for 5 mm thickness samples (Triclot et al., 2023). Consequently, the plane stress assumption was adopted for further analysis.

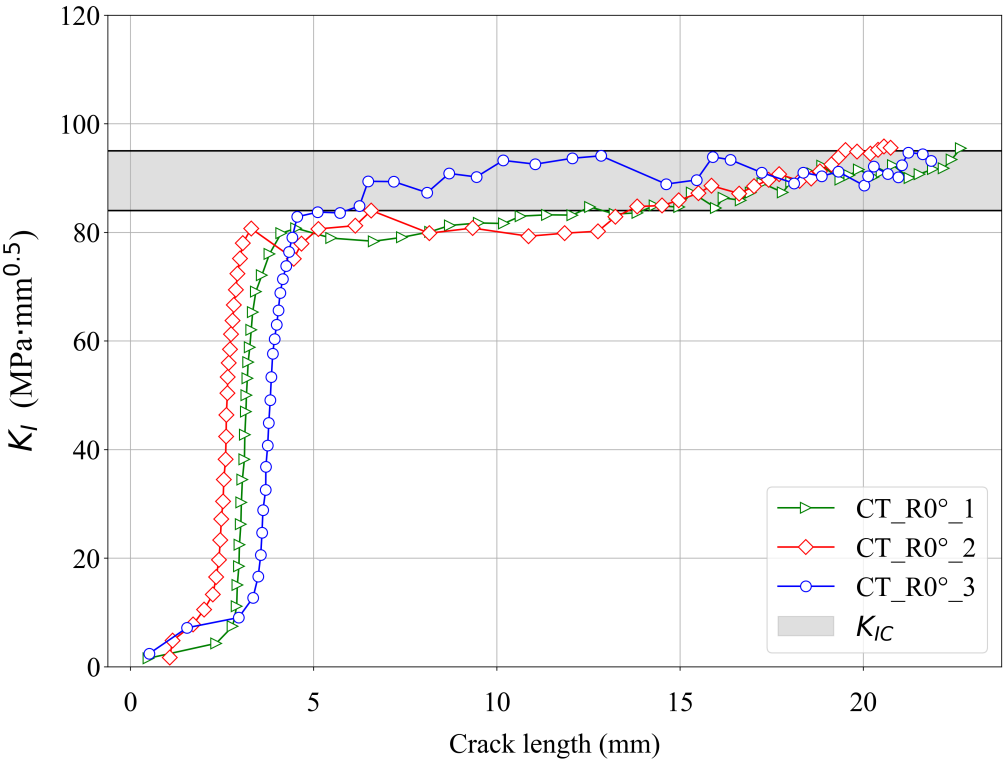

Figure 2.8 A comparison between the SIF K_I measured by DIC assuming plane stress (as a function of the crack length) and the computed average value of K_{IC} using eq. (2.3) for these three CT samples.

2.3 Experimental results

2.3.1 Elasticity properties

2.3.1.1 Tensile test

The strain results (ε_{xx}, ε_{yy} and ε_{xy}) were extracted from a rectangle zone centered on the tensile specimens, analogous to attaching a strain gauge to the surface of the sample as shown in fig. 2.9. The Young's modulus was determined by performing a linear fit of the data up to 0.8% longitudinal deformation ε_{yy}. For Young's modulus, the nominal stress σ_{yy} was plotted against longitudinal deformation ε_{yy} as shown in fig. 2.10(left). While for Poisson's ratio, the transverse strain ε_{xx} was plotted against longitudinal strain ε_{yy} as shown in fig. 2.10 (right). Fig. 2.11 shows the results of tensile tests with different raster angle obtained by linear fit of experimental data. As reported in (Corre and Lazarus, 2021), the printed samples exhibited nearly isotropic behavior in elasticity. It is evident that the Young's modulus value is nearly unaffected by the raster angle. However, for the Poisson's ratio, there is a higher dispersion in the measurements, possibly due to surface effects caused by inadequate printing of the first layer. Based on the study conducted by Corre and Lazarus 2021, we adopt the assumption that our printed material possesses isotropic elasticity, and the measured Young's modulus E and Poisson ratio ν for the tensile sample were 1890 MPa (standard deviation 111 MPa) and 0.34 (standard deviation 0.07) respectively. The critical stress, denoted as σ_c, was determined by measuring the normal stress at the point of rupture, which was found to be 42 MPa with a standard deviation of 2 MPa. These results are consistent with the values reported in Corre and Lazarus 2021 and the material properties provided by the supplier.

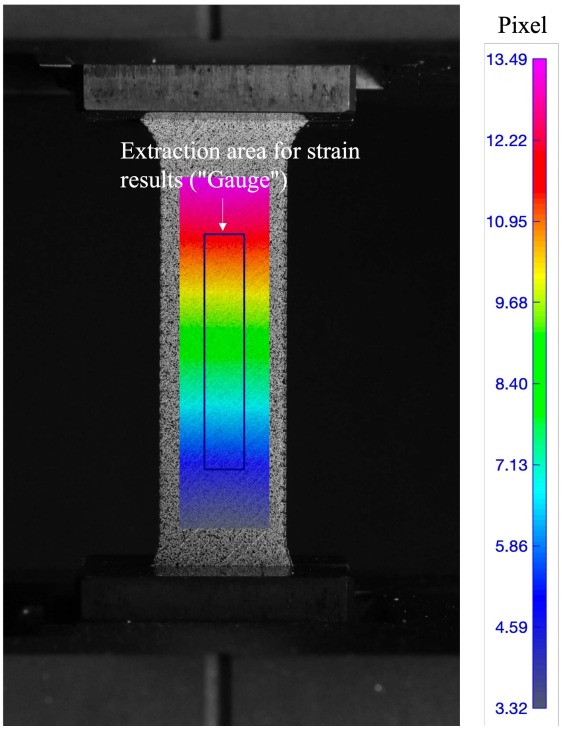

Figure 2.9 The measured displacement field along the y-axis (during the linear phase) of the tensile sample with a 45° raster angle. The rectangular area, positioned at the center of the tensile specimen, represents the designated extraction zone for obtaining strain results.

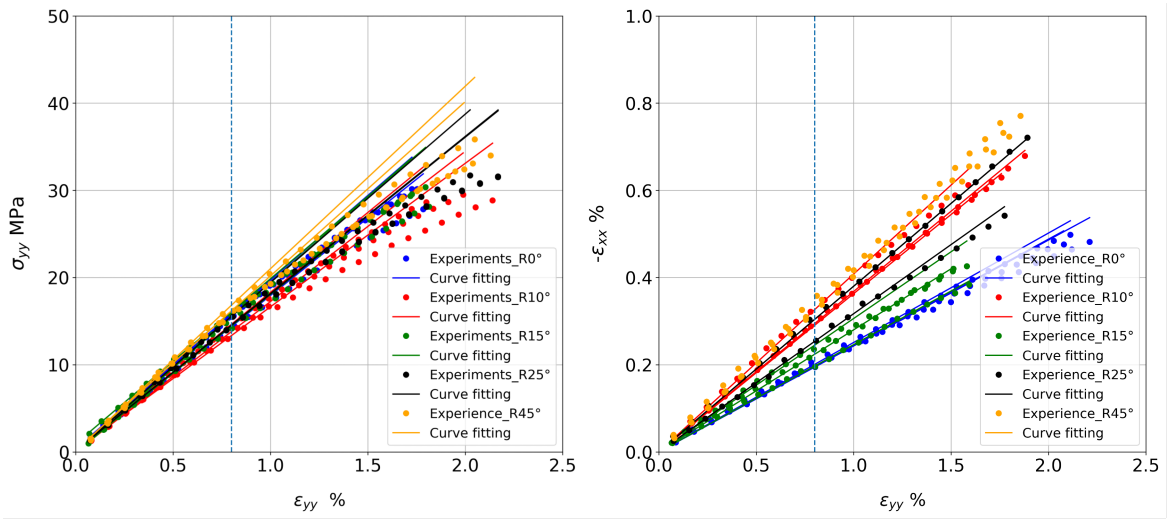

Figure 2.10 The results of the tensile test are presented as follows: on the left side, is the plot showing the nominal stress σ_{yy} plotted against the longitudinal deformation ε_{yy}. On the right side, is a plot displaying the transverse strain ε_{xx} plotted against the longitudinal strain ε_{yy}.

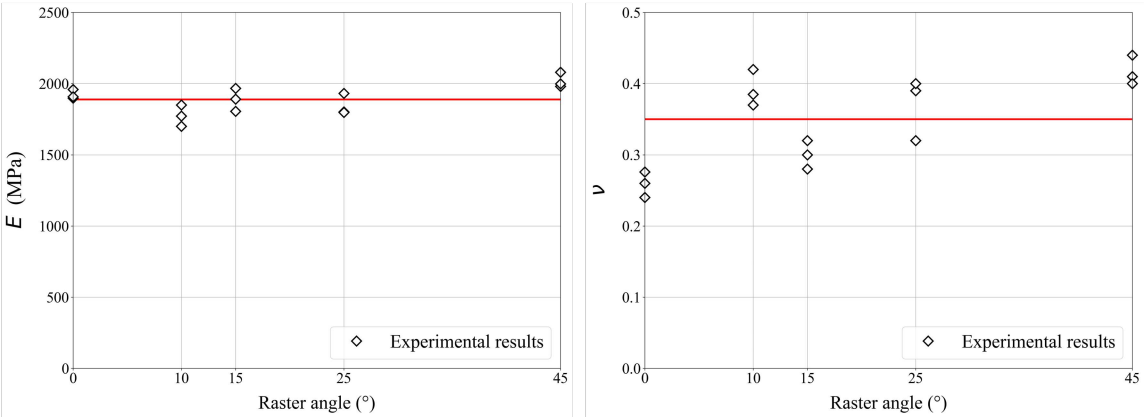

Figure 2.11 Results for tensile test: left and right represents measured Young's modulus E and Poisson's ratio ν with respect to the raster angle

2.3.2 Crack evolution in CT and CTS samples

In Figure 2.12, the crack tip of a CT sample with a 25° raster angle is shown at the point where kinking occurs. Prior to the crack kink, with increasing displacement, it was observed that there was a brief period of straight propagation, followed by kinking when the maximum force or critical force was reached. Fig. 2.13 illustrates the crack path and evolution of SIFs for CT sample with a 25° raster angle. It was observed that K_I increased almost linearly until the propagation threshold was reached, after which the crack kinked in the direction of the raster angle. Fracture experiments were conducted for various raster angles, including: 0°, 5°, 15°, 25°, 35° and 45°. From the mode I fracture tests, it was observed that the crack propagation consistently followed the deposited thread, aligning with the direction of the raster angle, which corresponds to the 'weak plane' as depicted Fig. 2.14.

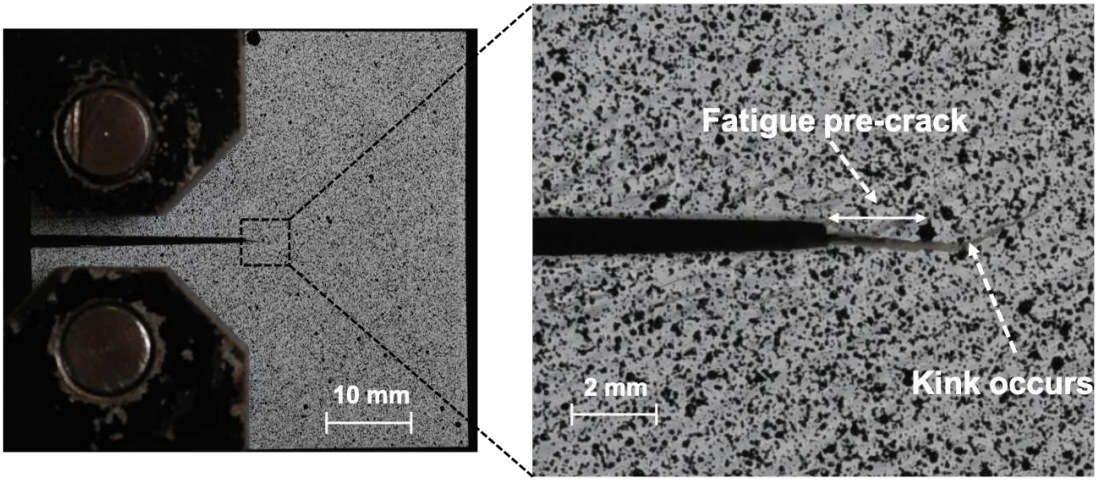

Figure 2.12 CT sample with 25° raster angle: the left image shows the CT sample when crack kink occurs, while the right image zooms in the crack tip

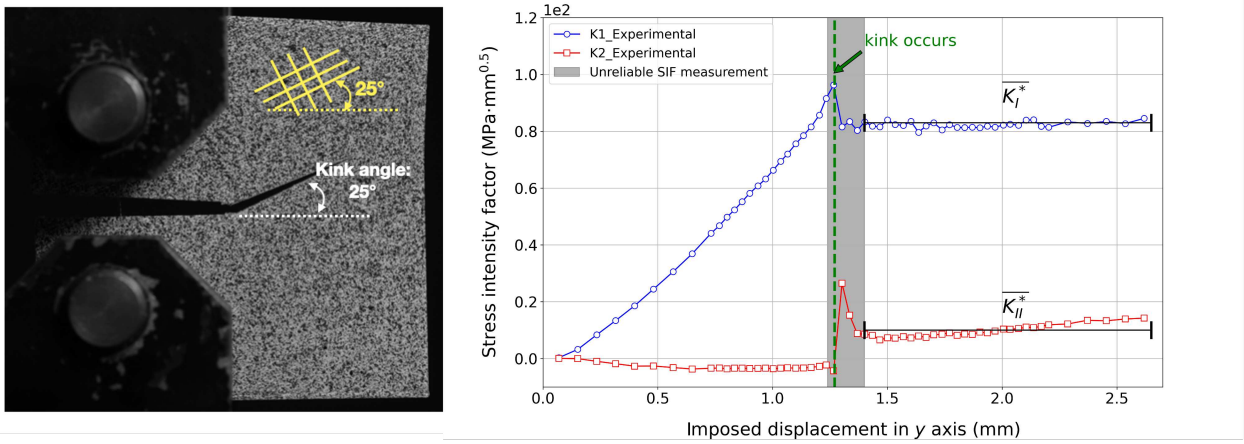

Figure 2.13 Experiment results of CT sample with 25° raster angle: the left image displays a kinking crack following the printed direction in a CT sample with corresponding experimental setup, while the right image shows the evolution of the SIF related to the imposed displacement along y axis. The grey zone signifies unreliable measurements due to the occurrence of a crack kink.

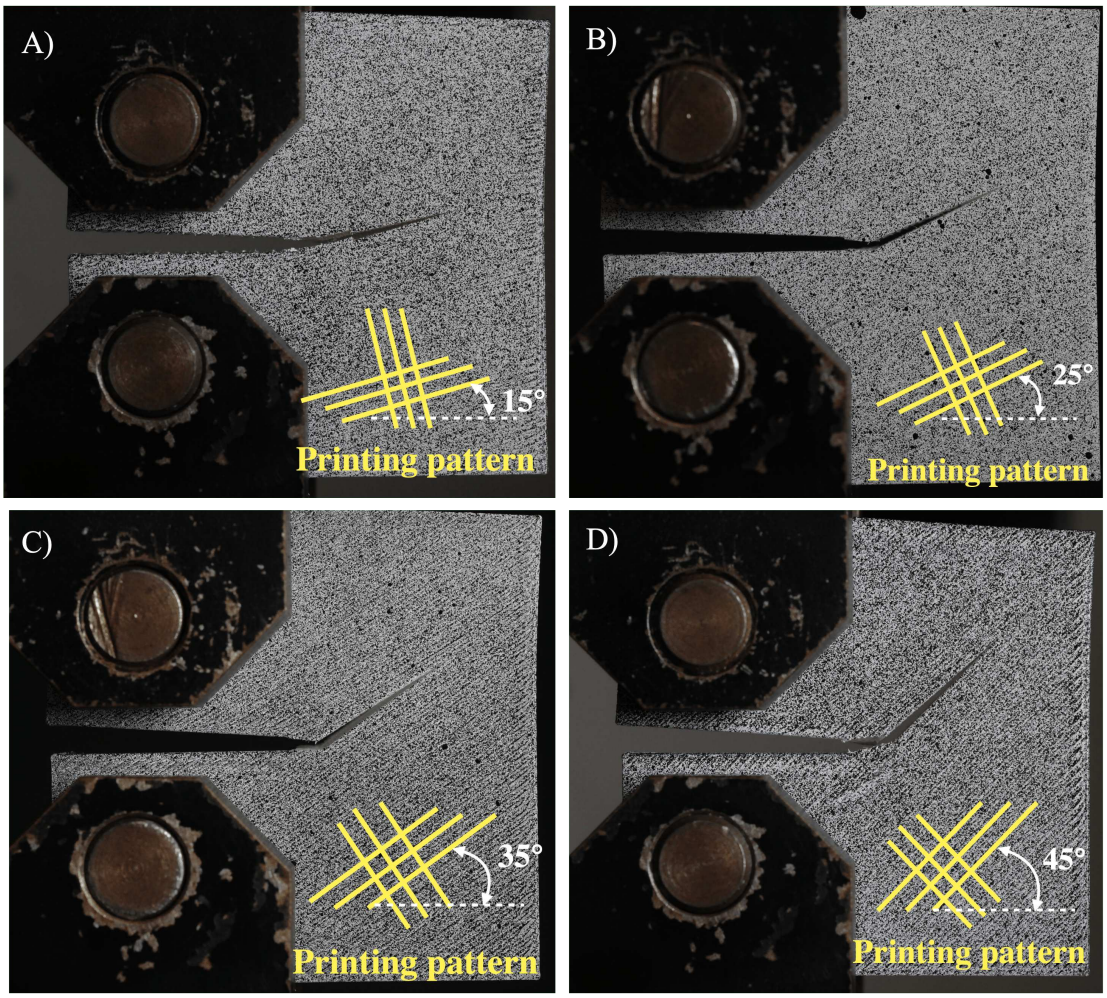

Figure 2.14 CT samples with different raster angle: A) 15°, B) 25°, C) 35° and D) 45°.

To ensure that the crack propagation remains unaffected by the loading condition, we further investigated the mode I+II fracture problem using CTS samples. The mode I+II fracture experiments were carried out for various raster angle and loading angle (5°, 15°, 25°, 35°). Fig. 2.15 illustrates the crack path and evolution of SIFs for CTS sample with a 40° raster angle and a 15° loading angle (represented by the blue dash line). Notably, irrespective of the loading conditions and the raster angle, the crack could only propagate along the printing direction as shown in fig. 2.16, which we refer to as the "weak plane" direction. This observation, combined with the experimental findings in the CT sample, clearly indicate that, regardless of the loading condition, the crack propagates exclusively in the weak direction, strongly suggesting that propagation in other directions is prohibited in the printed samples with criss-cross printing pattern.

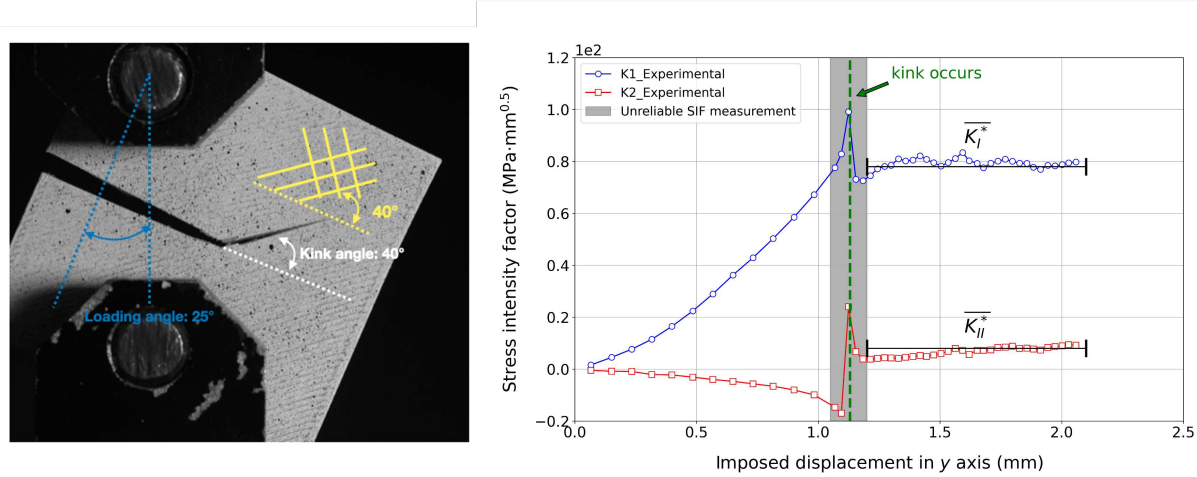

Figure 2.15 Experiment results of CTS sample with 40° raster angle and 25° loading angle: the left image displays a kinking crack following the printed direction in a CTS sample with corresponding experimental setup, while the right show the evolution of the SIF related to the imposed displacement along y axis. The grey zone signifies unreliable measurements due to the occurrence of a crack kink.

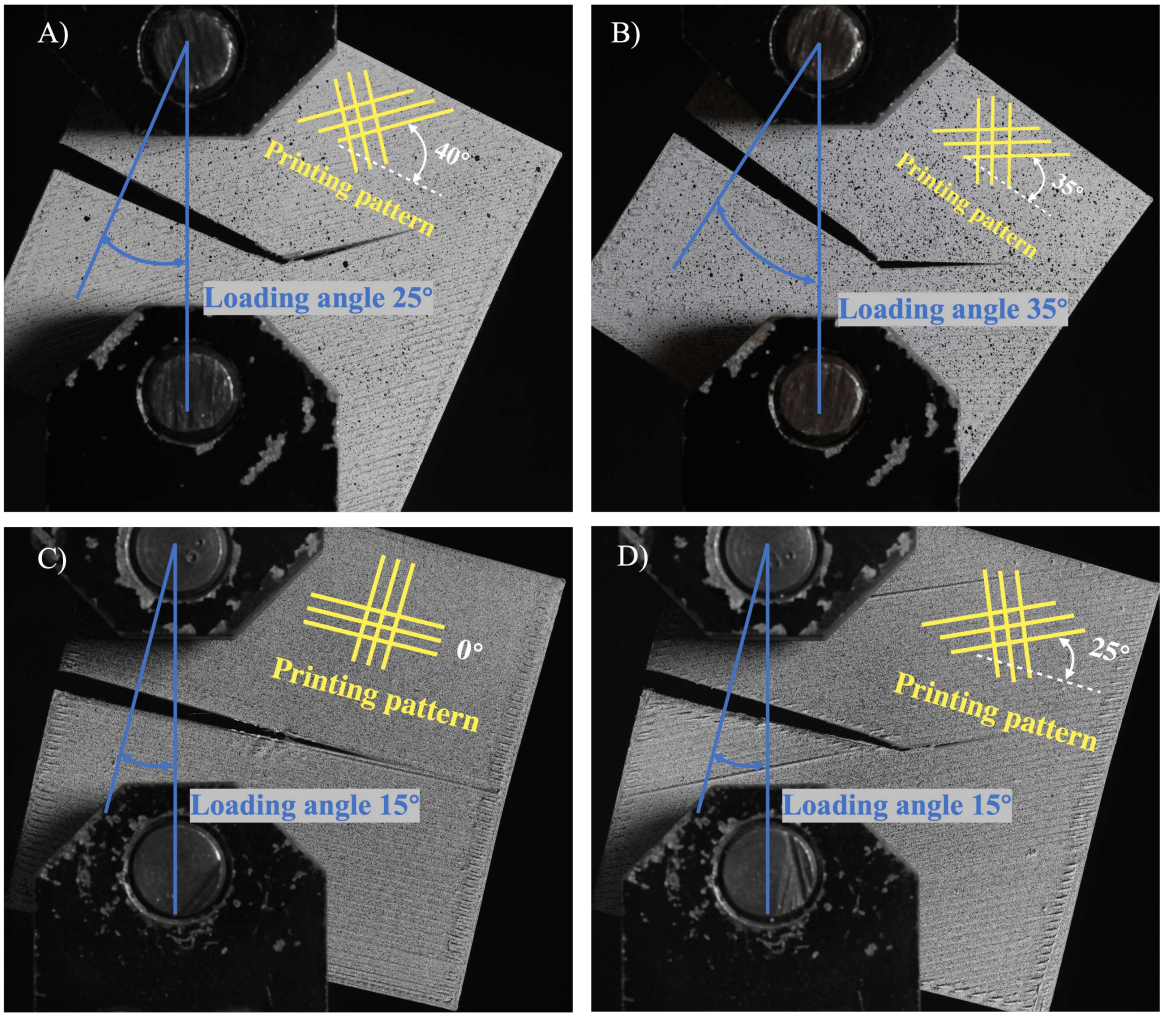

Figure 2.16 CTS samples with different raster angle and loading angle: A) raster angle 40° and loading angle 15°, B) raster angle 35° and loading angle 35°, C) raster angle 0° and loading angle 15° and D) raster angle 25° and loading angle 15°.

2.3.3 Evolution of critical force with different raster angle

Fig 2.17 illustrates the load curve for a CT sample with raster angles of 0°, 15°, 25°, and 45°. The crack exhibits a change in direction when it reaches its critical force. Subsequently, the force decreases as the crack propagates along the weak plane. The majority of the samples exhibit stable propagation after pre-cracking. Notably, the critical force increases as the raster angle increases. To gain a more comprehensive understanding from an experimental perspective, three fracture tests were conducted for each raster angle.

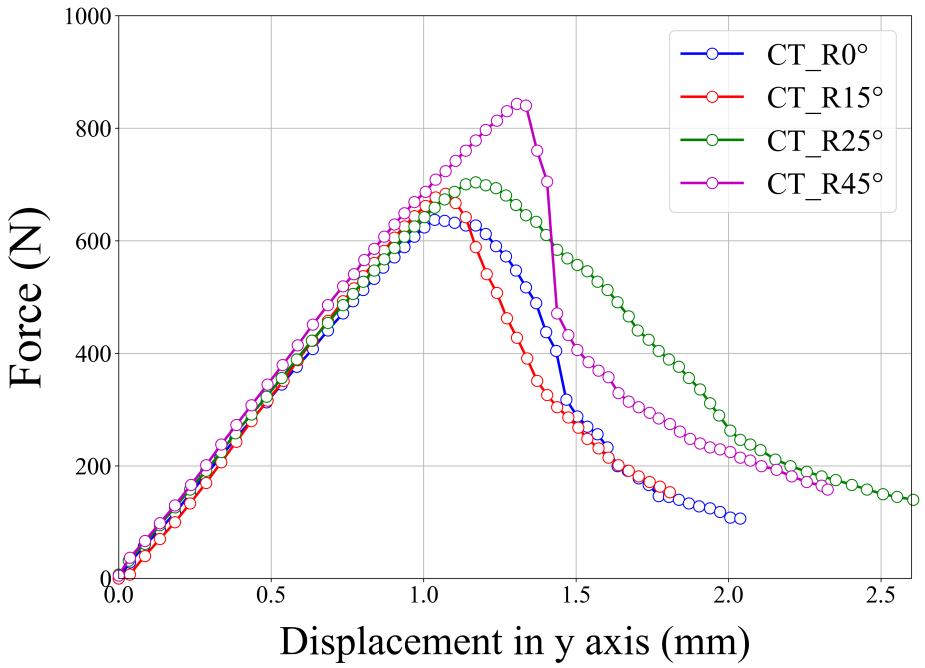

Figure 2.17 Load curve for CT sample with different raster angle.

Figure 2.18 illustrates the relationship between the critical force of the CT sample and the raster angle. Interestingly, it can be observed that the critical force exhibits a monotonically increasing trend as the raster angle increases.

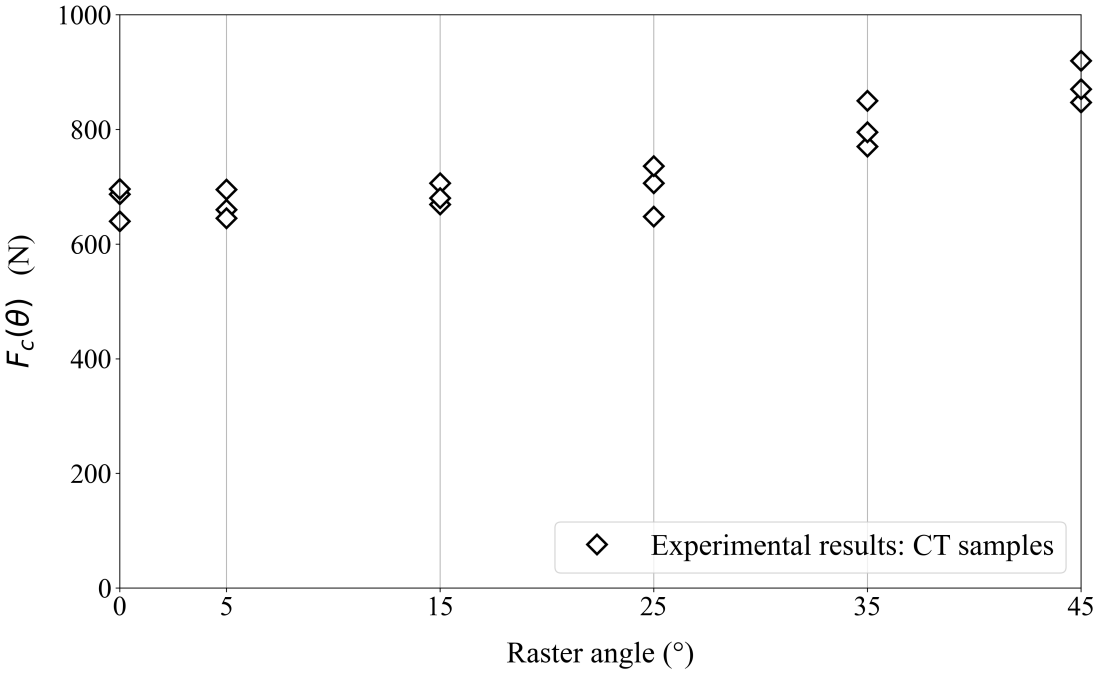

Figure 2.18 Experimental critical load of CT samples with respect to raster angle

We then investigated the critical force of CTS sample using 15° loading angle and various raster angle (0°, 15°, 25°, 35°, 45°). It is noteworthy that the critical force exhibits a non-monotonic variation with the difference between the loading angle and raster angle.

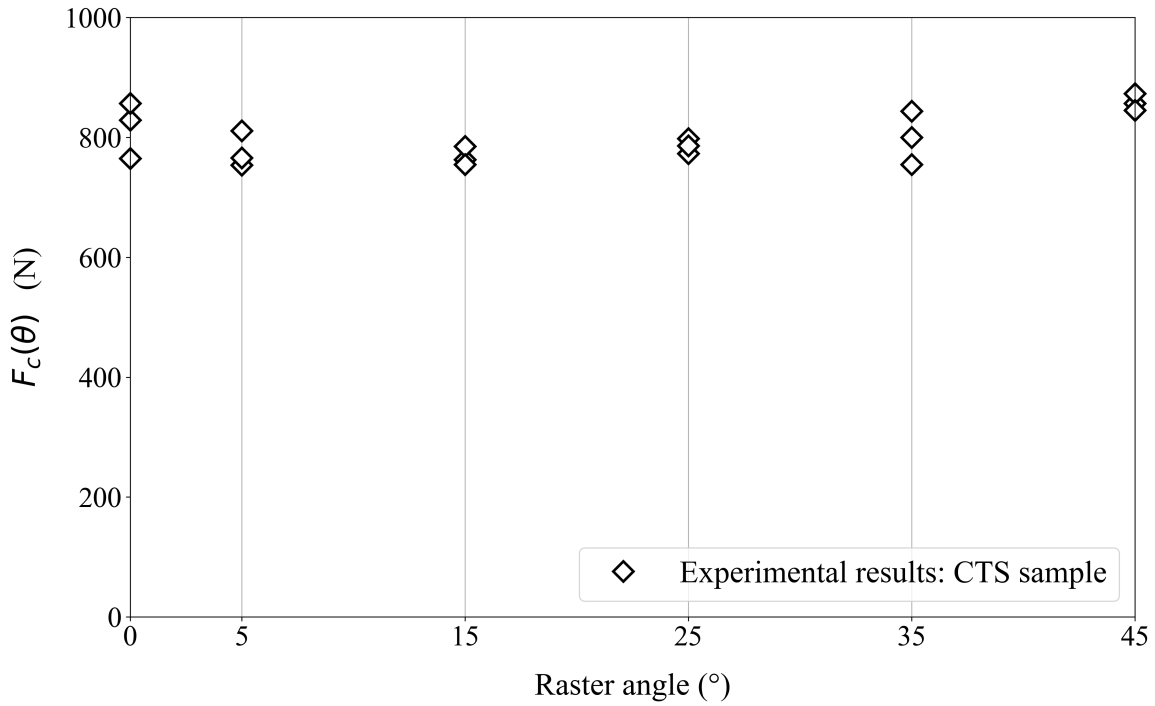

Figure 2.19 Experimental critical load of CTS samples with respect to the raster angle (loading angle = 15°)

Combined with the results for the CT sample, it has been observed that a larger kink angle requires a greater force to redirect the crack propagation.

2.3.4 Fracture energy

Through fracture experiments, the critical energy release rate of the weak plane can be achieved using the following formula under plane stress condition:

$$G_c = \frac{1}{E}\left(\overline{K_I^*}^2 + \overline{K_{II}^*}^2\right) \tag{2.4}$$

where $\overline{K_I^*}$ and $\overline{K_{II}^*}$ are the average value of the SIFs of mode I and mode II after kinking. By substituting the measured K_I^* and K_{II}^* as shown in the example fig. 2.13 and fig. 2.15,we were able to calculate the average critical energy release rate G_c for the weak plane. The calculated value of G_c was approximately 4.25 kJ/m^2, with a standard deviation of 0.97 kJ/m^2. This calculation was based on data obtained from 18 CT samples with different

raster angles and 18 CTS samples with a loading angle of 15°, as illustrated in fig. 2.20. The measured energy release rate of printed PC sample agrees with the value reported by literature from 1 kJ/m^2 to 5 kJ/m^2 (Ashby, 1989; Kim et al., 1994). Due to the fact that crack can only propagate into the direction of "weak plane", the value of G_c along other direction is inaccessible.

It is worth noting that the measured energy release rate differs from the value of 6 kJ/m^2 reported in Corre and Lazarus 2021. In order to understand the reasons behind the discrepancy in energy release rate observed in the same material, we further conducted a comparative analysis of the fracture surfaces using a microscope.

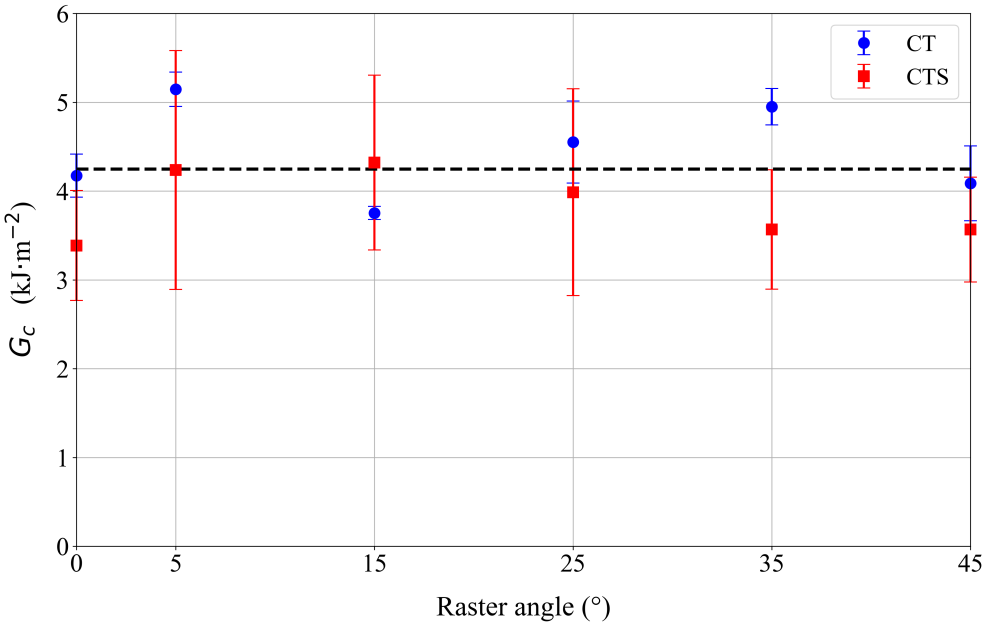

Figure 2.20 Energy release rate measured using 18 CT samples and 18 CTS samples with different raster angle and 15° loading angle

2.3.5 Fracture surface

Figure 2.21 displays the microscopic observations of two CT samples with a 45° raster angle. Sample A was printed using the Raise 3D N2 Plus printer, as utilized in the study by (Corre and Lazarus, 2021), while Sample B was printed using the Raise 3D Pro printer and used in this dissertation. From the front view of these two samples, shown in fig. 2.21 C) and D), it is evident that compared to the sample used in the study by Corre and Lazarus 2021, there are very few plasticized threads observed in our sample. The crack surface appears to be neat, indicating a fracture behavior closer to brittle fracture, with minimal visible signs of plastic deformation occurring in the threads before failure.

Moreover, as reported in the study by Corre and Lazarus 2021, a higher measured value of G_c (6 kJ/m^2) could be attributed to the plastic deformation of the transverse threads. In terms of the crack surface view, the longitudinal and transverse threads are easily distinguishable in the sample used in the study by Corre and Lazarus 2021 due to the gaps between each transverse thread. However, in our sample, it appears that the fusion of the threads from two directions is better, resulting in a less distinguishable boundary between the longitudinal and transverse threads. As a result, fewer instances of plastic deformation were observed in the transverse printing threads.

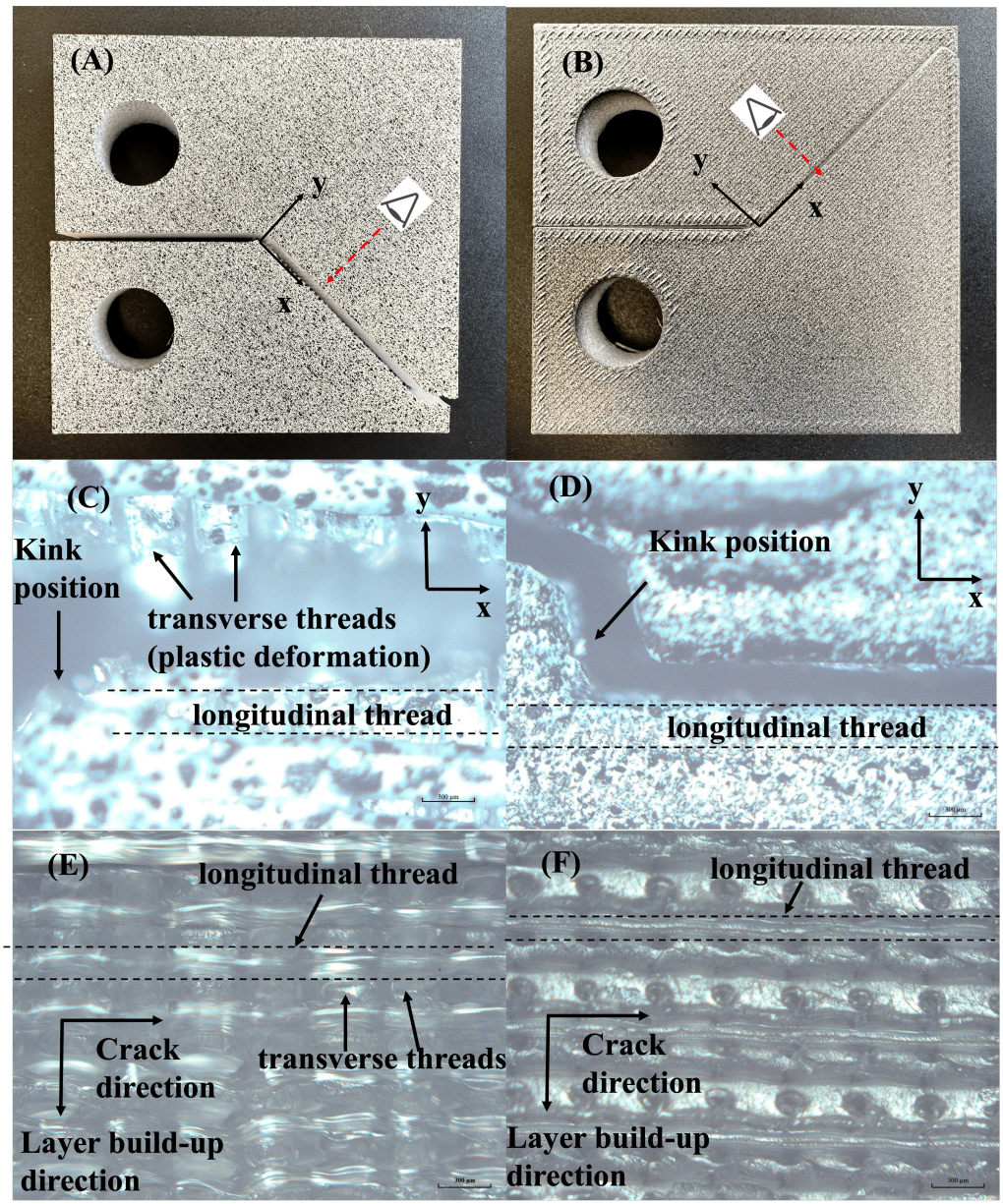

Figure 2.21 Observation under a microscope of two CT samples with a raster angle of 45°: A) sample printed by Raise 3D N2 Plus, as used in the study by (Corre and Lazarus, 2021). B) sample printed by Raise 3D Pro 2, as used in this dissertation. C) and D) show the front view of the respective samples. E) and F) show the view of the crack surface of the respective samples.

Table 2.2 Material properties of printed samples

Material properties			
E (MPa)	ν	σ_c (MPa)	G_c (kJ/m^2)
1890 (std 111)	0.34 (std 0.07)	42 (std 2)	4.25 (std 0.97)

2.4 Conclusions

In this section, we presented the experimental results on specimens with criss-cross printing pattern made using FDM technology. In the tensile test, we determined the material properties of the printed samples, which exhibited nearly isotropic elasticity. However, in the fracture experiments, such printing strategy resulting in a crystalline orthotropic arrangement of the threads and consequently an anisotropic fracture behavior.

By subjecting the specimens to different loading modes (mode I and mode I+II), we observed that cracks only propagated along the printing direction, which can be considered the "weak plane". At a microscopic level, the crack initiation occurred as a result of the rupture of the melting point between two parallel adjacent threads in alternating layers. Meanwhile the crack propagated horizontally across the remaining layers. These experimental observations suggest that directions other than the printing direction can be regarded as "forbidden directions" in comparison to the raster angle.

Interestingly, we found that the critical load was influenced by the crack angle. We discovered that, in the case of the CT sample, the critical force F_c exhibits a consistent increase with respect to the raster angle, whereas for the CTS sample, it follows a non-monotonic trend. Furthermore, through the use of Digital Image Correlation (DIC), we were able to determine G_c along the "weak plane" by using the measured SIFs after crack kinking.

In summary, our experimental findings provide insights into the anisotropic fracture behavior of FDM printed specimens, highlighting the influence of printing direction on crack path selection and its relevant critical load. The measured material properties of printed sample is shown in Table. 2.2. In the next step, our objective is to validate the numerical implementations. These numerical models will be utilized to investigate the anisotropic fracture behavior, as described in chapter 4.

Chapter 3

Validation of numerical models

This chapter focuses on validating the implementation of the FEM models based on both the classic and variational approaches. In the classic model, a static elasticity problem with a fixed geometry is solved to determine the SIFs in the presence of a crack kink. These SIFs will be used later to validate experimental measurements obtained through DIC. To ensure accurate determination of the SIFs in the presence of a kink, we compare the numerical results with the Amestoy-Leblond's formula. Furthermore, the implementation of the I-integral is validated using data from the existing literature.

In the phase-field model based on the variational approach, our goal is to verify the implementation of the model with both isotropic and weak anisotropic surface energy. To accomplish this, we compare the predictions of the phase-field model with experimental data from relevant literature. In the case of the isotropic model, we focus on crack propagation under mixed-mode loading conditions using Centred Notched (CN) specimens (Erdogan and Sih, 1963). This investigation allows us to assess the phase-field model's capability to predict crack paths and the corresponding critical forces. Additionally, we validate the implementation of the two-fold symmetric model for the weak anisotropic case. This is achieved by comparing the predicted crack paths with experimental results obtained from composite materials Mesgarnejad et al. (2020). For both studies, we employ the AT1 damage model, and the selection of the regularization parameter for the second-order phase-field model is thoroughly discussed.

Contents

3.1 Static elasticity problem: classic approach

To model a kinked crack path, a full-sized CT sample was meshed with Gmsh (a finite-element mesh generator). This was done to circumvent penitential mesh-related issues that could arise when employing a fine mesh in the vicinity of the crack tip, as the solution near the crack tip has to be resolved with adequate accuracy with an extreme fine discretization. The mesh of the CT sample with a kink angle of 25° in Gmsh is shown in Fig. 3.1, where (A) depicts the entire CT sample mesh consisting of second-order Triangle elements (blue) and second-order Quadrilateral elements (red), while (B) represents the mesh near the crack tip.

Note that nodes in the vicinity of the crack tip were encompassed within a circular region consisting of identical quadrilateral elements. This design enabled the application of the $G-\theta$ method to determine the SIFs. The circular region surrounding the crack tip was made up of structured meshes with multiple layers, as shown in Fig. 3.1 (B). The radius R_1 of this circular region was determined based on the kink length s to ensure that the entire kink was not included in the layer where the $G-\theta$ method was applied.

The finite element analyses were performed using the open-source Cast3M software. The calculations involved the solution of a linear elastic boundary value problem with a fixed crack tip. The outputs consist of the displacement field $\boldsymbol{u}$, strain field $\underset{\sim}{\boldsymbol{\varepsilon}}$, and stress field $\underset{\sim}{\boldsymbol{\sigma}}$.

The CT specimen was loaded through the bolt in the pin hole during fracture experiment, an accepted method of modeling this contact problem is to fill the pin holes with the Q4 elements (Ortega et al., 2014). The same material properties as the CT sample were assigned to both bolts, we applied a y-direction displacement to the pivot of upper bolt, the pivot of lower bolt being fixed. We adopted this method to validate the the SIFs across a crack kink.

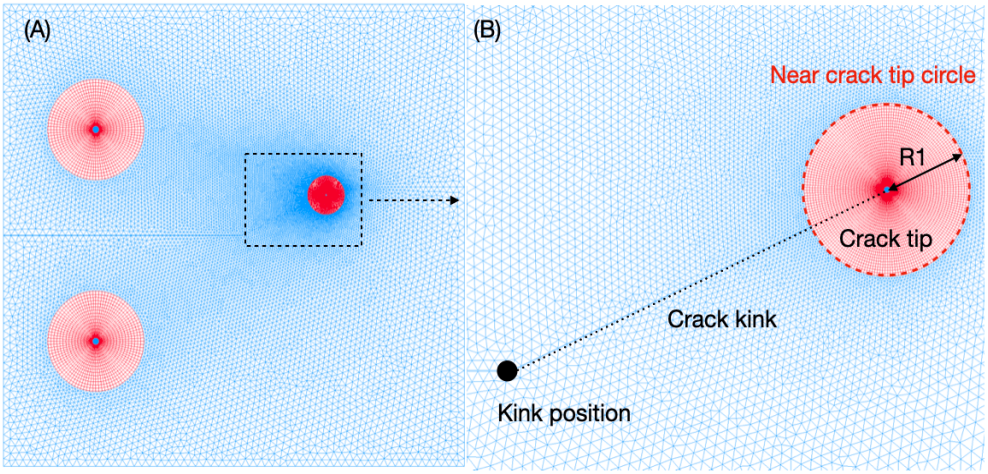

Figure 3.1 Mesh generated by Gmsh, CT sample with a kink angle of 25°. (A) shows the mesh of the entire CT sample with 50000 elements, where the blue and red mesh represent the Tri6 elements and Qua8 elements respectively. (B) is a zoomed-in view of the kink region, which consists of 6000 elements in the near crack tip circle. The near crack tip circle has 30 layers, and the kink length is dimensionless with a value of $\frac{s}{L} = 0.06$

3.1.1 SIFs across a kink: comparison to Amestoy-Leblond's formula

Before conducting the numerical experiments, we conducted validation tests for numerical convergence concerning the number of elements used and the number of layers where the $G-\theta$ method is applied. The results of the convergence analysis, both for CT samples with and without crack kink, indicated that convergence was achieved when employing 20,000 elements. For the $G-\theta$ method, the number of layers where it should be applied was determined as shown in fig. 1.6. Consequently, we conducted numerical experiments by selecting a total number of layers near the crack tip close to 30 and varying the number of layers where the $G-\theta$ method was applied. Fig. 3.2 displays the dimensionless values of the SIFs as a function of the number of layers where the $G-\theta$ method is employed. Notably, once $n > 5$, convergence was achieved using quadratic elements.

To validate our model, we will compute the universal functions $F_{pq}(\varphi)$ and $G_p(\varphi)$ numerically and compare them with their corresponding theoretical values. This comparison will serve as a means to evaluate the accuracy and reliability of our model.

We encountered a challenge in determining the values of $K_p^*(\varphi)$ as s approaches 0 for computing the functions $F_{pq}(\varphi)$ and $G_p(\varphi)$ due to the inaccessibility of performing numerical calculations with a kink length of 0. To address this limitation, we employed a fitting approach. We fitted the numerical evolution curve of $K_p(s,\varphi)$, which represents

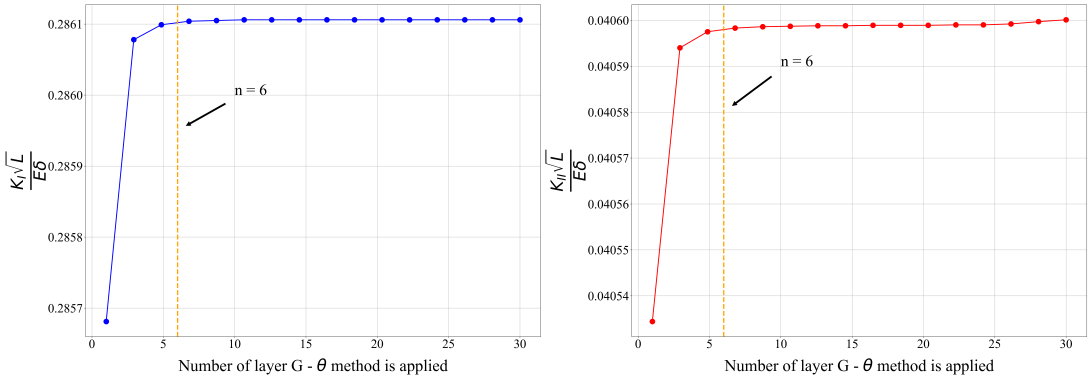

Figure 3.2 Dimensionless value of Stress intensity factor (left K_I and right K_{II}) with respect to the number of layer where G-θ method is applied (total layer $n = 30$, kink length $s/L = 0.06$)

the variation of K_p with respect to the kink length s and the kink angle φ, using a known functional form (3.1), inspired by eq. (1.10). By employing this fitting procedure, we were able to approximate the values of the universal functions $F_{pq}(\varphi)$ and $G_p(\varphi)$ as s approaches 0.

$$K_p(s,\varphi) = A_p(\varphi) + B_p(\varphi)\sqrt{s} + C_p(\varphi)s + D_p(\varphi)s^{3/2} \tag{3.1}$$

The numerical values of the SIFs used in the fitting procedure were obtained by applying a constant load and solving the elasticity problem for different combinations of kink length s and kink angle φ. The kink angle φ was varied in the range of $[0°, 80°]$. Finally, using the coefficients obtained from the fitting procedure, the values of $F_{pq}(\varphi)$ and $G_p(\varphi)$ can be calculated using:

$$A_p(\varphi) = F_{pq}(\varphi)K_q \ , \ B_p(\varphi) = G_p(\varphi)T \tag{3.2}$$

here, $A_p(\varphi)$ and $B_p(\varphi)$ represent the coefficients obtained from fitting the numerical SIFs: $K_p(s,\varphi)$. Specifically, for the case of mode I loading condition, the expression can be simplified as follows:

$$F_{pI}(\varphi) = \frac{A_p(\varphi)}{K_I} \ , \ G_p(\varphi) = \frac{B_p(\varphi)}{T} \tag{3.3}$$

Figure. 3.3 illustrates the fitted curves for various kink angles, where the black dots represent the dimensionless numerical values of $\frac{K_I(s,\varphi)\sqrt{L}}{E\delta}$ corresponding to different kink lengths s with a unit displacement imposed on the bolt. For the fitting procedure, 24 values in the dimensionless range $\frac{s}{L}$ $[0.001, 0.1]$ were utilized. The figure also displays the fitted curves along with the corresponding coefficients obtained from the fitting process.

The coefficients are arranged in the order $[A_p(\varphi), B_p(\varphi), C_p(\varphi), D_p(\varphi)]$ as specified in eq. (3.1). Furthermore, the dimensionless values of $\frac{K_I\sqrt{L}}{E\delta}$ and $\frac{TL}{E\delta}$ before kinking occur are 0.339 and 0.177, respectively.

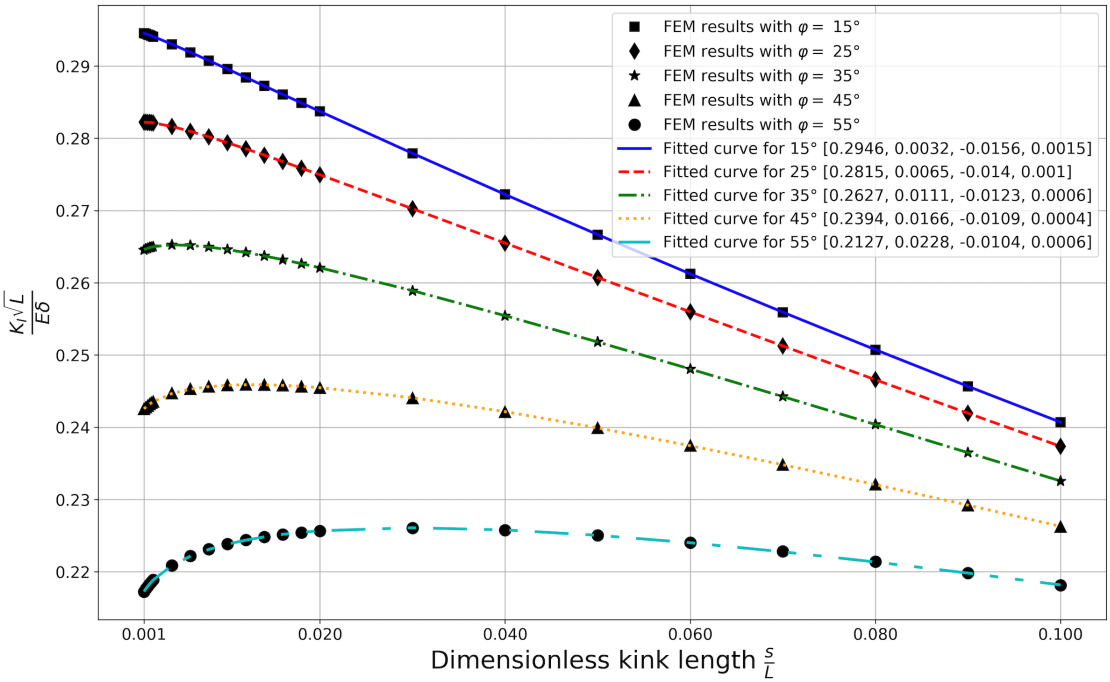

Figure 3.3 Fitted curve for $\frac{K_I(s,\varphi)\sqrt{L}}{E\delta}$ with various kink angles: the black dots are the numerical results. The fitted curves are represented by lines, the fits coefficients are shown in the legend, corresponds in turn to $[A_p(\varphi), B_p(\varphi), C_p(\varphi), D_p(\varphi)]$ in expression (3.1)

In this study, we aim to determine the appropriate range of dimensionless kink length $[\frac{s_{min}}{L}, \frac{s_{max}}{L}]$ to be used in the fitting process using the 4 terms expansion of $K_p(s,\varphi)$ as presented in eq. (3.1). To achieve this, we present a comparison between the numerical and theoretical values of $F_{pq}(\varphi)$ and $G_p(\varphi)$ in fig. 3.4 and fig. 3.5 (corresponding to varying $\frac{s_{max}}{L}$ and $\frac{s_{min}}{L}$, respectively). Each sub-figure is divided into left and right rows, representing the functions $F_{pq}(\varphi)$ and $G_p(\varphi)$, respectively. The sub-figures are arranged from top to bottom, with each one indicating the range of kink length used for the fitting procedure.

Since $F_{pq}(\varphi)$ and $G_p(\varphi)$ are results obtained as $s \to 0$, it is essential to choose a range of kink length that is as close to 0 as possible in order to ensure the accuracy of the results. Therefore, the selection of an appropriate range of kink length is critical for obtaining reliable fitting outcomes.

In summary, the results indicate that by varying $\frac{s_{max}}{L}$ within the range of [0.1, 0.4] (with $\frac{s_{min}}{L}$ fixed at 0.0002), or $\frac{s_{min}}{L}$ within the range of [0.0002, 0.04] (with $\frac{s_{max}}{L}$ fixed at 0.1),

the values of $F_{pq}(\varphi)$ consistently remain acceptable when compared to the theoretical values. However, to obtain reasonable numerical values for $G_p(\varphi)$, it is recommended to set the dimensionless kink range to [0.001, 0.1]. This range is illustrated in the second row of fig. 3.5.

By employing the fitting process with the numerical values within the dimensionless kink length range of [0.001, 0.1], we have achieved excellent agreement between the numerical values of $F_{pq}(\varphi)$ and $G_p(\varphi)$ and their corresponding theoretical values. This indicates that our model accurately predicts the relationship between the stress intensity factors (SIFs) as expressed in eq. (1.10), both before and after kinking, within the specified range. Consequently, our model can effectively analyze with a kinked crack path, as presented in the study by Corre and Lazarus 2021. Considering the length of our CT sample: $L = 50$ mm, it can be inferred that the expression $F_{pq}(\varphi)K_q + T\sqrt{s}G_p(\varphi)$ provides a satisfactory approximation of $K_p(s, \varphi)$ within the range of [0.5, 5] mm. Notably, this range is within the limits of observation in the experimental setup.

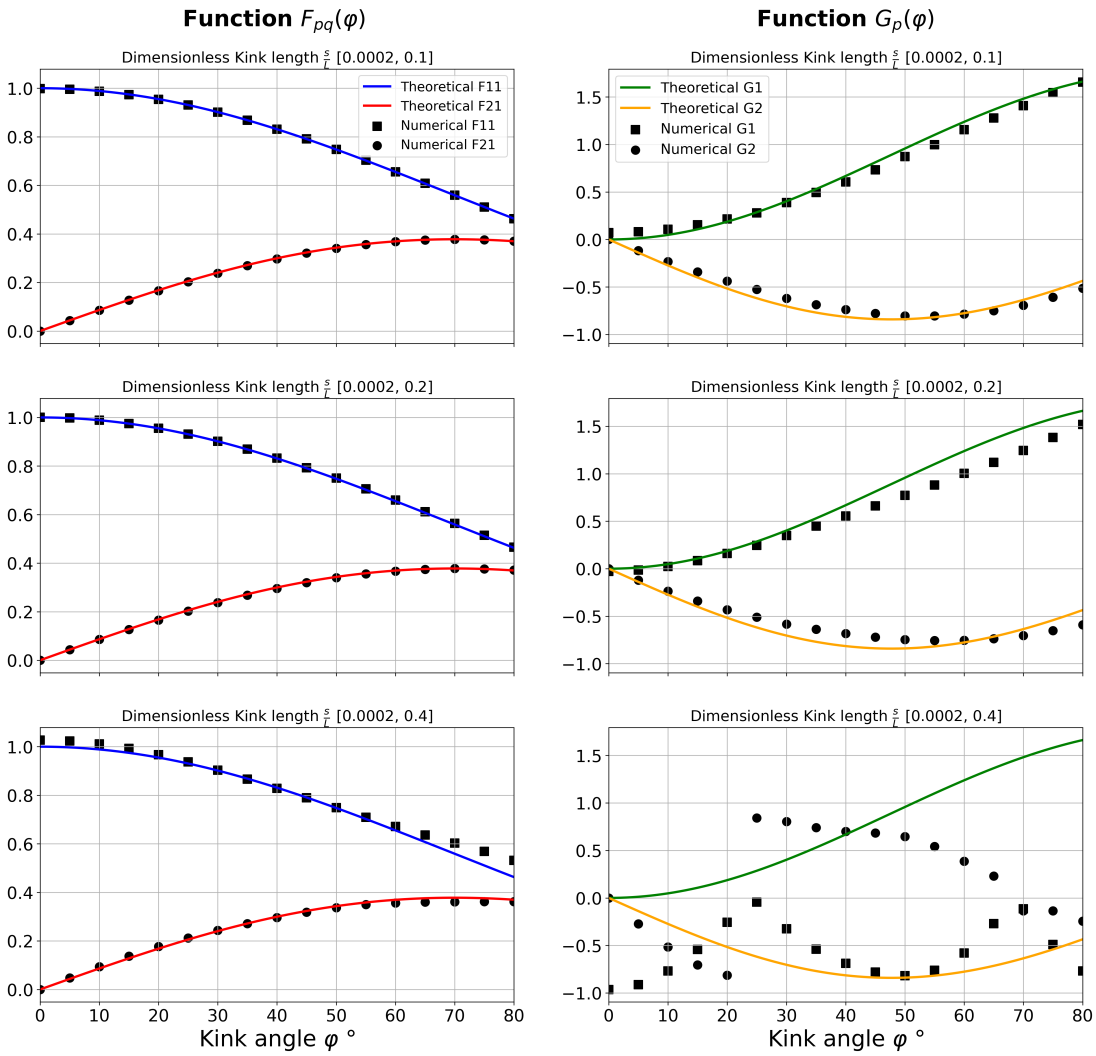

Figure 3.4 Function $F_{pq}(\varphi)$ and $G_p(\varphi)$ between numerical and theoretical values for different range of the kink length with change of $\frac{s_{max}}{L}$

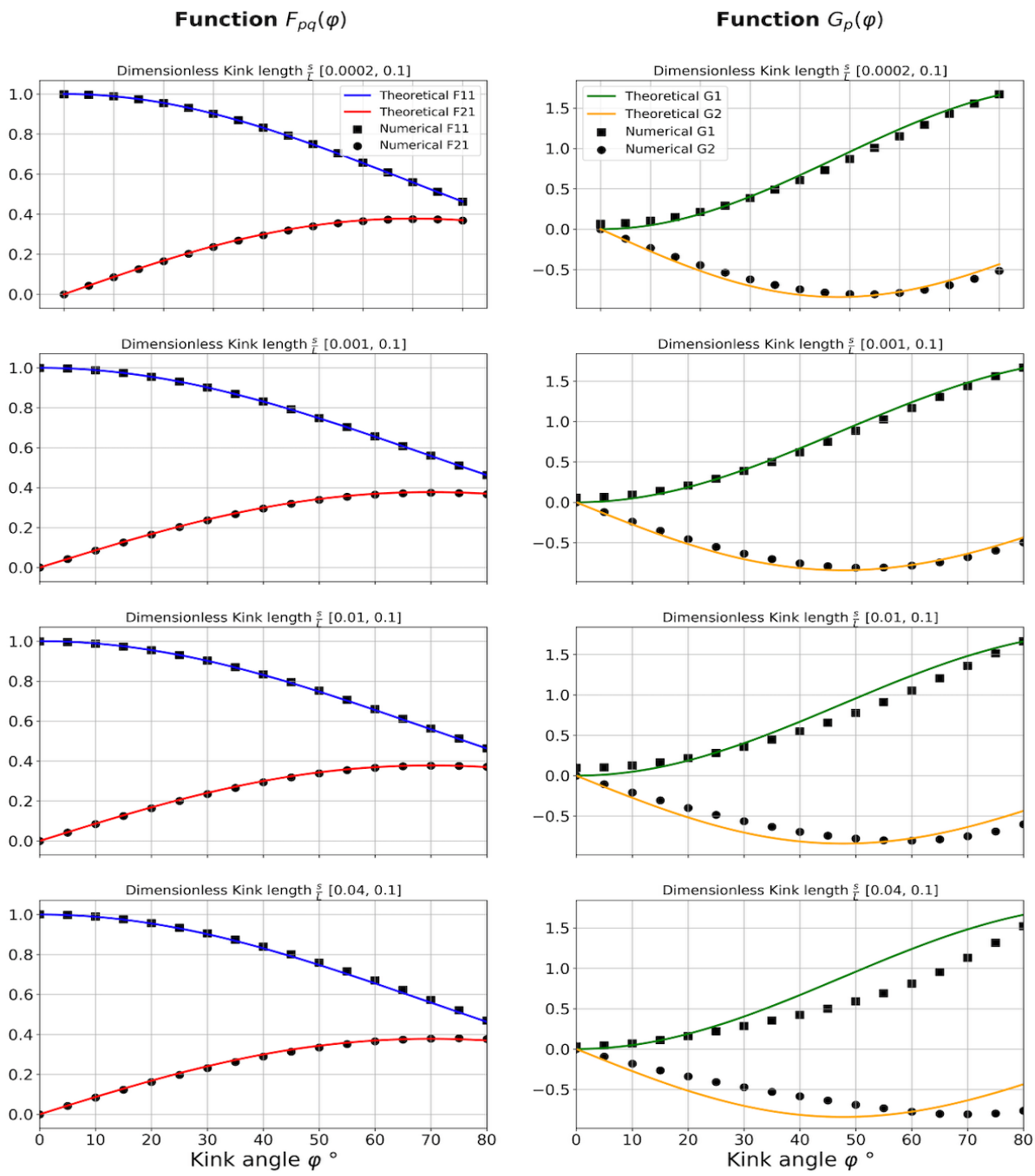

Figure 3.5 Function $F_{pq}(\varphi)$ and $G_p(\varphi)$ between numerical and theoretical values for different range of the kink length with change of $\frac{s_{min}}{L}$

3.1.2 Validation of I-integral implementation

The phase-field model was implemented in the open-source computational platform FEniCS. However, to determine the fracture parameters, an additional numerical method

needed to be implemented. Therefore, we adopted the I-integral method because it allows us to determine both the SIFs (Yau et al., 1980) and the higher-order term, namely the T-stress, by choosing the appropriate auxiliary field (Kfouri, 1986). The choice of auxiliary field is presented in Section 1.4.1.2.

In practical numerical simulations, the mutual energy momentum tensor can be extracted using FEniCS and post-processed using an open-source visualization platform called ParaView (ParaView, 2023). To verify the implementation of the I-integral method in FEniCS, we utilized the Single Edge Notch (SEN) specimen as an illustrative example, as shown in fig. 3.6.

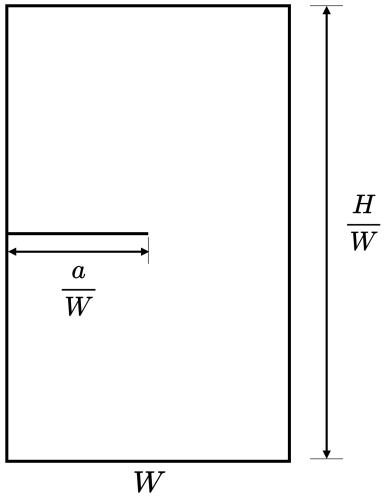

Figure 3.6 Single Edge Notch specimen

To evaluate the effectiveness of the I-integral method in separating the SIFs, we applied a mixed load to the SEN specimen. Specifically, we applied a unit stress on the upper boundary in both the x and y directions, while keeping the lower boundary fixed. By sequentially varying the ratios $\frac{a}{W}$ and $\frac{H}{W}$, we obtained the SIFs K_I and K_{II} using the I-integral method in FEniCS. We then compared these results to those obtained using the $G-\theta$ method in Cast3M.

The comparison results are presented in fig. 3.7. It is evident that the SIFs obtained through the I-integral method exhibit strong agreement with those obtained using the $G-\theta$ method. This validation confirms the capability of the I-integral method in accurately separating the SIFs under mixed mode loading conditions.

To examine the higher-order term T-stress, we applied mode I loading to the SEN specimen with a unit stress in the y direction. The comparison of the dimensionless T-stress ($\frac{T\sqrt{\pi a}}{K_I}$) in terms of the B-ratio is presented in fig. 3.8. The B-ratio, calculated using the I-integral method, shows excellent agreement with the value reported in the

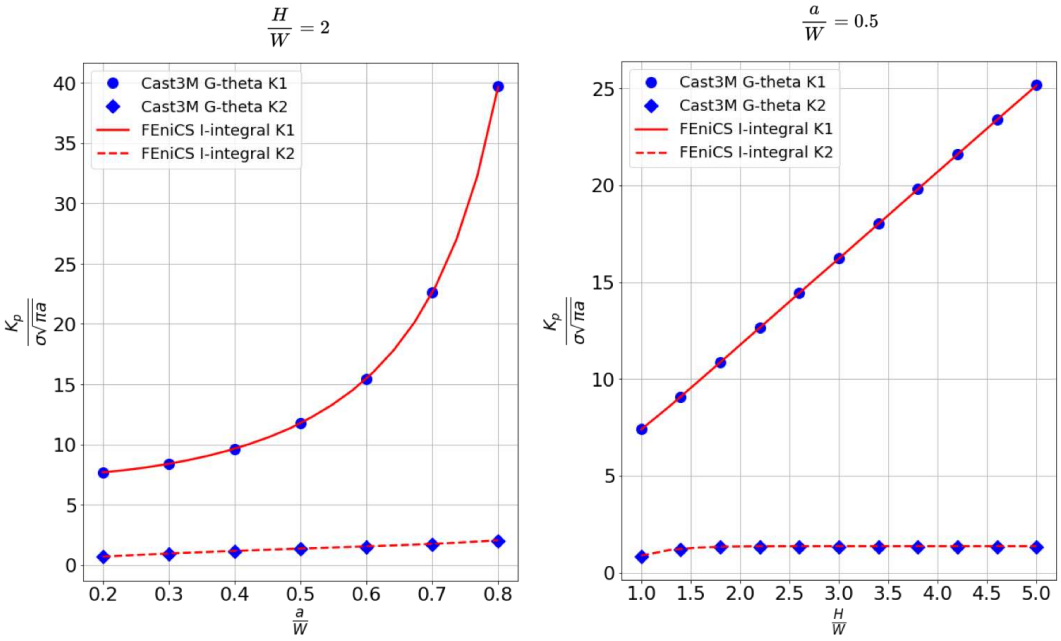

Figure 3.7 The comparison of SIFs between Cast3M and FEniCS for SEN sample is illustrated. On the left side, the dimensionless SIFs are shown for different values of $\frac{a}{W}$, where $\frac{H}{W} = 2$. On the right side, the dimensionless SIFs are shown for different values of $\frac{H}{W}$, where $\frac{a}{W} = 0.5$.

literature (Leevers and Radon, 1982). The literature provides B-ratio values for various sample geometries with different dimensional configurations, all obtained through a numerical model.

However, it is worth noting that the T-stress value extracted using the direct method of phase subtraction from the stress field near the crack tip is found to be inaccurate in certain cases. Consequently, the implementation of the I-integral method in FEniCS is validated based on the comparison results obtained using the SEN specimen.

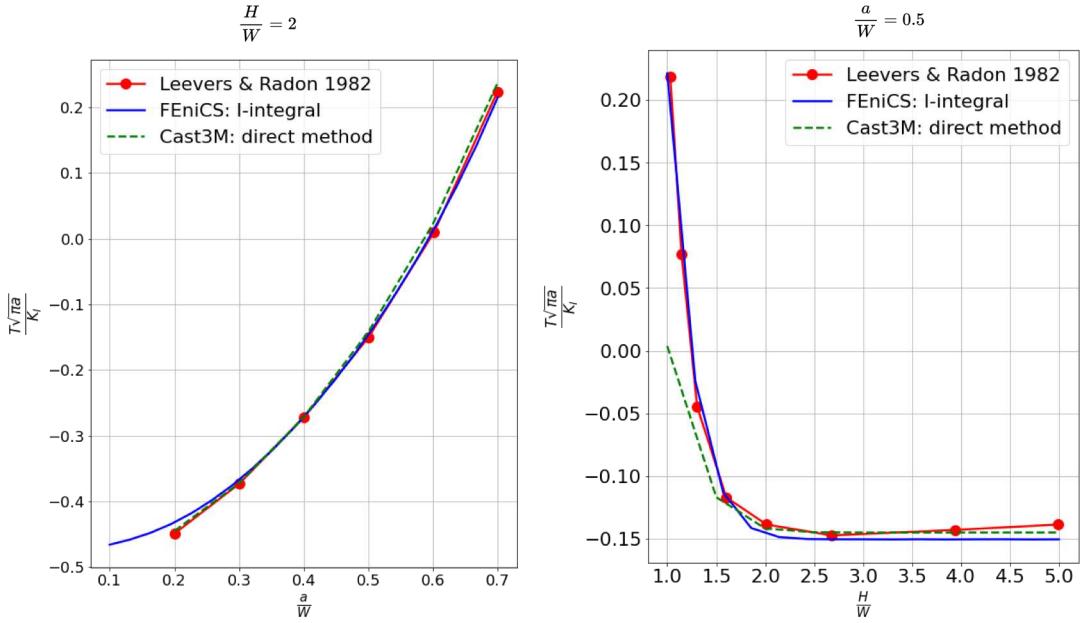

Figure 3.8 The comparison of T-stress values among Cast3M, FEniCS, and a reference value from Leevers and Radon 1982 for the SEN sample is presented. On the left side, the various B-ratios are plotted against $\frac{a}{W}$ with a fixed $\frac{H}{W} = 2$. On the right side, the different B-ratios are plotted against $\frac{H}{W}$ with a fixed $\frac{a}{W} = 0.5$.

3.2 Phase-field modeling of brittle fracture

The validation process of the phase-field model implementation begins with a simple model, specifically the second-order model featuring isotropic and weakly anisotropic surface energy. Initially, we addressed the mixed-mode fracture problem described by Erdogan and Sih 1963, assuming isotropic fracture toughness. To validate the numerical predictions concerning the crack path and the relevant critical stress, we compared them with both the experimental data from Erdogan and Sih 1963 and theoretical results based on the energy release rate criterion. Subsequently, using the two-fold anisotropic model, our objective was to replicate the numerical findings presented in the study conducted by Mesgarnejad et al. 2020, while comparing them with their experimental results on a composite material. The numerical implementation was performed using the FEniCS software (FEniCS, 2022). Our primary focus was on the AT1 damage model as presented in eq. (1.36), as it is similar to the specific damage model employed in the higher-order model ($w(\alpha) = 9\alpha$) (Li and Maurini, 2019). Validating the AT1 phase-field model allows for a smooth transition as we expand our investigations to the higher-order phase-field model, aiming to analyze crack propagation in 3D printed samples.

3.2.1 Isotropic case: PMMA specimen under mixed loading

Figure. 3.9 illustrates the dimensions of the center-notched specimens used in the study by Erdogan and Sih 1963. It is noticed that the in the study of Erdogan and Sih 1963, the imperial system was used, here all the units used in their paper have been converted to the metric system. These specimens were composed of an isotropic homogeneous PMMA (Polymethyl Methacrylate) plate with an inclined center-notch. The length of the notch was denoted as $2a$, and it was positioned at a notch angle of β.

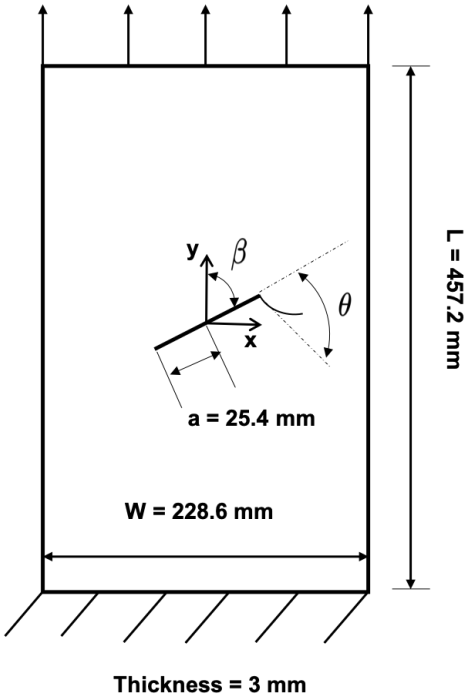

Figure 3.9 Dimension of center-notched sample in Erdogan and Sih 1963

To conduct the numerical calculations, we utilized an AT1 phase-field model with isotropic surface energy as introduced in Section 1.4.2, which has proven effective in predicting complex crack trajectories and stress states during the crack nucleation phase (Cavuoto et al., 2022). Several numerical parameters were necessary for the numerical experiments, including Young's modulus E, Poisson's ratio ν, fracture energy G_c, and the regularization parameter ℓ.

The values of the elastic constants were chosen as $E = 3000$ MPa and $\nu = 0.35$, as referenced from Pham et al. 2017 (they were not provided in Erdogan and Sih 1963). The fracture energy G_c was set to 0.35 kJ/m^2, as reported in Erdogan and Sih 1963. The regularization parameter ℓ for AT1 phase-field model has been computed using the following expression (Tanné et al., 2018):

$$\ell = \frac{3}{8}\frac{G_c E}{\sigma_c^2} \tag{3.4}$$

It is important to note that this formulation assumes that the material is isotropic and homogeneous under uni-axial tension (Pham et al., 2011). For the case of CN specimen, the local stress state changes due to the presence of an inclined notch. However, in the study of Cavuoto et al. 2022, they determined the optimal value of ℓ by fitting their numerically predicted load-displacement curves with experimental results obtained from compact tension tests. Interestingly, they found that the computed value of ℓ using the previous formulation was very close to the value obtained by fitting the numerical results with experimental data. Hence, we adopted this formula to estimate the value of the regularization parameter ℓ in our numerical experiments. The regularization parameter $\ell = 0.25$ mm was obtained by using the material strength $\sigma_c = 40$ MPa. To enhance numerical efficiency and mesh generation, we used a slightly larger value of $\ell = 0.3$ mm and set the mesh size to $h = \ell/3$ near the crack tip while the mesh size at the boundary was 12 times larger. The upper boundary of the specimen in the y-axis was subjected to a displacement, while the lower boundary remained fixed. In addition, we assigned the damage variable $\alpha = 1$ at the crack tip as the initial condition for the damage field. The numerical computations were performed assuming 2D plane stress.

Before conducting the numerical experiments, we compared the SIFs obtained using the I-integral method with the analytical solution given by eq. (3.5), which corresponds to the scenario where a crack is situated in an infinite plate. These numerical values will be used subsequently to establish the relationship between the critical stress and the initial crack angle using the $G_{\max}$ criteria. Fig. 3.10 shows the normalized values of K_I and K_{II} for different crack angles β ranging from 20° to 90°, comparing the analytical solution with the numerical results. It is worth noting that the numerical results demonstrate excellent agreement with the analytical solution.

$$K_{\mathrm{I}} = \sigma\sqrt{\pi a}\sin^2\beta, \quad K_{\mathrm{II}} = \sigma\sqrt{\pi a}\sin\beta\cos\beta \tag{3.5}$$

Figure. 3.11 left presents a snapshot of the numerical predicted crack path (highlighted in red) for a CN sample with an initial crack angle of $\beta = 60°$. And Figure. 3.11 right presents the numerical load curve for CN sample with β=60°. In fig. 3.13, the kink angle relative to the initial crack angle is depicted, and the theoretical prediction for $G_{\max}$ is determined using Eq. (1.19) with an isotropic surface energy. The AT1 phase-field model accurately predicts the angle of the crack path, as evidenced by the comparison with experimental and theoretical data. Fig. 3.14 compares the numerical prediction of

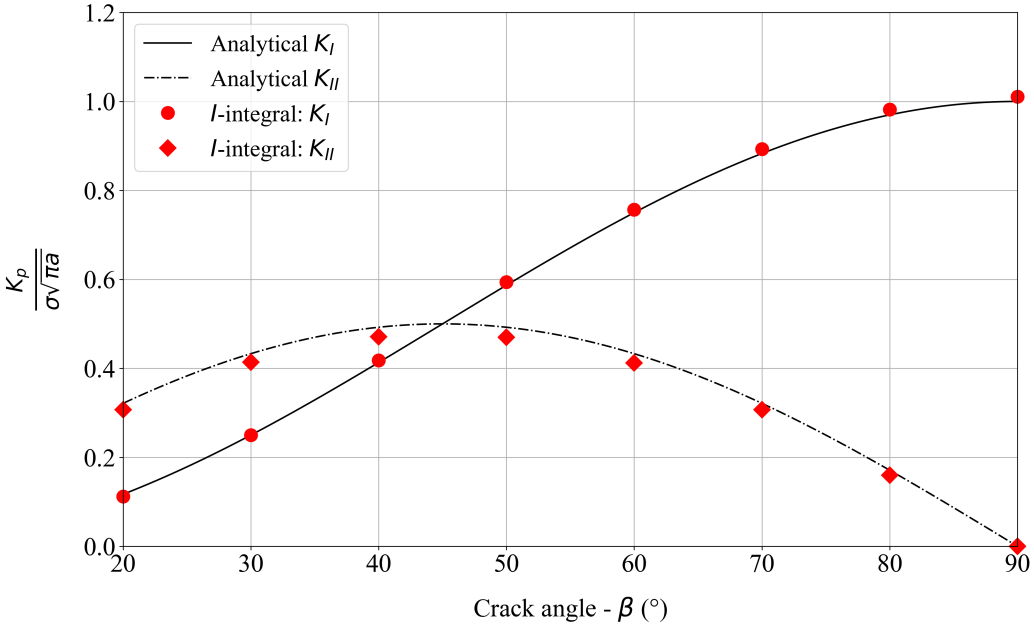

Figure 3.10 Normalized SIFs of center notched sample (a/W=0.11)

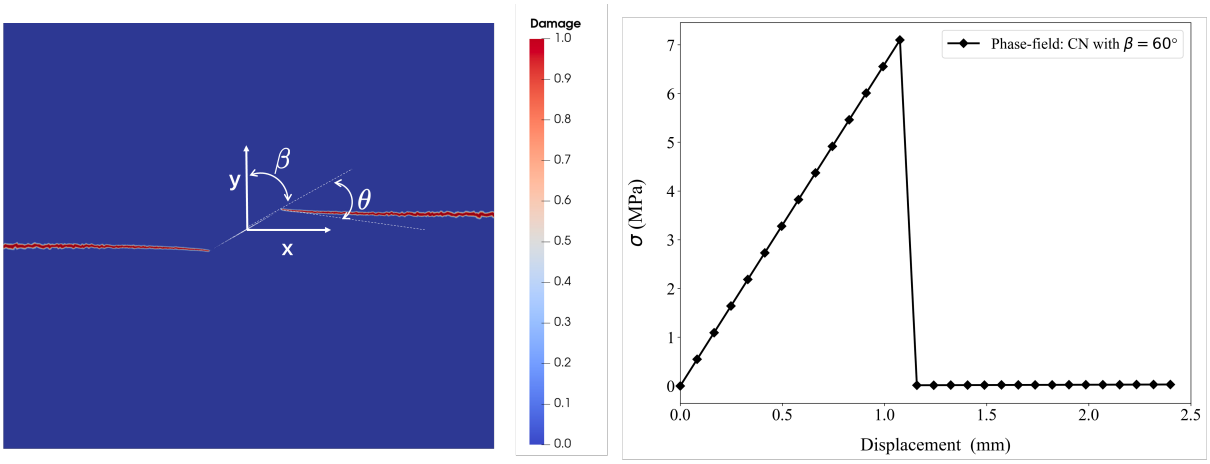

Figure 3.11 Left: a snapshot of numerical predicted crack path (in red, zoom on center crack, ℓ=0.3 mm) and right: numerical load curve (30 time step) for center-notched sample with the initial crack angle $\beta = 60°$.

the critical stress with experimental and theoretical results, the numerical critical stress σ_c corresponds to the maximum stress shown in figure. 3.11(right). The experimental critical stress values were implicitly presented in the study by Erdogan and Sih 1963, and we have re-plotted them in Figure 3.12. Each data point in the figure corresponds to a specific test with a particular crack angle β. In order to obtain the relevant critical stress values, we substituted the corresponding crack angle β and the value of SIFs into into the analytical solution given by eq. (3.5). By doing so, we were able to calculate the corresponding critical stress for each crack angle β.

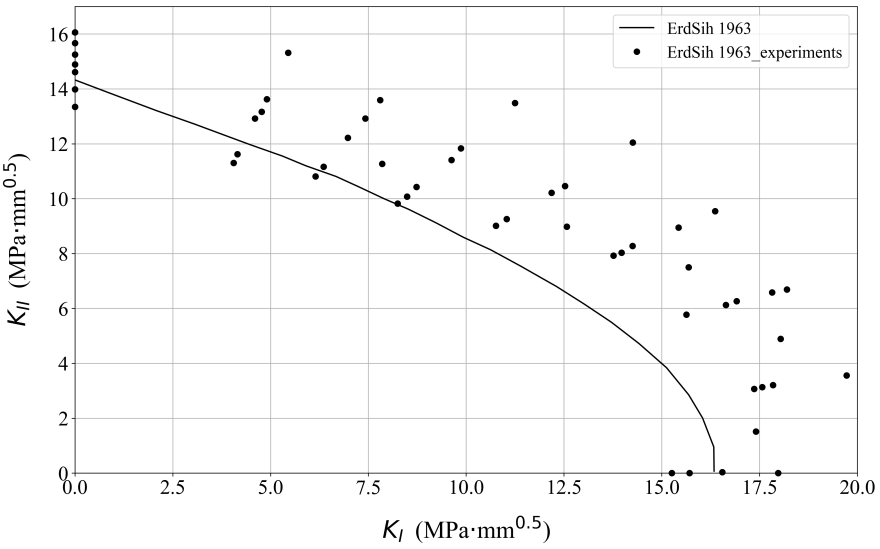

Figure 3.12 Re-plotted figure.6 in Erdogan and Sih 1963: K_I versus K_{II} at the beginning of crack propagation in CN samples

To obtain the relevant stress in the LEFM framework, we adopted the $G_{\max}$ criteria. The $G_{\max}$ predictions are derived by using eq. (1.13) to develop $G(\theta) = G_c$:

$$a\sigma_c^2 \frac{1}{E}\left[\left(\hat{K}_I^*(\theta)\right)^2 + \left(\hat{K}_{II}^*(\theta)\right)^2\right] = G_c \tag{3.6}$$

where $\hat{K}_I^*(\theta)$ and $\hat{K}_{II}^*(\theta)$ are the SIFs after kinking at unit stress $\sigma = 1$ and unit initial crack length $a = 1$. Then we substitute $\hat{K}_p^*(\theta)$ by using eq. (1.12), we can establish the relationship between the fracture angle θ and the critical stress as follows:

$$\frac{a\sigma_c^2}{K_c^2} = \frac{1}{[F_{1q}(\theta)\hat{K}_q]^2 + [F_{2q}(\theta)\hat{K}_q]^2} \tag{3.7}$$

where a is half of the notch length, K_c is the fracture toughness of the material. $F_{1q}(\theta)$

and $F_{2q}(\theta)$ are universal functions and known for different values of kink angle θ refer to Appendix. A. The numerical values of $\hat{K}_q$ at unit stress and unit notch length, as presented in fig. 3.10, are then substituted into eq. (3.7). Consequently, the relationship between the critical stress σ_c and the initial crack angle β, obtained using the energy release rate criterion, is represented by the black curve in fig. 3.14.

A comparison of these results reveals the effectiveness of the AT1 isotropic phase-field model in accurately predicting numerical outcomes for mixed mode fracture problems. Additionally, we have demonstrated that these predictions can also be obtained through the application of the $G_{\max}$ within the framework of LEFM.

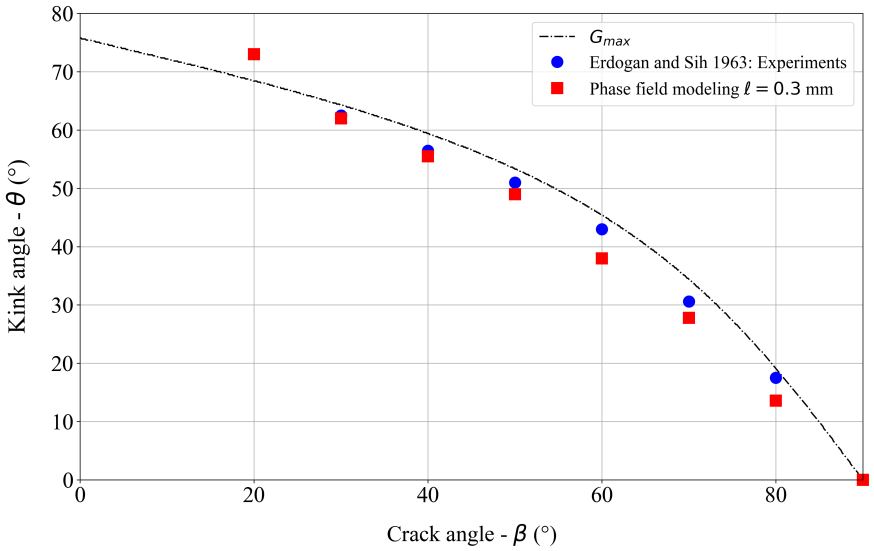

Figure 3.13 Comparison of experimental, (Erdogan and Sih, 1963) theoretical and simulated kink angle with respect to the initial crack angle. The black curve represent the predicted results using the maximum stress criterion, while dot-curve is obtained by the G_{max} criterion. Blue dots are experimental results from Erdogan and Sih 1963, and red dots represents the numerical prediction.

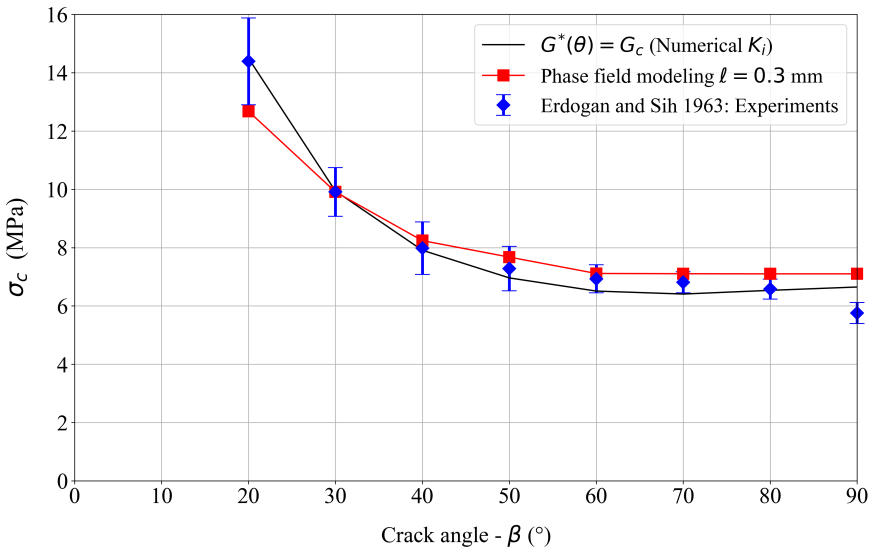

Figure 3.14 Comparison of experimental, theoretical and simulated critical stress with respect to the initial crack angle. Blue dots represent the experimental results from Erdogan and Sih 1963, the red dots are the numerical prediction, and black curve shows theoretical prediction base on the energy release rate criterion.

3.2.2 Weakly anisotropic case: Composite materials

Fig. 3.15 provides an illustration of the dimensions of the long and short samples utilized in the study conducted by Mesgarnejad et al. 2020. These samples were composed of a composite material comprising a polymer matrix with alumina platelets oriented along α_Γ. Fracture experiments were carried out on these orientationally ordered composites, revealing that the crack path can vary as the volume fraction increases. This variation in crack path is attributed to the presence of weakly anisotropic fracture toughness within the material. It is important to note that the selection of the crack path is influenced by both macroscopic factors, such as sample geometry, and microscopic factors, including volume fraction and orientation of the fiber within the matrix.

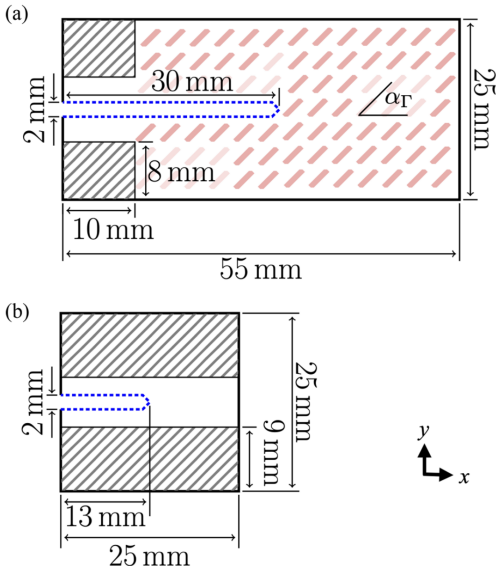

Figure 3.15 Dimension of composite material (Mesgarnejad et al., 2020) with alumina fiber oriented along α_Γ: a) Long sample and b) Short sample, with gray hatched regions were affixed onto grips

Our primary objective is to validate the implementation of the phase-field model with a weakly anisotropic (two-fold symmetric) surface energy, as presented in Section 1.4.3.1. To achieve this, we aim to replicate the numerical predictions and then compare them with the experimental results provided in (Mesgarnejad et al., 2020). In this study, we have chosen to use the AT1 model instead of the KKL damage model as in Mesgarnejad et al. 2020 (presented in eq. (1.36).

To determine the value of the regularization parameter ℓ for the AT1 model, we have utilized an estimated value that is equivalent to that of the KKL model. The estimated value of ℓ is calculated as $0.375 \cdot \frac{G_c E}{\sigma_c^2}$. The only difference between the AT1 and KKL models lies in the initiation of crack nucleation. In the KKL model, a slight perturbation at the notch is required, where the damage variable (α) is set to a non-zero value, in order to initiate crack nucleation. Otherwise, the damage variable will always remains at zero. In the case of the AT1 model, it does not necessitate an initial damage condition for nucleation. Furthermore, since we are not seeking to obtain a numerical prediction of the critical load, we have therefore omitted the initial damage condition $\alpha = 1$. Using the material parameters provided in (Mesgarnejad et al., 2020), we estimated the range of the regularization parameter to be between $225\,\mu$m and $550\,\mu$m. To conduct numerical experiments, we used the given material properties and explored the effects of both the upper and lower bounds of the estimated regularization parameter.

We initially focused on investigating a specific case where the material axis was fixed

at $\theta_0 = 90°$, corresponding to a fiber orientation of $\alpha_\Gamma = 90°$ in the experimental setup. In Fig. 3.16, we present a comprehensive comparison of the experimental, theoretical, and numerical results for the predicted crack angle as a function of the anisotropic coefficient A_t. Here, the anisotropic coefficient A_t represents the volume fraction of the fibers in the matrix, and its relationship with the numerical parameter A_t is established based on the experimental data provided in detail in (Mesgarnejad et al., 2020). By varying A_t and observing its influence on the predicted crack angle, we aim to gain insights into the impact of the anisotropic coefficient on the crack path selection.

In the presence of weakly anisotropic surface energy, the GMERR criterion (presented in Section 1.3.1: Eq. (1.19)) undergoes a modification by replacing $G_c(\theta)$ with the corresponding surface energy form provided in eq. (1.41). In fig. 3.16, the black dashed line represents the GMERR prediction without considering the T-stress, which is not satisfactory. Therefore, to enable a more accurate quantitative prediction of the crack path using the GMERR criterion, we adopt the approach described in (Mesgarnejad et al., 2020), where we choose $s = \ell$ to account for the T-stress effect when calculating the energy release rate at the tip of a kinked crack:

$$\begin{aligned} K_I^*(\theta) &= K_I F_{11}(\theta) + T\sqrt{s} G_1(\theta) \\ K_{II}^*(\theta) &= K_I F_{21}(\theta) + T\sqrt{s} G_2(\theta) \\ G(\theta) &= (K_I^*(\theta)^2 + K_{II}^*(\theta)^2)/E \end{aligned} \tag{3.8}$$

To determine the value of the T-stress, we conducted a static elasticity analysis with a fixed geometry. Both the long and short samples were subjected to a unit displacement. The T-stress value was then extracted using the I-integral method. In our analysis, we obtained a T-ratio of $\frac{T\sqrt{L}}{K_I} = 0.93$ for the long sample and -1.38 for the short sample. These values are consistent with the results reported in (Mesgarnejad et al., 2020).

The comparison of the results reveals that the AT1 phase-field model with weakly anisotropic surface energy provides excellent predictions that align with both experimental results and GMERR predictions that consider the T-stress. Furthermore, an interesting finding is that as the anisotropic coefficient A_t increases, the influence of the T-stress on crack path selection becomes negligible. Specifically, when $A_t > 4$, considering the T-stress in GMERR predictions becomes unnecessary. The experimental and numerical results for the long sample emphasize the significant impact of the microstructure on the crack path. As the volume fraction of fibers oriented along 90° increases (corresponding to an increasing anisotropic coefficient in the numerical simulations), the crack path gradually shifts towards the direction of fiber orientation. This observation highlights the influence of the microstructural characteristics (volume fraction of the fiber).

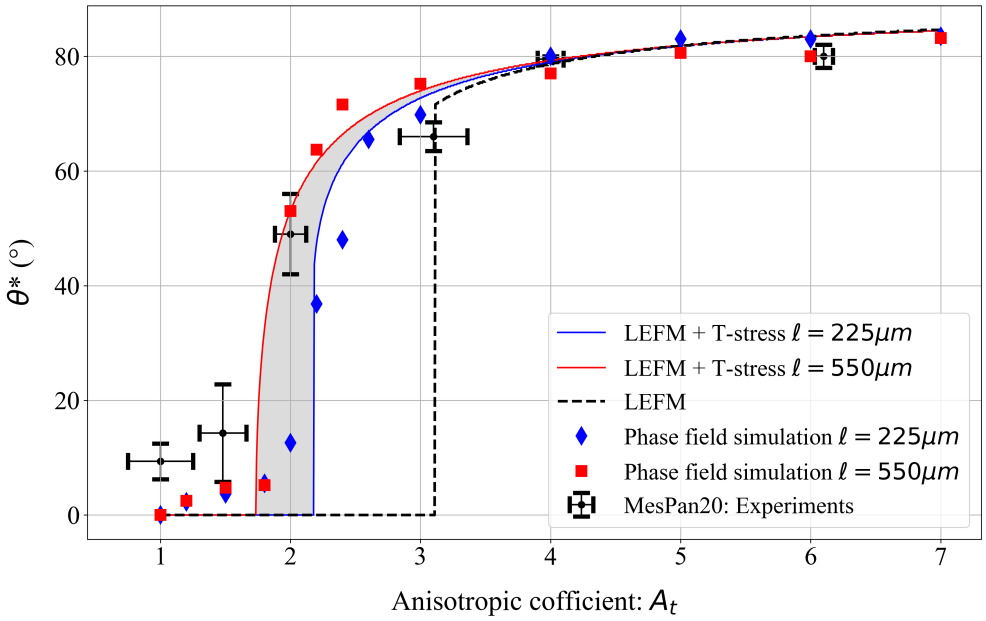

Figure 3.16 Comparison between numerical predictions and experimental results for long sample. Experimental results involves the crack path in fracture experiments with different fraction volume f_v from 0.01-0.07. The fraction volume were translated in the degree of anisotropy A_t using the experimental data: fig.8 d) in (Mesgarnejad et al., 2020). Numerical results involves the predicted crack path by weak anisotropic phase-field model with different value of the anisotropic coefficient A_t and regularization $\ell = 225$ and 550μm. Also the GMERR prediction in LEFM framework is presented. With the black-dot line are the LEFM prediction without T-stress, blue and red curve are LEFM prediction by taking into account the T-stress.

Fig. 3.17 illustrates the damage field of the long and short samples at different values of the anisotropic coefficient A_t, while maintaining a fixed material axis of $\theta_0 = 90°$. Notably, the crack path exhibits a change in direction as the anisotropic coefficient increases in the long sample. However, in the short sample, the crack angle consistently remains at 0°. This behavior can be explained by referring to the Wulff diagram depicted in Fig. 3.18. The crucial distinction between these two samples lies in the sign of the T-stress. When the T-stress is positive, the reciprocal of the energy release rate $\frac{1}{G(\theta)}$ forms a convex function. However, as the T-stress becomes negative, this reciprocal function becomes non-convex. As a result, in the short sample, as the anisotropic coefficient increases, the crack path always remains at 0°. This is due to the intersection point between the reciprocal of the energy release rate $\frac{1}{G(\theta)}$ and the reciprocal of the surface energy $\frac{1}{G_c(\theta)}$ occurring at 0°. These findings indicate that both microstructure and macrostructure configuration influence the selection of the crack path.

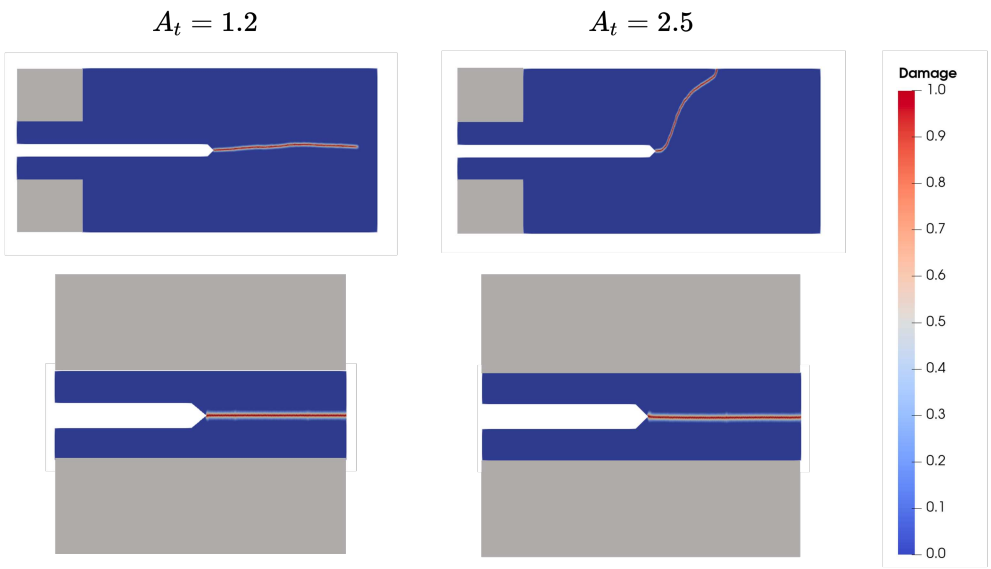

Figure 3.17 Snapshot of the numerical predicated crack path by weak anisotropic model with different coefficient A_t for different sample. First row and second row shows the simulation results for long sample and short sample, respectively.

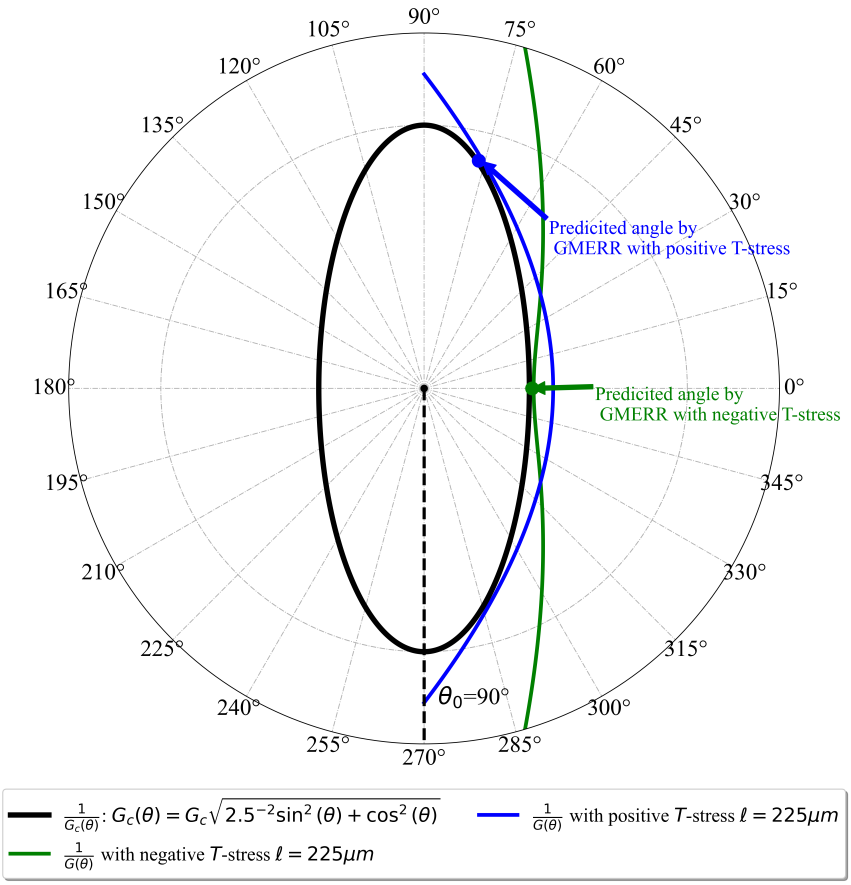

Figure 3.18 Wulff diagram, GEMRR visualization: black curve shows the reciprocal surface energy in form: $G_c(\theta) = G_c\sqrt{2.5^{-2}\sin^2(\theta) + \cos^2(\theta)}$, green and blue line represents the reciprocal energy release rate taking into account negative and positive T-stress with $\ell = 225\mu$m, respectively.

We then shift our focus to investigating a scenario where the anisotropic coefficient A_t is fixed at 2.5, corresponding to a volume fraction of fibers $f_v = 0.04$ in the experiments. However, we now vary the material axis θ_0 for both the long and short samples. It is important to note that in our numerical simulations, the material axis θ_0 represents the fiber orientation α_Γ in the composite material. Figure. 3.19 presents a comparison of experimental, theoretical, and numerical results for the predicted crack angle as a function of the fiber orientation α_Γ. The results showed that the AT1 phase-field model with weakly anisotropic surface energy provided accurate predictions for varying fiber orientation, aligning closely with both experimental results and GMERR predictions that took into account the T-stress. Furthermore, with AT1 damage model, we successfully replicated the numerical predictions as outlined in Mesgarnejad et al. 2020, where the KKL damage model was employed. It is evident that these two damage models demonstrate nearly identical performance in predicting crack propagation under conditions of weak

anisotropy. Combining the previous results with the findings presented here validates our implementations of the AT1 phase-field model with weakly anisotropic surface energy.

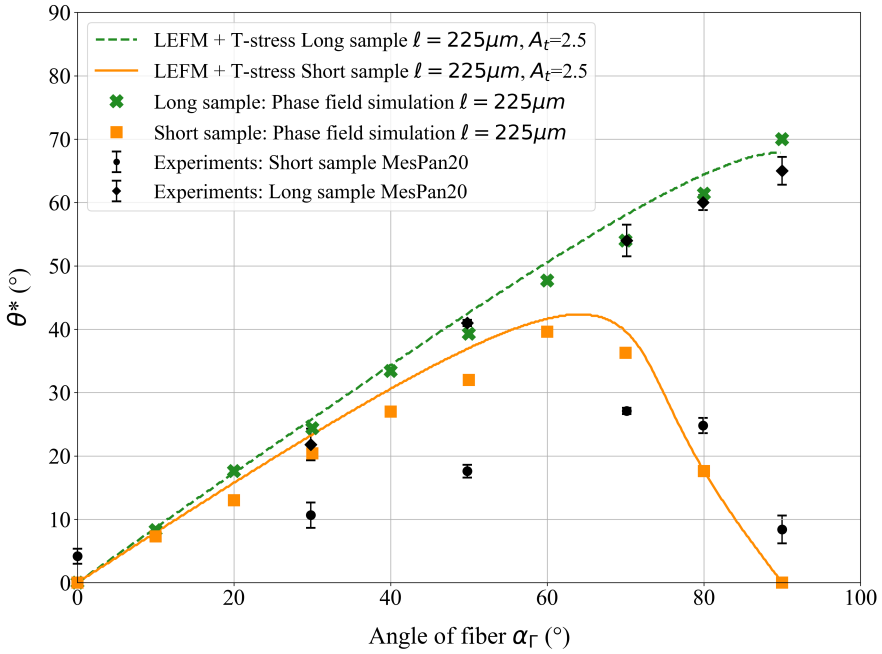

Figure 3.19 Comparison between numerical predictions and experimental results for long and short sample. Experimental results involves the crack path in fracture experiments with different fiber orientation α_Γ and fixed friction volume f_v =0.04 (corresponding anisotropic coefficient A_t=2.5). Numerical results involves the predicted crack path by weak anisotropic phase-field model with different fiber orientation and regularization ℓ = 225μm. Also the GMERR prediction in LEFM framework is presented. The LEFM prediction taking into account the T-stress. Green and orange color represent the results for long and short sample, respectively.

3.3 Conclusions

In summary, our study involved the validation of a numerical model for determining SIFs across a kink and fracture parameters using the I-integral method in the context of static elasticity problems. We then compared our numerical predictions for the damage evolution problem with experimental results from existing literature, thereby confirming the accuracy of implementing both the AT1 phase-field model with isotropic and weakly anisotropic surface energy.

We demonstrated the capability of the phase-field model with a linear dissipation function (w(α) = α, AT1) to accurately predict crack paths and critical forces. This validation holds significant importance as the higher-order phase-field model proposed by

Li and Maurini 2019 also incorporates a similar linear dissipation function ($\mathrm{w}(\alpha) = 9\alpha$). Thus, the validation of the AT1 phase-field model acts as a smooth transition towards the higher-order model.

Our next chapter will expand the study to include a higher-order phase-field model with strongly anisotropic surface energy. This extension will allow us to investigate crack propagation in our 3D printed sample. Furthermore, we will utilize the validated GMERR prediction procedure in cases involving strongly anisotropic surface energy, providing valuable insights and understanding.

Chapter 4

Numerical investigation versus fracture experiments in CT and CTS tests

In this chapter, we focus on comparing numerical results with experimental data. The first step involves validating the measured SIFs by comparing them with numerical results obtained from solving a static elasticity problem with a fixed geometry. Furthermore, we utilize the numerical model to determine the elastic constant of the printed CT sample.

To tackle the damage evolution problem with strongly anisotropic surface energy, we utilize a higher-order phase-field model. In order to compare with our fracture experiments on 3D printing part, we carefully determine the numerical parameters, especially the anisotropic constants that contribute to the surface energy. Moreover, we identify appropriate boundary conditions based on experimental data. By comparing the simulation results with the experimental data, we demonstrate the model's capability to predict crack trajectories and the corresponding critical load. These predictions can also be obtained through the GMERR within a LEFM framework.

Lastly, we delve into the discussion regarding the selection of the regularization parameter ℓ of the higher-order phase-field model.

Contents

4.1 Static problem: linear elastic solution

4.1.1 Boundary condition of CT specimens

As presented in previous section 3.1, the nodal loading boundary condition was adopted to validate the SIFs across a kink, as depicted in in Fig. 4.1 (1). However, it has been discussed in Triclot et al. 2023 that this boundary condition does not accurately simulate the loading process of a CT sample due to the complex numerical challenges associated with modeling the contact between the bolt and pin hole. Some influencing factors between the bolt and specimen are completely neglected in our model, such as the gaps between the bolts and CT specimen, the friction generated by the possible rotation of the bolt in the pin hole as the applied displacement increases.

To avoid the complexity of incorporating these influencing factors into the model, we introduce the DIC boundary condition in Fig. 4.1 (2) (Triclot et al., 2023). A sub-domain of the CT sample was modeled based on the experimental displacement field obtained by the DIC software UFreckles20. An example of extracted displacement field for CT specimen is shown in Fig. 4.2. The experimental displacements field is obtained using a finite element formulation of DIC with bi-linear quadrilateral (Q4) elements (element size 16×16 pixel), and then applied to the corresponding points of the selected contour in Cast3M, with the right boundary of the CT sample (represented by the green curve in Fig. 4.2) considered as a traction-free boundary.

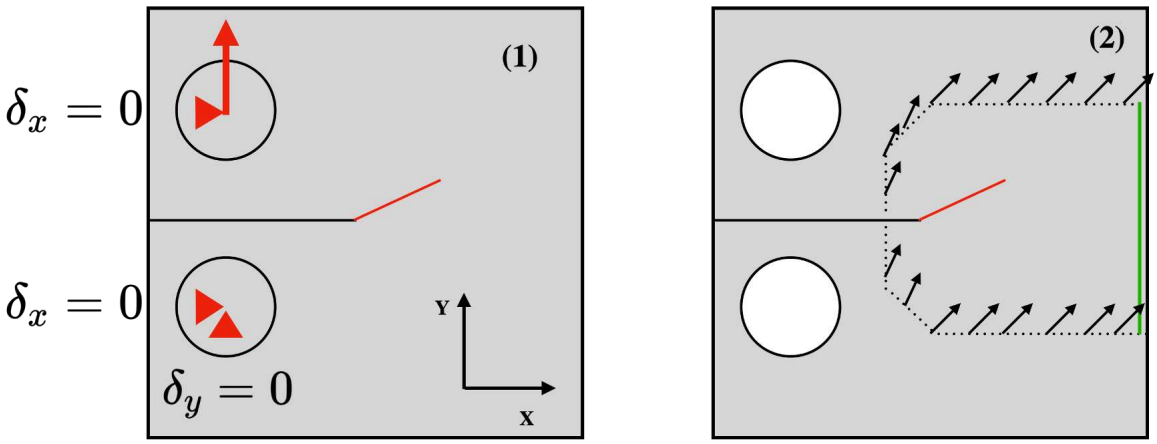

Figure 4.1 Different boundaries conditions used: (1) Nodal loading and (2) DIC boundary condition

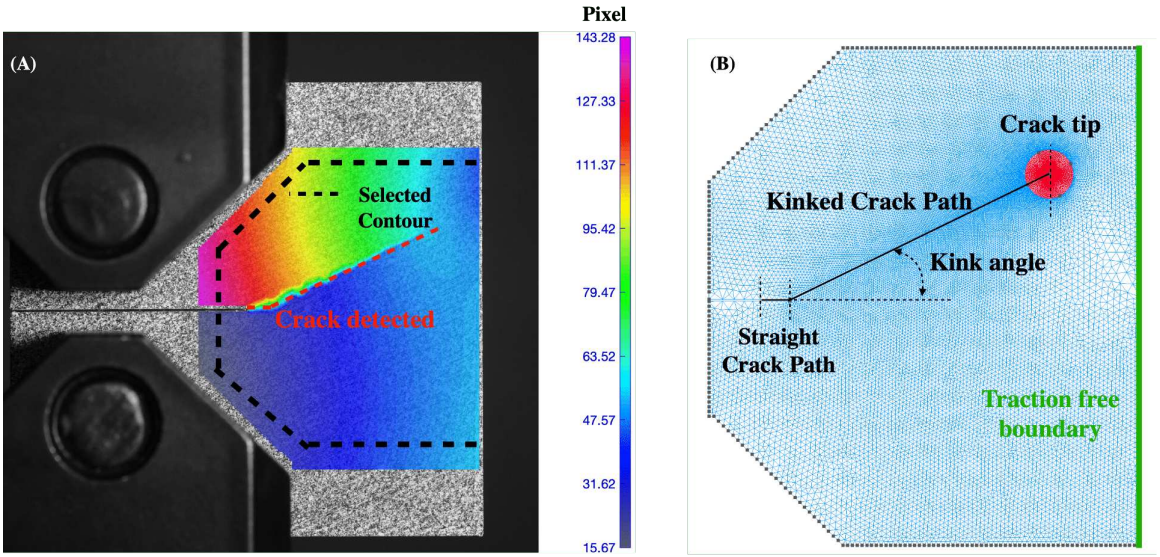

Figure 4.2 Extracted displacement field obtained from DIC: (A) 3rd contour (counts from the outside to the inside) was extracted as inputs for the finite element modeling, (B) sub-domain mesh is shown in Gmsh (6000 Qua8 elements in near crack tip circle and 40000 elements for entire model)

4.1.2 Comparison results between experiments and simulations

Figure 4.3 presents a comparison between the experimental and numerical results of the SIF and T-stress relative to the applied displacement in the y direction, indicating the evolution of SIF and T-stress throughout the fracture experiment during crack propagation. The left column corresponds to CT specimens with a raster angle of 0°, while the right column corresponds to a raster angle of 25°. It is worth noting that the

Young's modulus and crack tip position play an identical role in both the experimental and numerical results for SIF and T-stress. Thus, variations in these variables will not impact the comparison between the experimental and numerical results. In our mesh, we employed approximately 40,000 elements, including 6,000 Qua8 elements in the vicinity of the crack tip circle. The $G-\theta$ method is applied at the 10th layer surrounding the crack tip.

The comparison of the results reveals that the SIF obtained using the nodal loading boundary condition is significantly overestimated and does not align satisfactorily with the experimental results. This suggests that nodal loading boundary conditions are not suitable for accurately extracting the SIF and T-stress during the finite element calculation of the CT sample. In contrast, the SIF obtained from finite element modeling with the DIC boundary condition exhibits excellent agreement with the experimental results. This provides valuable insights into validating the linear elastic isotropic assumption. We acknowledge that a small offset still exists, but it remains within acceptable tolerances. Additionally, for the kinked CT sample (25° raster angle), the experimental SIF values obtained using DIC become unreliable near the kink position (applied displacement from 1.26 mm to 1.45 mm). This is attributed to the presence of a kink in the extraction region, which hinders the precise determination of asymptotic coefficients (Williams series is defined for a straight crack (Williams, 1952)). Therefore, by using finite element modeling with the DIC boundary condition, we can obtain accurate SIF values near the kink position.

Regarding the comparison of T-stress during propagation, a significant discrepancy exists between the experimental and numerical results. In the experimental analysis, the T-stress was extracted by projecting the displacement field onto the Williams series. However, since the T-stress is the second-order term in the Williams series, the obtained values lack accuracy. On the other hand, in the numerical analysis, the T-stress was obtained using the direct method, which necessitates a convergence region where the T-stress reaches a stable value.

In summary, the use of DIC boundary condition enables the prediction of SIFs evolution in the presence of a crack kink, compared to other boundary conditions. Additionally, the DIC boundary condition allows for the accurate determination of the SIFs value near the kink position, compensating for the lack of experimental information and validating the experimental measurements from CT samples. Furthermore, we validates the assumption of isotropic linear elasticity adopted for the printed samples.

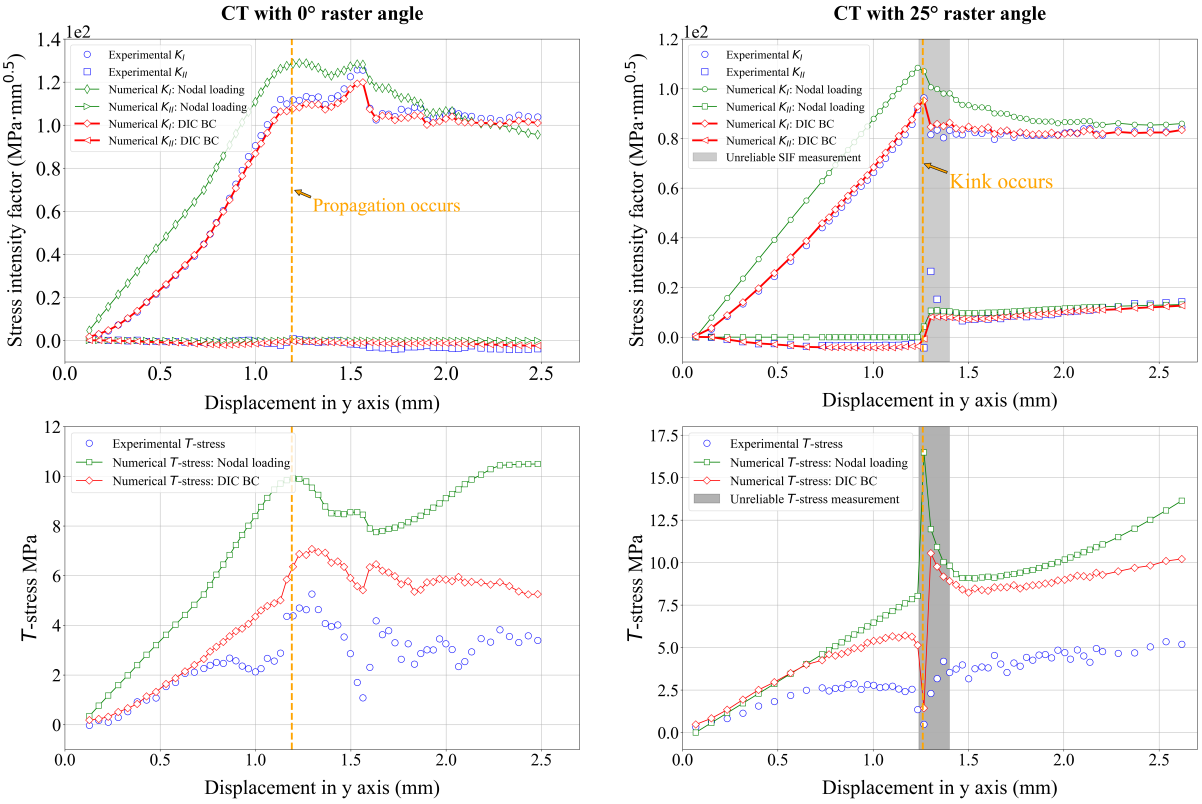

Figure 4.3 Comparison with experimental results with different boundary conditions: evolution of SIF and T-stress relative to the imposed displacement for CT sample without and with kink (left raster angle 0° and right raster angle 25°). And blue dots represent the experimental results. Green and red curves represent the numerical results using Nodal loading boundary condition and DIC boundary condition, respectively (50000 elements used, and numerical convergence is reached with 20000 elements).

4.1.3 Determination of Young's modulus of printed CT sample

Due to the complexity of the printing process, there is uncertainty regarding whether the elasticity constants obtained through a tensile test accurately represent those of the printed CT/CTS samples. It is worth noting that the Young's modulus and crack tip position intervene same way in both the experimental and numerical results for SIF and T-stress. Therefore, any variations in these variables will not impact the comparison between the experimental and numerical results. Consequently, the previous study can only validate the measured SIFs experimentally. However, determining the value of the elastic constant (Young's modulus) requires checking the loading curve.

In a recent study by Triclot et al. 2023, a 3D finite element model was employed to calibrate the Young's modulus of printed CT samples. The authors compared the Force versus Crack Opening Displacement (COD) curve between experimental and numerical results. One advantage of using COD as a reference instead of the Force-Displacement curve is that it remains unaffected by the boundary conditions employed in the numerical simulation. Consequently, they discovered a significant 50% increase in the Young's modulus when compared to the values obtained from the tensile test.

The authors suggested that the higher Young's modulus may be attributed to the variations in size and geometry features between the dog-bone and CT samples. However, these findings have not been reported in other additive manufacturing literature. Additionally, it was observed that the calibrated Young's modulus is strongly influenced by the location of the COD measurement on the crack lip relative to the crack tip position. Given these factors, an alternative method was employed in our study to investigate the Young's modulus of printed CT samples.

Based on the previous study, the most straightforward and convenient approach for modeling the CT sample involves utilizing the displacement field obtained from experiments as the boundary condition. Therefore, instead of comparing the load curve between numerical and experimental data, our objective is to compare the displacement field of a selected zone in the CT sample during the linear elastic phase. This process is depicted in Figure 4.4, where the measured displacement field allows us to extract data from a chosen contour, as shown on the left. This selected contour comprises approximately 200 points, each providing information about their pixel positions as well as the measured displacements in the x and y-axes during the loading of the CT sample.

Subsequently, this selected contour is incorporated into a full-size 3D FE model, as illustrated on the right side of the figure. The 3D model is then subjected to the experimentally measured force, and we extract the numerical displacement of the selected contour. It has been shown that while the results are very sensitive to the way the

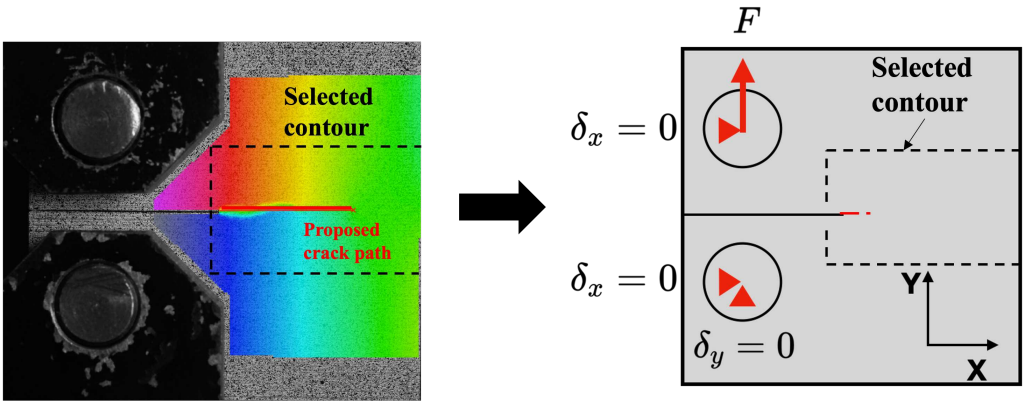

Figure 4.4 Process of calibrating the elastic constants using a 3D numerical model: The measured displacement field is used to extract a selected contour (left), which is then inserted into a 3D FE model (right).

displacement is applied, they are insensitive to the way a force is applied, in accordance with Saint Venant's principle (Triclot et al., 2023). By varying the input value of the Young's modulus, our aim is to identify the simulation results that best approximate the experimental displacement field.

The study employed a CT sample with a raster angle of 0° to examine a pre-existing crack of length a_0 using DIC for identification purposes. A mesh was generated using UFreckles20 based on the images captured during the experiments, as depicted in fig. 4.5 A). The measured displacement field in the y-axis is illustrated in fig. 4.5 B). By analyzing the discontinuity in the displacement field, we proposed a crack path indicated by the red line to determine the position of the successive crack tip. The crack extension, relative to the number of images, is presented in fig. 4.6. Notably, the crack extension initially increased with the growing load but then remained constant, despite the continued load increment. This period is considered to be a linear elastic phase without crack propagation, occurring as the applied displacement increased, specifically between image N° 5 and N° 20. Consequently, the estimated pre-crack length a_0 was determined to be 26.64 mm.

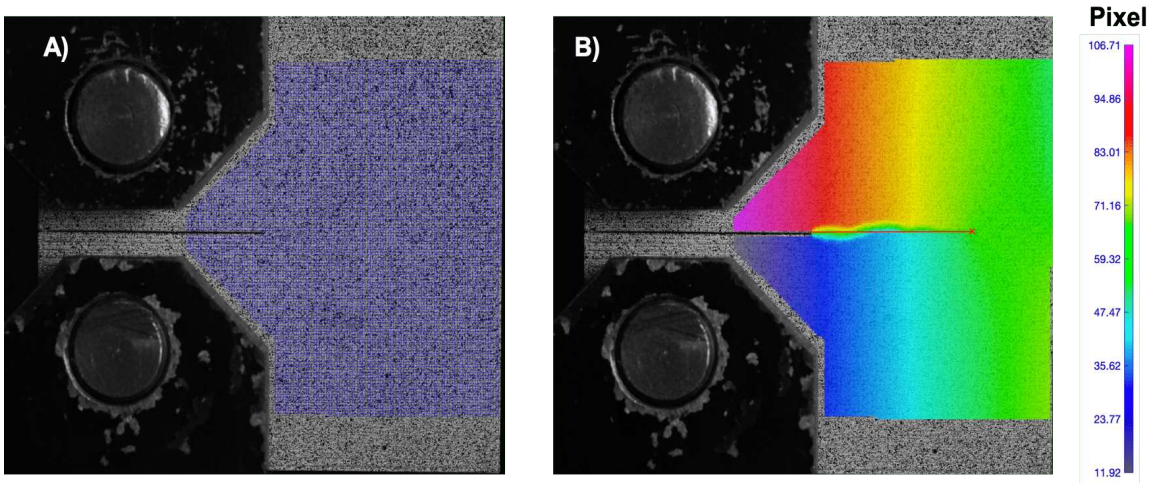

Figure 4.5 DIC analysis for CT sample with a raster angle of O°: (A) displays the mesh produced by UFreckles using 16x16 pixel element size. (B) presents the vertical displacement field in pixels, where the red line indicates the suggested crack path for determining the successive crack tip position based on the discontinuity of the displacement field.

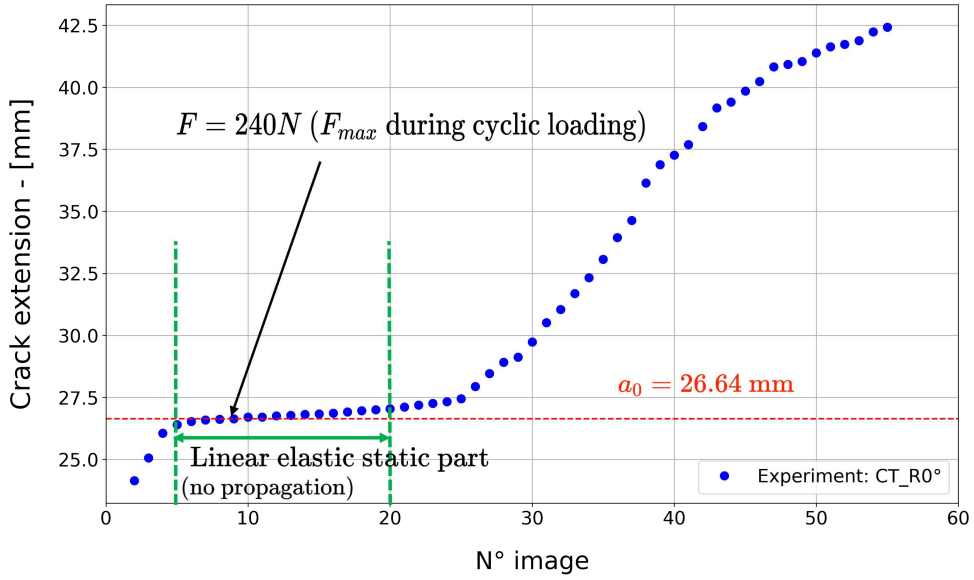

Figure 4.6 The crack extension is plotted as a function of the number of captured images

Fig. 4.7 displays the displacement field data extracted from the DIC analysis. Each point indicating a nodal position on the generated mesh and contains displacement values in the x- and y-axes during the fracture experiment. We selected three contours from extracted displacement field data as shown in fig. 4.7 and inserted them into a full-size CT sample to generate a 3D mesh file using Gmsh. Subsequently, Cast3M was utilized to perform calculations based on the solution of a linear elastic problem at a fixed crack

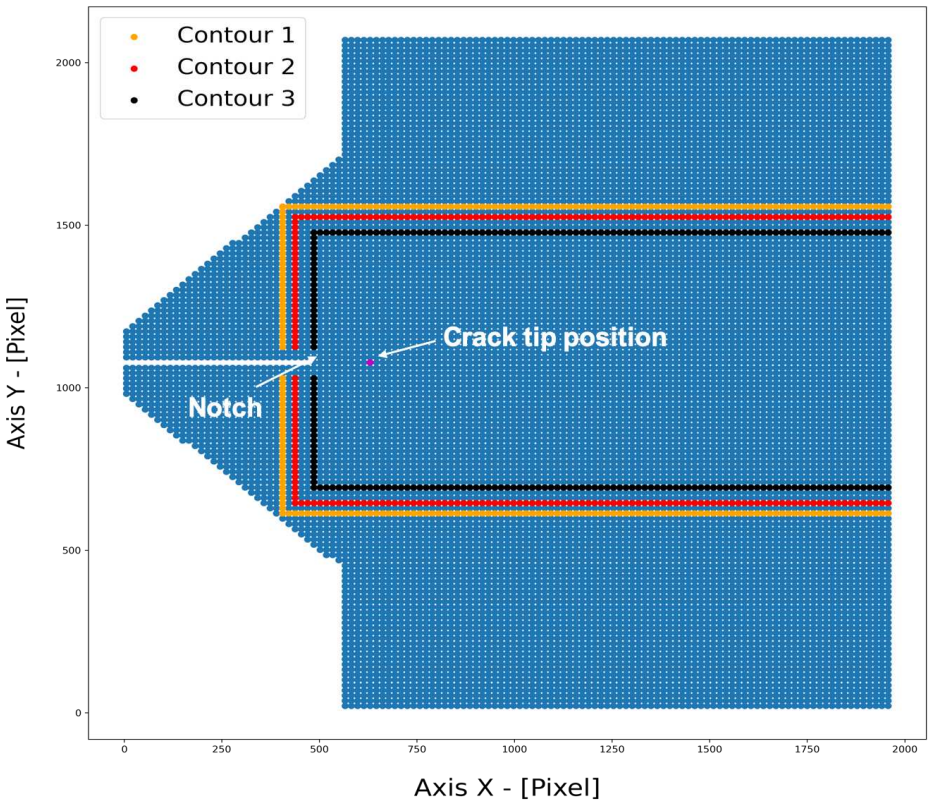

Figure 4.7 The data obtained from the DIC analysis includes the position and displacement values along the x and y axes for each nodal point on the mesh generated in UFreckles. Each point on the graph corresponds to a nodal point on the mesh.

tip position $a_0 = 26.64$ mm. The input data consisted of force measurements acquired through fracture experiments, while the output data consisted of the displacement field of the selected contour with different Young's moduli. In the FEM calculation, as depicted in fig. 4.4, a force was applied to the center of the upper bolt in the pin hole, while the lower side remained fixed.

Fig. 4.8 displays the comparison between the experimental and numerical displacement fields, specifically focusing on the third contour at image 20, where a force of 590 N was applied to the bolt. The black dot-line represents the experimental position after deformation, while the dots of various colors represent the simulated results obtained using different values of Young's modulus. To enhance the interpretability of the results, we calculated the absolute difference between the positions of each contour in the experimental and numerical data. The absolute difference between the experimental and numerical contour positions after deformation is computed using the following expression:

$$\text{Absolute difference} = \frac{1}{N}\sum_{i=1}^{N}[\sqrt{(x_i^{num} - x_i^{exp})^2 + (y_i^{num} - y_i^{exp})^2} \cdot 100] \tag{4.1}$$

where x_i and y_i represent the position of the deformed point i in the selected contour, and N denotes number of points in the selected contour.

The absolute difference between the experimental and numerical contour position after deformation indicates the closeness of the simulation to the experiment. A smaller value implies a closer match. The absolute difference value with respect to the number of image for different contour are shown in fig. 4.9. It is noteworthy that the comparison results are independent on the selected contour. Additionally, we found that the Young's modulus of the printed sample is approximately 1900 MPa.

To determine the exact value of the Young's modulus for the printed CT sample, we conducted FEM calculations to obtain the minimal absolute difference. Figure 4.10 presents the average absolute difference values from image 5 to image 20 of the third contour. The optimal value of the Young's modulus is the one that yields the minimum average absolute difference, which is about 1950 MPa. This obtained value for the printed CT sample aligns with the results of the tensile tests presented in section 2.3.1.1. Consequently, it can be concluded that the elastic properties of printed sample by fused deposition in polycarbonate are not affected by different size and geometry features.

In the study conducted by Triclot et al. 2023, it was observed that the position of the extracted COD was found to be too close to the crack tip, which could be influenced by the fracture process zone. When comparing the results obtained from the displacement field using a specific contour, it was noted that the numerical displacement field, which utilized a Young's modulus of E = 2700 MPa near the crack lip, exhibited significant deviations from the experimental results.

However, it was discovered that when calculating COD as the difference in displacement between upper and lower points located on the crack lip, the error was effectively canceled out. Consequently, this led to a higher value of Young's modulus (E = 2700 MPa) being obtained. Additionally, it was found that the calibration of Young's modulus using the F-COD method was highly sensitive to the experimental measured COD value. Even a slight offset of 0.032 mm in the COD value may result in a 50% increase in the estimated Young's modulus.

In comparison, the use of a selected contour to compare the displacement fields was deemed to be more accurate and reliable. This was primarily due to the fact that each contour contained a larger number of data points (approximately 200 points), which minimized the influence of small differences and reduced the potential for significant errors.

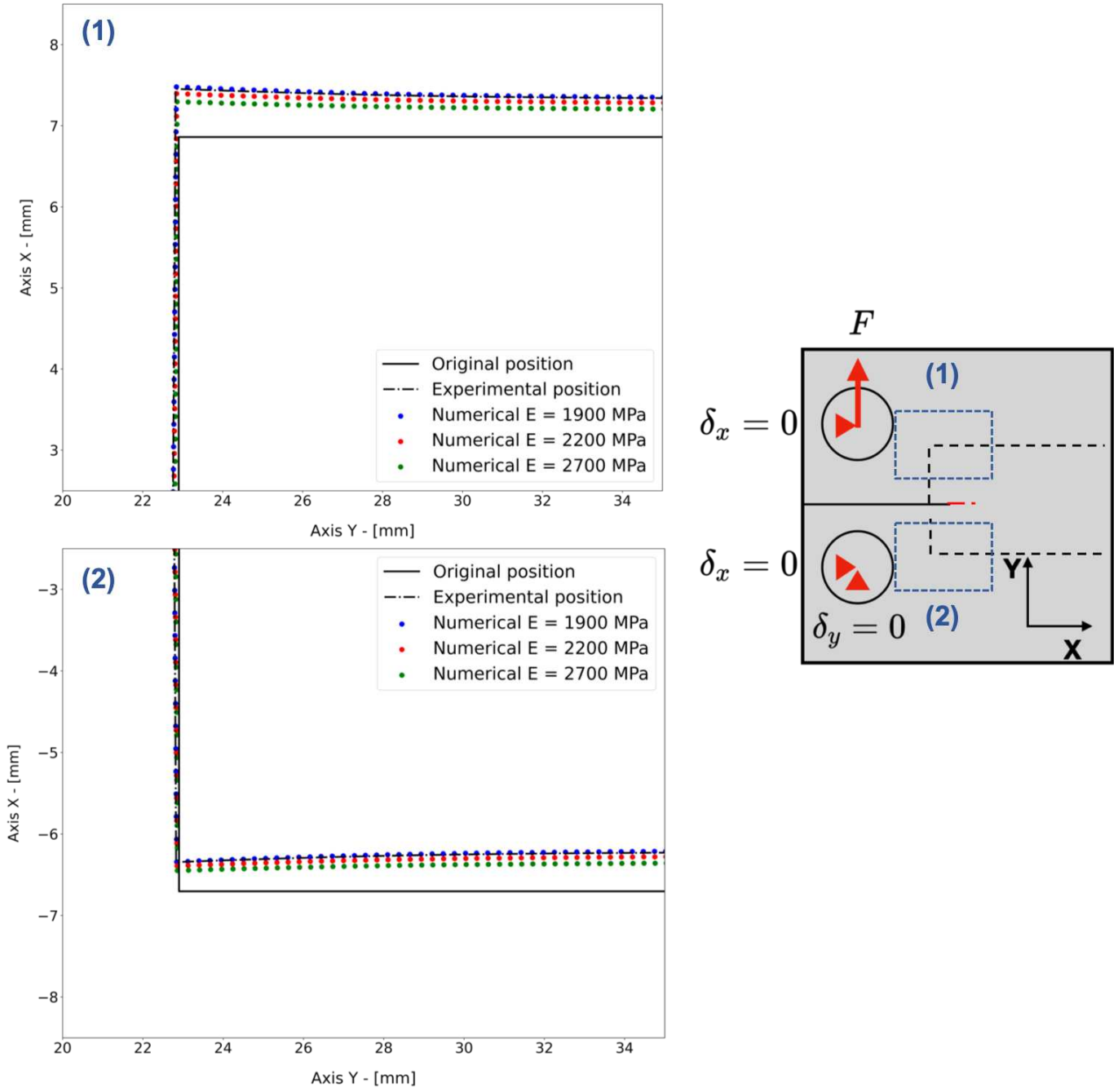

Figure 4.8 Comparison of the displacement field for the third contour at image 20 (with an imposed force of 590 N) between experiments and simulation is presented in this figure. The zoomed-in views of the upper and lower sides are shown in (1) and (2), respectively. The initial position of the sample is represented by the black line, and the experimental displacement field is shown as a black dot-line. The blue, red, and green dots correspond to the numerical displacement fields obtained using the Young's modulus values of 1900 MPa, 2200 MPa, and 2700 MPa, respectively.

Furthermore, this study provides an explanation for the disparities in SIFs values observed when employing pin loading and DIC boundary conditions. The complexity of the contact problem between the pin and pin hole makes it challenging to accurately capture the local displacement field when using the pin nodal boundary condition, resulting in deviations from the experimental results.

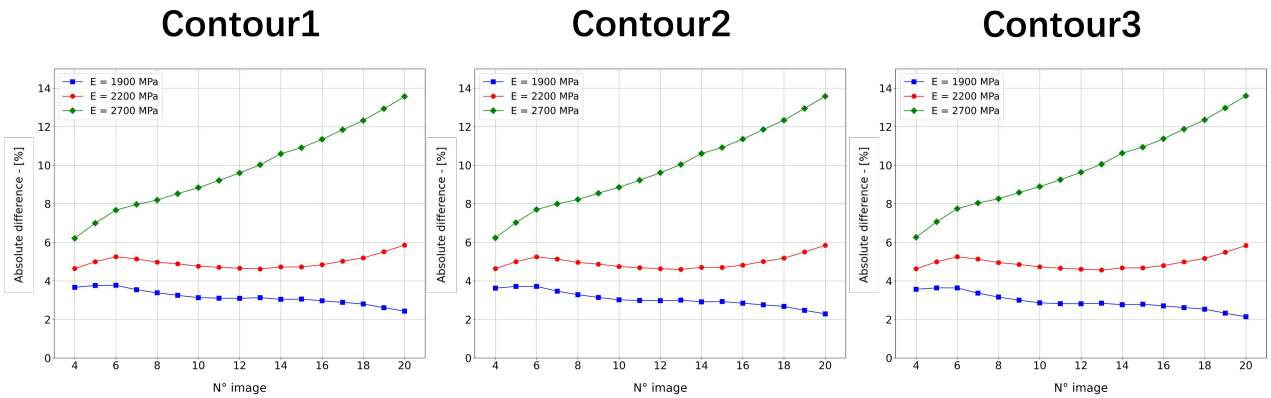

Figure 4.9 The absolute difference between different contours is shown as a function of the number of images.

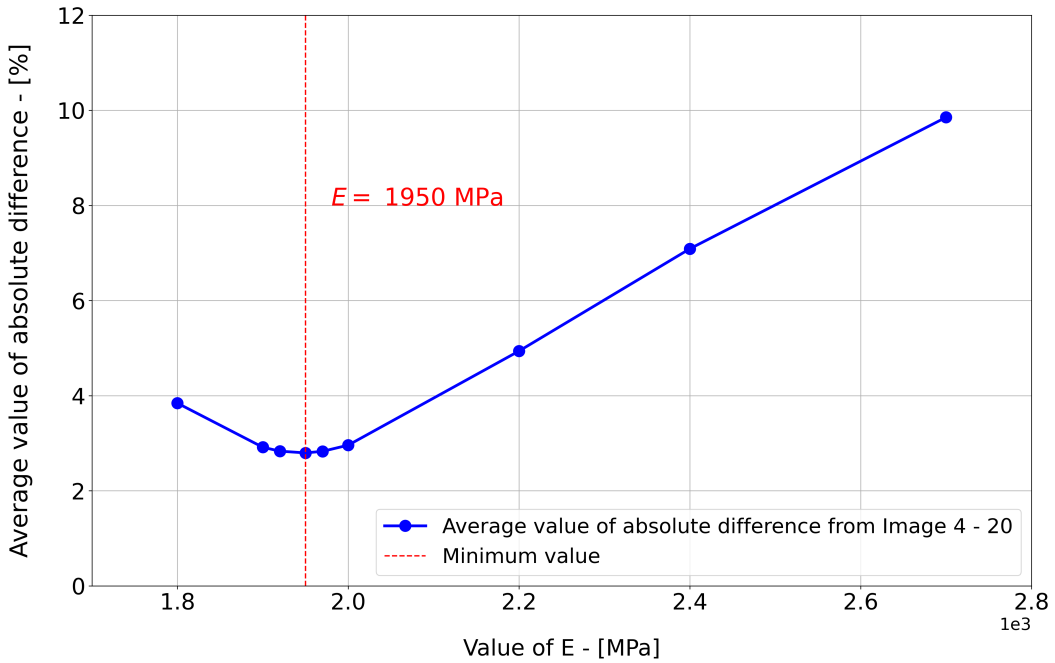

Figure 4.10 The average absolute difference between different values of Young's modulus from image 5 to image 20.

4.2 Phase-field modeling with strongly anisotropic surface energy

In this section, we investigate the fracture problem with strongly anisotropic surface energy using the higher-order phase-field model as presented in Section 1.4.3.2. To accommodate the requirements of the higher-order phase-field model, which necessitates a C^1 continuity finite element formulation, we adopted the Mixed Interpolation of Tensorial Components (MITC) formulation, as discussed in previous works Hale et al. 2018; Li and Maurini 2019. Alternative methods include isogeometric analysis refer to Li et al. 2015 and the utilization of Power-Sabin B-Splines, as described in Chen et al. 2021.

In comparison to the AT1 phase-field model, the anisotropic model demands additional numerical parameters to described the anisotropic surface energy. To determine these parameters, we initially focus on examining the mode I fracture problem using a CT sample. Since the form of the surface energy is known (as shown in eq. 1.43), we can therefore adopt the GMERR prediction to investigate the choice of the anisotropic coefficient A_f. By comparing the numerical results with the GMERR prediction and experimental crack path, we can determine the appropriate numerical parameters for the anisotropic surface energy. These parameters, combined with the material parameters obtained from fracture experiments, are then employed in the subsequent numerical experiments. It is noticed that the numerical experiments were carried out under assumption of 2D plane stress.

We aim at seeking for both predicted crack path and its relevant critical force. We will first examine the mode I problem with CT sample and then mode I+II with CTS sample. The numerical predictions, which encompass the crack path and critical force, will be presented and compared against experimental data and theoretical predictions.

4.2.1 Determination of boundary conditions and numerical parameters using CT sample

Determining an appropriate boundary condition remains a challenge due to the complex numerical issues associated with modeling the contact between the bolt and pin hole. In the previous section, we found that the DIC boundary condition, as presented in Section 4.1.1, closely resembles the experimental conditions. However, using the DIC boundary condition makes it difficult to obtain the relevant critical force. Hence, for phase-field modeling, we adopted an alternative boundary condition.

To ensure that the boundary condition closely aligns with the experimental setup

while avoiding excessive complexity, we initially neglected the friction resulting from the rotation of the bolt within the pin hole of the CT sample as the applied displacement increases. Based on experimental observations, we observed that only a certain area of the pin hole was loaded, as depicted in fig. 4.11. We defined the angle of this loaded area as the "pin angle" (ϕ). We hypothesized that the numerical SIFs near the crack tip should match the experimental values when the pin angle is well defined in the numerical simulation. So as to determine the pin angle for our numerical experiments, we computed the numerical dimensionless SIF $\frac{K_I\sqrt{a_0}}{E\delta}$ values by varying the pin angle and compared them with experimental data. Note that under assumption of linear elasticity, the dimensionless quantity doesn't depend on displacement δ for a given pin angle ϕ. The comparison is presented in fig. 4.12, with different colors indicating different applied displacements. We observed that the experimental dimensionless SIF increases with increasing applied displacement, suggesting that the contact angle increases during the fracture experiments prior to crack propagation. Additionally, it was observed that crack propagation commenced along the direction of the kink at an applied displacement of approximately 1 mm during fracture experiments as shown in fig. 2.17. Therefore, we adopted the associated pin angle of approximately 50° (blue dot line $\delta = 1$ mm as depicted in fig. 4.12) for our numerical experiments and assumed it remains constant.

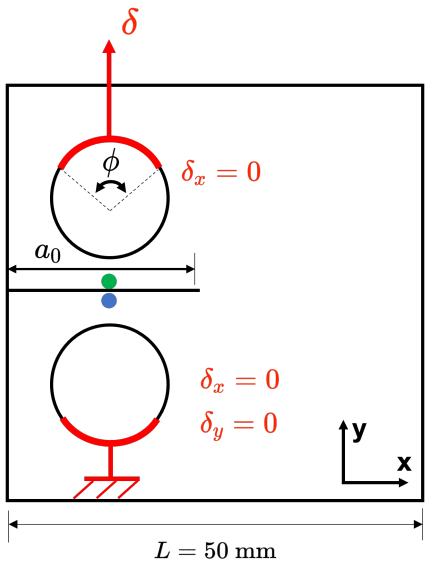

Figure 4.11 Schema: Boundary conditions used in phase-field modeling for CT samples. The difference in the y-axis displacement between blue (upper side) and green point (lower side) is defined as the COD. These two points are aligned with the center of the pin along the x-axis.

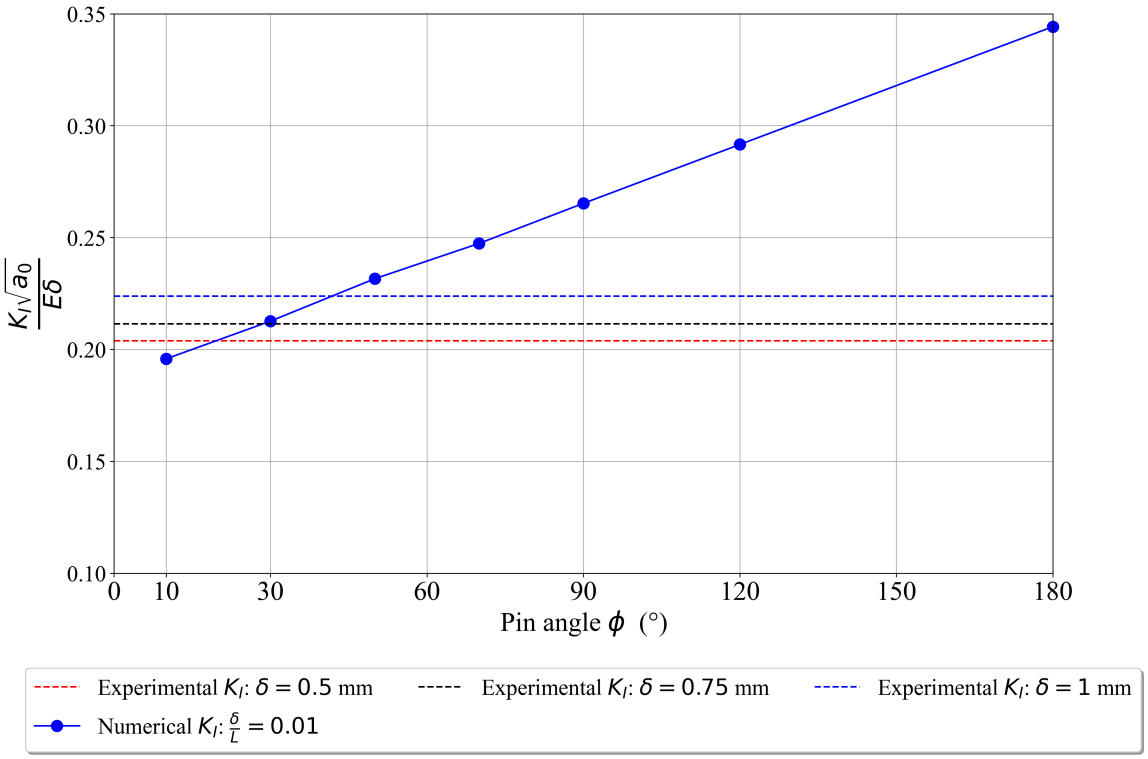

Figure 4.12 Dimensionless value of numerical SIF with respect to the pin angle ϕ compared with experimental values. The dotted lines are the experimental values for different applied displacements (mean values of 18 tested CT samples).

As for the determination of anisotropic constants, we employed an anisotropic surface energy with cubic symmetry, which aligns with the criss-cross printing method used for our CT and CTS samples. This printing method results in two mutually orthogonal weak planes corresponding to the direction of the infill angle. To simulate different raster angles, we rotated the orientation-dependent $G_c(\theta)$ by transforming the matrix $\mathbb{C}$ using eq. (1.44). Due to the cubic symmetry, our numerical experiments required three numerical parameters in the matrix $\mathbb{C}$ (eq. (1.42)) to simulate the strongly anisotropic surface energy. As shown in (Li and Maurini, 2019), the form of the four-fold symmetry surface energy in terms of constants in matrix $\mathbb{C}$ is shown as follows:

$$G_c(\theta) = G_0 \sqrt{\frac{3C_{11} + C_{12} + 2C_{44}}{4} \left(1 + \frac{C_{11} - C_{12} - 2C_{44}}{3C_{11} + C_{12} + 2C_{44}} \cos 4\theta\right)} \tag{4.2}$$

The orientation dependent surface energy $G_c(\theta)$ attains its maximum at $\theta^* = 0$, which can be interpreted as a sample with 0° raster angle ($\theta_0 = 0°$), therefore the previous

expression is simplified:

$$G_c(\theta^* = 0) = G_0\sqrt{C_{11}} \tag{4.3}$$

It is noticed that the surface energy G_c along the weak plane equals to the numerical parameter G_0 multiplied by the anisotropic constants C_{11}, to avoid confusion, we set $C_{11} = 1$ to normalize the surface energy $G_c(\theta)$. This normalization ensures that the numerical parameter of G_c for the weak plane is directly related to the experimental surface energy.

We then selected $C_{12} = 0.5$ to satisfy the condition $C_{11}^2 > C_{12}^2$ and varied C_{44} to alter the anisotropy of the surface energy, subject to the constraint that the matrix $\mathbb{C}$ is positive definite. The rationale behind adjusting the numerical value of C_{44} is closely tied to altering the surface energy along the "forbidden direction." As G_c along the direction of the 'weak plane' remains constant, increasing the value of C_{44} results in a higher ratio between the surface energy along the weak plane and the "forbidden direction." Consequently, the surface energy becomes progressively more anisotropic as C_{44} increases. We considered C_{44} values ranging from (0.25, 198.25], and the associated anisotropic coefficient A_f varied between 0 to 0.99.

In the numerical experiments conducted by Scherer et al. 2022, they demonstrated that the degree of anisotropy in surface energy has an impact on the predicted critical load. As the surface energy becomes more anisotropic, the constraint on crack propagation becomes increasingly stringent in numerical simulations. Therefore, the choice of the anisotropic coefficient plays a crucial role as it influences both the selection of the crack path and the relevant critical force. Beside, as we know the physical interpretation of the anisotropic coefficient A_f is the ratio between the surface energy along the weak plane and the "forbidden direction". However, it is not possible to determine the surface energy along the "forbidden direction" experimentally, as the crack cannot be guided towards that direction. Consequently, the choice of the anisotropic coefficient becomes challenging, as it relies on understanding the influence of the anisotropy on the fracture behavior.

To determine the appropriate anisotropic coefficient, we conducted numerical tests with the anisotropic coefficient ranging from 0 to 0.99 along with a material axis $\theta_0 = 25°$. We anticipated that the predicted crack angle should align closely with the raster angle when the anisotropic coefficient is accurately defined. A comparison between the numerical results and the GMERR prediction is illustrated in fig. 4.13. The black dash-dotted line represents the predicted crack angle with respect to the anisotropic coefficient, the blue dots being the numerical predicted kink angles and the red curve being the material axis (raster angle). It is noticed that the numerical predictions

are agree with the GMERR prediction. Furthermore, we observed that the numerical prediction closest to the experiments, which involved a 25° raster angle, was obtained with an anisotropic coefficient of 0.99 (C_{44} = 198.25). While it is possible to enhance the anisotropy of the surface energy by increasing the value of C_{44}, it should be noted that excessively large values can sometimes result in convergence issues. Hence, it is not meaningful to blindly push this value A_f towards 1 indefinitely. Meanwhile, different from the results presented in Scherer et al. 2022, in Li's anisotropic model, the influence of anisotropic coefficient on predicted critical load is not significant. Consequently, we choose A_f = 0.99 to simulate our fused deposition fabricated specimens, whereby the corresponding surface energy is given by $G_c(\theta) = G_0\sqrt[4]{100 - 99\cos 4(\theta - \theta_0)}$. This choice allows us to capture the anisotropic behavior accurately and aligns with the experimental observations.

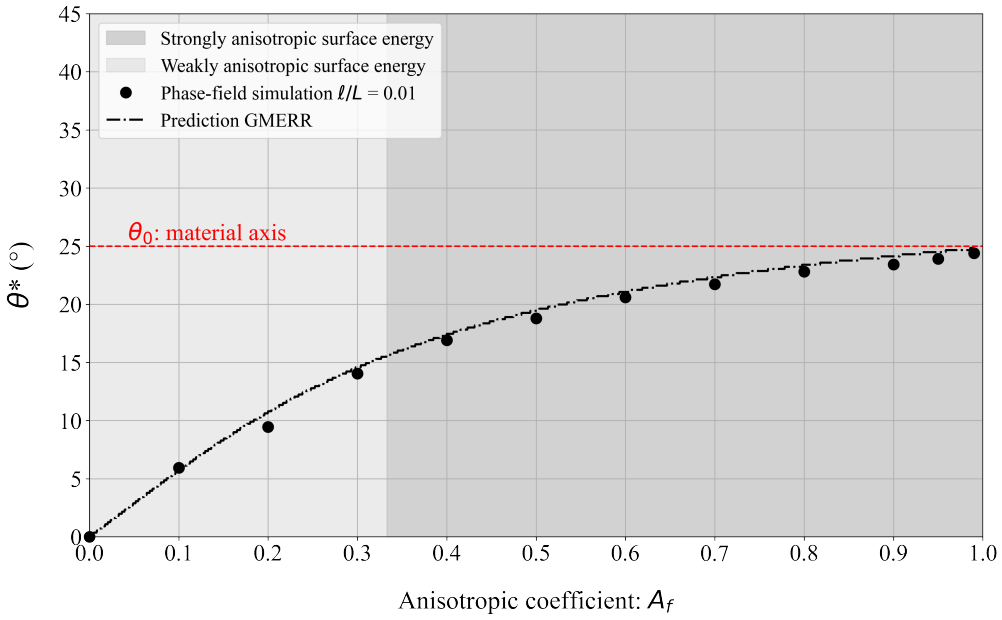

Figure 4.13 Comparison of predicted crack angles between GMERR and numerical predictions with different values of anisotropic coefficient A_f

Other numerical parameters like material parameters are obtained by tensile test and fracture experiments: E = 1900 MPa, ν = 0.34, the energy release rate G_c = 4.5 kJ/m^2, and material strength σ_c = 42 MPa. Additionally, to determine the regularization parameter of the weak plane ℓ_0, we adopted the expression presented in (Tanné et al., 2018). Depending on the selected damage model, the regularization parameter can be denoted as follows:

$$\ell_0 = \frac{45}{96}\frac{G_c E}{\sigma_c^2} \tag{4.4}$$

the estimated regularization parameter ℓ_0 was approximately 2.1 mm. However, this value appeared excessively large compared to the size of the specimens and the diameter of the extruded thread, which was 0.4 mm. Since the regularization parameter influences the width of the damage field and is inversely proportional to the critical stress σ_c, an adjustment was made to the estimate. To refine the estimate, numerical experiments were conducted using $\ell_0 = 0.4$ mm (the diameter of the printed thread) to obtain the upper limit of the critical force and $\ell_0 = 2.1$ mm (the estimated value determined by Tanné et al. 2018's formula) to obtain the lower limit of the critical force. The aim was to investigate whether the critical force observed in the experiments falls within the range of the numerical predictions using ℓ_0 values of 0.4 mm and 2.1 mm. The objective was to identify the optimal value of ℓ_0 by achieving a match with the experimental data.

4.2.2 Numerical predictions on crack path and critical force: a comparison with experimental data

In terms of the order of magnitude, the experimental data falls within the range of the predicted critical load when the regularization parameter ℓ_0 is chosen within the range of [0.4, 2.1] mm. Besides, the numerical predictions exhibit a perfect fit with the experimental results when ℓ_0 is set to 0.6 mm. Interestingly, numerical simulations accurately captured the correlation between the raster angle and the corresponding critical load. To further enhance our comprehension of the relation between the critical force and the raster angle, and given that we are specifically examining a CT sample subjected solely to mode I loading, the eq. (1.21) can be redefined as follows:

$$F_c(\theta) = \left[\frac{1}{F_{11}(\theta)^2 + F_{21}(\theta)^2}\right]^{0.5} \cdot F_c(\theta = 0) \tag{4.5}$$

where $F_{11}(\theta)$ and $F_{21}(\theta)$ are the universal functions appears in the Amestoy-Leblond's formula shown in eq. (1.12). Finally, we have access to the relation between critical force and the raster angle as depicted in fig. 4.14 (represented by the black dash line), we substituted the theoretical value of the unit force $F_c(\theta = 0)$ with the experimental value $F_c^{exp}(\theta = 0)$. Notably, the predictions made using the GMERR within the framework of LEFM align well with the experimental findings. Specifically, the critical load consistently rises as the kink angle increases, establishing a clear and monotonous trend.

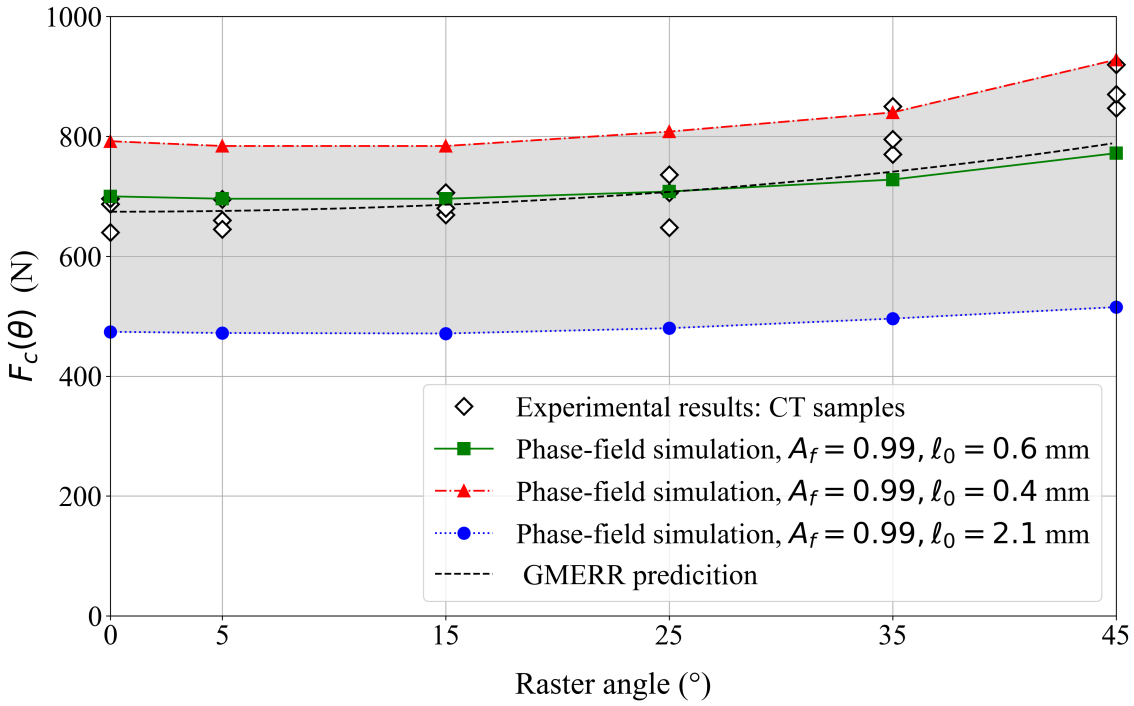

Figure 4.14 Comparison between experimental, numerical and theoretical results. Black dots are experimental data, each point represents 3 tested CT samples. Blue, green and red dot-lines are predicted critical force obtained by phase-field simulation. Black dash-line are theoretical prediction based on the energy release rate criterion.

A snapshot of the predicted numerical crack path in an anisotropic CT sample is illustrated in fig. 4.15, with regularization parameter $\ell_0 = 0.6$ mm. The black curve represents the associated reciprocal surface energy, and green curve represents the reciprocal energy release rate calculated using Irwin's formula and Amestoy-Leblond's formula.

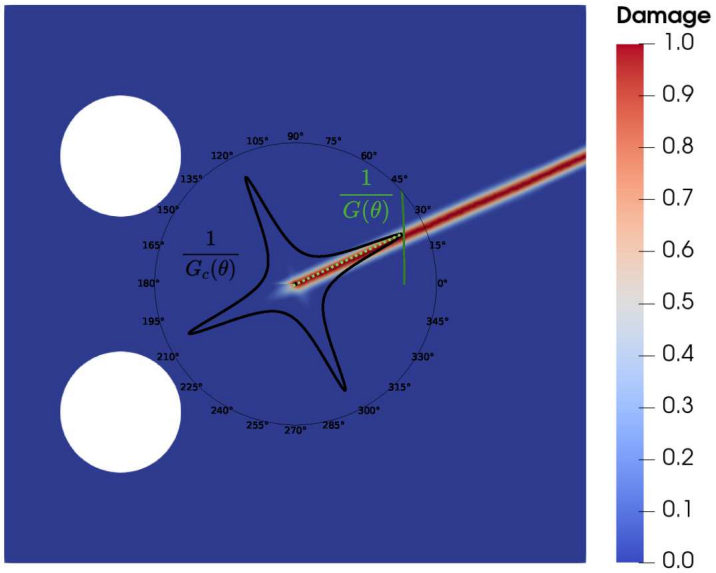

Figure 4.15 A snapshot of predicted numerical crack path in CT specimen with anisotropic fracture energy. The form of the anisotropic surface energy is expressed as: $G_c(\theta) = G_c \sqrt[4]{100 - 99\cos 4\left(\theta - \frac{5\pi}{36}\right)}$. The black and green curves represent the reciprocal surface energy and reciprocal energy release rate in polar coordinates respectively. The regularization parameter $\ell = 0.6$ mm is used in this numerical calculation.

With the identified regularization parameter $\ell_0 = 0.6$ mm, a numerical simulation was conducted on a CT sample with 25° raster angle. The comparison between the numerically predicted and experimental Force/COD is depicted in fig. 4.16. COD is defined as the difference in the y-axis displacement between two points situated on the crack lip away from the crack tip (aligned with the center of the pin hole), as shown in fig. 4.11. The experimental COD was determined using the displacement field measured through DIC. It is observed that the predicted numerical F-COD curve matches well with the experimental curve before crack propagation. However, during the crack propagation stage, a sudden decrease in numerical force is observed. This abrupt drop can be attributed to the appearance of an additional crack kink of finite length, as evident from the damage field depicted in fig. 4.16. This phenomenon is independent of the time step and indicates unstable propagation. Similar results and discussions were reported and discussed in Li and Maurini 2019. The kink problem has also been analyzed theoretically in Chambolle et al. 2009. The analysis in Chambolle et al. 2009 states that the jump is anticipated when a crack kinks because it exists another energy favorable direction for the crack propagation. In such a situation, the crack arrests before kinking. As the loading increases, a sudden jump is anticipated when a crack kink occurs, as the energy release rate G exceeds the critical surface energy G_c for the kinking direction. In contrast,

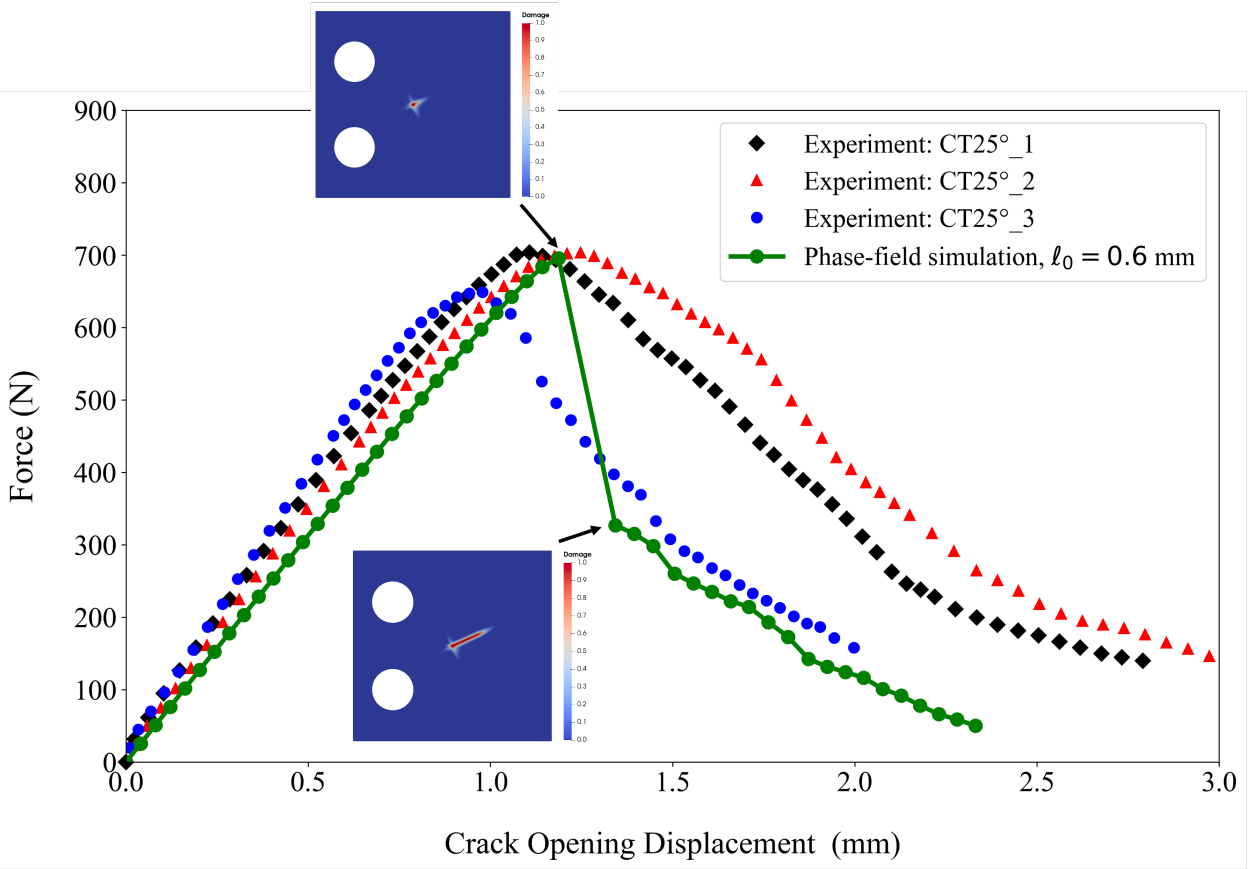

Figure 4.16 Comparison between numerical simulation and experiment on CT sample of 25° raster angle: Force versus COD. Two numerical damage field snapshots show the predicted crack path before and after the crack propagation, which is correlated with a sudden decrease in force.

our simulation corresponds to the case where $G = G_c$, indicating that the observed jump in our numerical experiments might be a numerical artifact resulting from the phase-field modeling.

The investigation of the mixed-mode fracture problem involved conducting numerical tests on CTS, using the same numerical parameters as for CT specimens. Different from the CT specimens, simulation of CTS specimens requires an additional numerical parameter: the loading angle. For the boundary condition, in order to determine the angle of the contact surface, the numerical K-ratio $\frac{K_{II}}{K_I}$ was computed for various pin angles and compared with experimental data, the same pin angle $\phi = 50°$ was obtained as CT sample.

A snapshot of the predicted numerical crack path in an anisotropic CTS sample with 15° loading angle is illustrated in fig. 4.17, with the regularization parameter $\ell_0 = 0.6$ mm. The black curve represents the corresponding reciprocal surface energy, and green

curve represents the reciprocal energy release rate in polar coordinate. When subjected to mixed-mode loading, the predicted crack path follows the material axis in the CTS sample, consistent with the GMERR predictions. Moreover, the predicted crack path consistently followed the direction of 'weak plane' as the loading angle and material axis changed during numerical experiments.

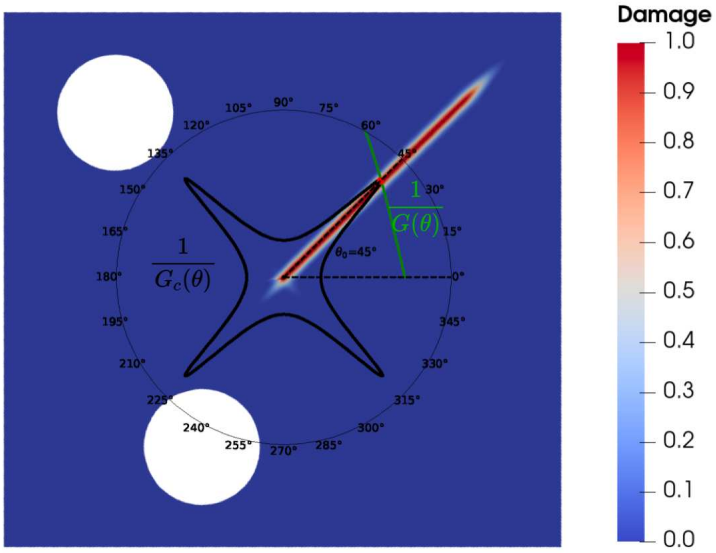

Figure 4.17 A snapshot of predicted numerical crack path in CTS specimen with anisotropic fracture energy. The loading angle is 15°. The form of the anisotropic surface energy is expressed as: $G_c(\theta) = G_c \sqrt[4]{100 - 99\cos 4\left(\theta - \frac{\pi}{4}\right)}$. The black and green curves represent the reciprocal surface energy and reciprocal energy release rate in polar coordinates respectively. The regularization parameter $\ell = 0.6$ mm is used in this numerical calculation.

To further examine the correlation between the critical force and the raster angle in CTS samples, we conducted numerical tests with a loading angle of 15° and varied the material axis θ_0 from 0° to 45°. The results of the critical force for CTS samples are presented in fig. 4.18. As mode II effects are present in CTS samples, it is important to consider the mode II SIF $\hat{K}^*_{II}$ while computing the energy release rate $\hat{G}(\theta)$ in eq. (1.21). Taking this into account, the modified theoretical prediction can be expressed as follows:

$$F_c(\theta) = \left[\frac{K_I^2 + K_{II}^2}{(K_I F_{11}(\theta) + K_{II} F_{12}(\theta))^2 + (K_I F_{21}(\theta) + K_{II} F_{22}(\theta))^2}\right]^{0.5} \cdot F_c(\theta = 0) \qquad (4.6)$$

To incorporate the K-ratio $\frac{K_{II}}{K_I}$ into the formulation, we utilized the average value of the K-ratio obtained from DIC experimental results of the CTS sample with a 15° loading angle and different raster angles at a displacement of 1 mm (prior to crack propagation).

It was observed that the K-ratio remains constant and independent of the raster angle, with a value of -0.12 for the CTS sample with a 15° loading angle (this value has been validated through numerical calculations). By considering the contribution of K_{II} in equation (4.6), we establish the relationship between the critical force and the difference between the raster angle and loading angle, as depicted in fig. 2.19. It is important to note that the critical force exhibits a non-monotonic variation with respect to the difference between the loading angle and raster angle. When the difference is zero, the crack propagates under pure mode I conditions, with the crack direction being orthogonal to the loading angle. These results highlight the ability of higher-order phase-field models to accurately predict quantitative outcomes for mixed-mode fracture problems involving strongly anisotropic surface energy. The optimal value of ℓ is founded to be 0.6 mm for two different sample geometry: CT and CTS, which indicate that the found regularization parameter is a material parameter which is independent on the sample geometry.

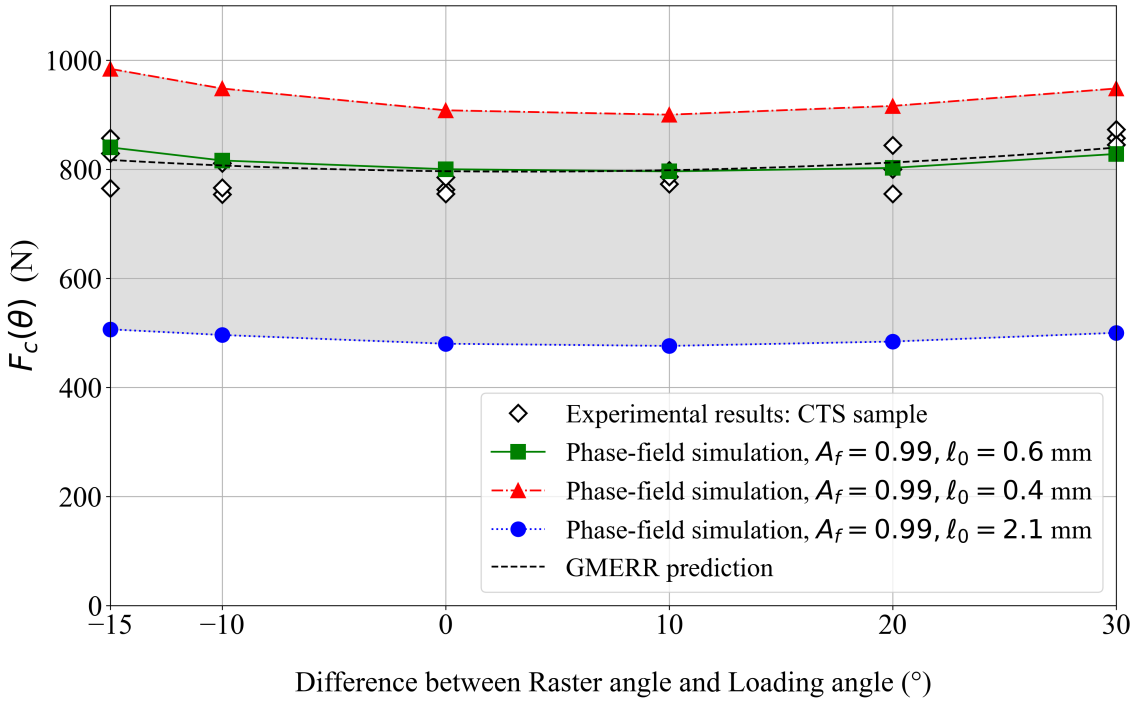

Figure 4.18 Comparison of experimental, numerical and theoretical critical forces as a function of the difference between raster angle and loading angle. Each experimental point correspond to 3 tested CTS samples. Blue, green and red dot-lines are predicted critical force obtained by phase-field simulation. Black dash-line are theoretical prediction based on the energy release rate criterion.

4.2.3 Discussion on the choice of the regularization parameter in anisotropic model

Through numerical investigations from the isotropic case to the weakly anisotropic case, we have observed that the regularization parameter, obtained using the expression presented in Tanné et al. 2018 , accurately predicts the crack path and critical load. Similar studies have been conducted in (Pham et al., 2017; Cavuoto et al., 2022) for the isotropic case, where they compared their results with experimental data. For the weakly anisotropic case, as studied in (Mesgarnejad et al., 2020), the computed regularization parameter was utilized to account for the T-stress effect in GMERR prediction, as the scale of the regularization parameter ℓ is similar to that of the fracture process zone. Their results using the KKL damage model in conjunction with with our numerical experiments using the AT1 model in Section 3.2.2, demonstrate that selecting $\ell = s$ in GMERR yields satisfactory predictions when compared to experimental data and phase-field simulations.

The aforementioned studies attempts to assign a physical interpretation to this numerical parameter ℓ, which is commonly referred to as the material internal length. Based on the determined optimal value of $\ell = 0.6$ mm for two different sample geometries: CT and CTS, it can be inferred that the obtained ℓ is a material parameter that remains consistent irrespective of the sample geometry. In light of the matter concerning the selection of this parameter ℓ, building upon the previous work, our study provides a new insight: in the case of materials with anisotropic surface energy, the presence of microstructure plays a role in contributing to this anisotropy. As a result, it is plausible that the numerical parameter ℓ depends on the size of the microstructure. The validity of this hypothesis is further supported by the comparison between our experimental results and simulations. Notably, we observed that the optimal value of $\ell = 0.6$ mm closely aligns with the diameter of the deposited thread (0.4 mm) in the FDM process. Since the ℓ is fixed, the Γ-convergence is no longer applicable for establishing a connection to the Griffith's model. However as mentioned in Marigo 2023, when dealing with structures where the length L greatly exceeds the internal length ℓ, we incorporate the small parameter ℓ/L into the damage evolution problem, this results in the reestablishment of the connection with Griffith's theory.

On the other hand, the inadequacy of the presented expression in (Tanné et al., 2018) in our numerical investigations can be attributed to two factors. Firstly, this formulation assumes the material to be isotropic and homogeneous under uniaxial tension, as noted in (Pham et al., 2011). However, the CT and CTS samples used in our study are not suitable for this case. Therefore, a more generalized formulation should be considered,

as suggested by (Molnár et al., 2020). Secondly, the expression is derived based on the second-order phase-field model, and extending it to the fourth-order phase-field model requires a rigorous mathematical proof. Additionally, the consideration of anisotropic surface energy becomes essential in this context.

While the debate regarding whether the regularization parameter can be interpreted as a material internal length is still ongoing, we find that based on previous studies and our own work, there are compelling reasons to consider the regularization parameter as an internal length due to the fact that the regularization parameter is connected to the critical load at which structural failure occurs. However, additional experimental verification is required, specifically employing diverse damage models, to validate the interpretation of the regularization parameter as an internal length.

4.3 Conclusions

In conclusion, we conducted a comparison between the numerical results obtained through the classical approach and the SIFs measured using DIC. This comparison serves to validate the experimental measurements and the assumption of isotropic elasticity adopted in our printed sample. Additionally, the FE model was used to determine the elastic constants, such as Young's modulus, of the printed CT sample.

Regarding the damage evolution problem, we successfully validated the phase-field model with a strongly anisotropic surface energy in predicting crack paths and the corresponding critical load using an appropriate regularization parameter. We thoroughly discussed the determination of suitable anisotropic constants for our printed sample. Furthermore, we established the relationship between the critical load and raster angle using the GMERR criterion within the framework of LEFM. Lastly, we examined the selection of the regularization parameter for the phase-field model and its significance.

In the next section, we will present a preliminary study using a strongly anisotropic phase-field model. This study includes an investigation into the possibility of zig-zag crack paths and the influence of $\boldsymbol{T}$-stress on materials with strongly anisotropic surface energy. Additionally, we will showcase an intriguing experimental observation of distinct fracture behaviors under cyclic loading.

Chapter 5

Preliminary study on samples with strongly anisotropic surface energy

In this chapter, we examine possibility zig-zag crack patterns in printed samples resulting from anisotropic surface energy. To investigate this phenomenon in diverse sample geometries, we employ the same higher-order phase-field model incorporating anisotropic surface energy presented in Chapter 4. Specifically, we study the influence of T-stress on the zig-zag crack path. Furthermore, we observe zig-zag crack propagation near the interface of a sample with thickness variation from experiments. These experimental findings align with the numerical results obtained using phase-field model. Through these analyses, we demonstrate the predictive capability of the higher-order phase-field model in capturing complex zig-zag crack patterns.

Additionally, we observe some interesting fracture behavior in printed samples when subjected to cyclic loading. This behavior significantly differs from the response observed under monotonic loading. To shed light on this phenomenon, we present preliminary results from numerical simulations using a phase-field model.

Contents

5.1 On the possibility of zig-zag crack path

Zig-zag crack pattern is an interesting phenomenon resulting from the presence of anisotropic surface energy, causing the crack to change its direction when encountering another energy favorable direction. The study of zig-zag crack growth holds significant importance for engineering applications, as reported in (Xu et al., 2021) that the zig-zag crack growth path can potentially decelerate the rate of fatigue crack propagation in certain materials. Besides, the complexity of zig-zag pattern can help us gain a deeper understanding of how cracks propagate in solids. This behavior can be observed in printed samples with a criss-cross printing pattern, where two 'weak planes' exist. To potentially observe the zig-zag crack pattern, appropriate sample geometry and loading conditions are required.

It has been observed possible zig-zag crack paths in anisotropic phase-field models (Li et al., 2015; Mandal et al., 2022) using a specific boundary condition called 'Surfing boundary condition' (Hossain et al., 2014; Brach et al., 2019a). However, this boundary condition necessitates a complex experimental setup that might be challenging to implement. An alternative method involves a short sample with protected upper and lower edges. When the crack reaches these boundaries, it changes direction and propagates along another energy favorable path. Another option is to create a groove in a CT sample, with thickness mismatch, it can therefore induce the zig-zag crack path. These alternative approaches offer potential avenues for observing the zig-zag crack pattern without any complicated experimental setups.

This section aims to present the findings of our study on the zig-zag crack path. We will start by presenting both numerical results and preliminary experimental results obtained from short samples presented in Chapter 3. Subsequently, we explored an alternative geometry configuration using CT samples with groove (sample with varying thickness). The primary objective of this study is to systematically explore a specific configuration capable of generating a zig-zag path in fracture experiments. To achieve this, we employed phase-field modeling. Once we identified the sample configuration, it will serve as a system for further investigation into the phenomena of zig-zag propagation.

5.1.1 Short sample: influence of T-stress on zig-zag crack path

The selection of the short sample employed in Mesgarnejad et al. (2020) was primarily motivated by the work of Nguyen et al. 2017. They conducted numerical experiments using the multi-damage model (as outlined in Section 1.4.3.3) on a sample that resembled the short sample used in our study. The observation of zig-zag crack path in their numerical results justified the adoption of the short sample for further investigation.

Another reason for choosing the short sample was related to its negative T-stress state. This caused the reciprocal energy release rate $\frac{1}{G(\theta)}$ to become non-convex in the Wulff diagram, as illustrated in the previous fig. 3.18. This intriguing behavior made it interesting to investigate the impact of T-stress in a system with strongly anisotropic surface energy. This is because there is a possibility that the non-convex reciprocal energy release rate may intersect the 'forbidden direction' of the surface energy as the loading increases.

5.1.1.1 Numerical experiments

We conducted the numerical experiments on the short sample using the same numerical parameters (A_f=0.99, ℓ=0.6 mm) as determined in Section 4.2. To provide a reminder, the dimensions of the short sample were as follows: $\frac{a}{L} = 0.5$ and $\frac{h}{L} = 0.28$, where a is the length of the notch, h is the height of the sample, and L is the length of the sample, as depicted in fig. 5.1 (left). The boundary condition adopted was as described in section 3.2.2. In Fig. 5.1, the numerical results are presented with the material axis θ_0=25° and the corresponding surface energy $\mathcal{E}_s$. Initially, the crack was observed to propagate along the direction of 25°. However, due to the constraint that the upper boundary cannot be damaged, the crack path turned to -75° once it reached the upper boundary. As a result, the crack then continued to propagate along this new energy-favorable direction, changing its trajectory until it ultimately reached the lower boundary of the sample. Each change in crack direction is linked to a jump of the surface energy. The jump length, denoted as s_i, can be calculated as $\mathcal{E}_s/G_0$. It's important to note that the length of the crack kink remains independent of the selection of the regularization parameter ℓ.

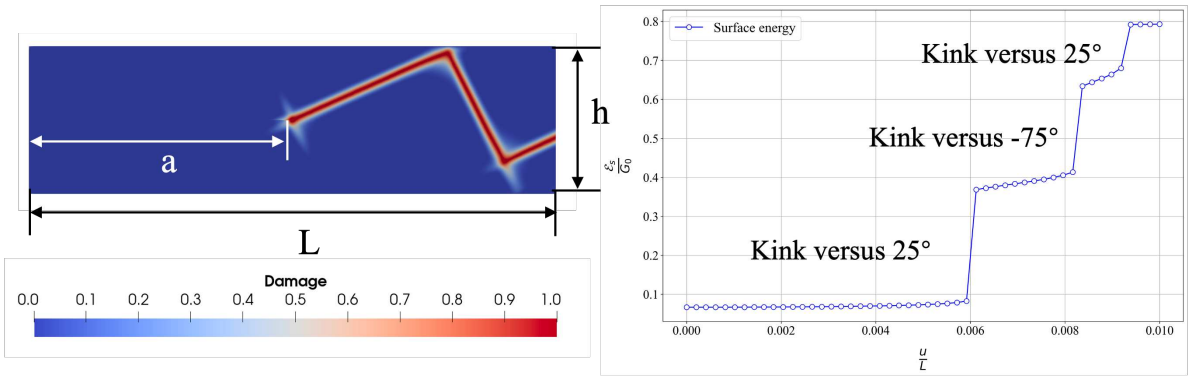

Figure 5.1 Left: A snapshot of predicted numerical crack path in short specimen with anisotropic fracture energy. The form of the anisotropic surface energy is expressed as: $G_c(\theta) = G_c \sqrt[4]{100 - 99\cos 4\left(\theta - \frac{5\pi}{36}\right)}$. The regularization parameter $\ell = 0.6$ mm is used in this numerical calculation. Right: corresponding surface energy.

Based on the investigation in Section 3.2.2, it was revealed that the influence of T-stress becomes negligible in cases of high anisotropy. Consequently, there is no need to delve into the effect of T-stress with a chosen anisotropic coefficient of $A_f = 0.99$. To address this, we conducted numerical experiments, varying the anisotropic coefficient A_f while keeping the material axis fixed at $\theta_0 = 45°$. Following the approach of (Mesgarnejad et al., 2020), we opted for $s = \ell = 0.6$ mm to account for the T-stress effect. The energy release rate $G(\theta)$ was then computed using equation (3.8).

In Fig. 5.2, we present the numerical predictions of crack angles concerning the anisotropic coefficient A_f and compare them to the GMERR predictions with and without considering the T-stress effect. Notably, the GMERR predictions that take into account the T-stress effect show greater consistency with the simulation results obtained from the phase-field model.

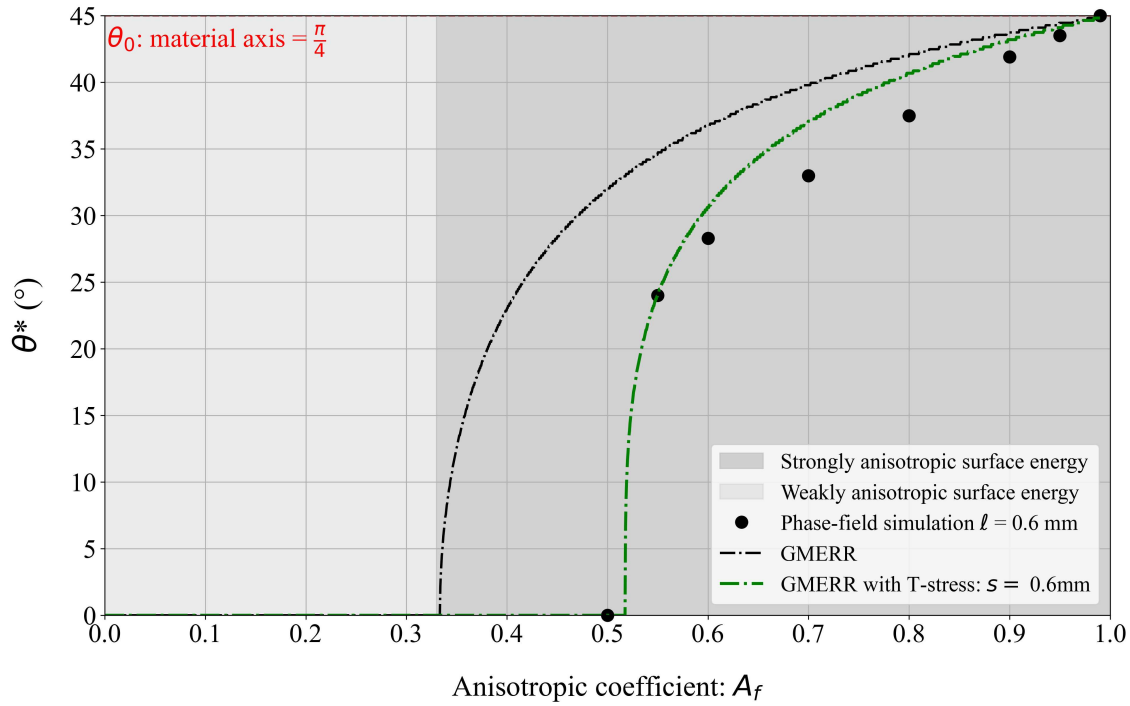

Figure 5.2 Comparison between numerical results with choice of ℓ=0.6 mm and GMERR prediction for short sample at fixed material axis θ_0=45° with different anisotropic coefficient. The black-dot line represents the GMERR predictions without considering the T-stress, while the green curve represents the predictions that take into account the T-stress effect.

Furthermore, according to the definition of convexity described by eq. (1.24), the four-fold surface energy exhibits a strong anisotropy when $A_f \geq 0.5$. Focusing on the numerical results with A_f=0.5, it is notable that the predicted crack angle is equal to 0°, a direction commonly referred to as the 'forbidden direction.' This finding imply the possibility of guiding crack propagation into the 'forbidden direction' by reducing anisotropy in our printed samples. However, achieving such a reduction in anisotropy through modifications in the printing process poses significant challenges, primarily because quantifying the anisotropic coefficient in printed samples is difficult. In Fig. 5.3, we depict the damage field of the short sample with varying anisotropic coefficient A_f. As the anisotropic coefficient decreases, it becomes evident that the predicted crack angle gradually approaches 0° until A_f=0.5, primarily due to the influence of the T-stress effect. Additionally, an intriguing observation is that the amplitude of the zig-zag crack path decreases as the A_f is reduced.

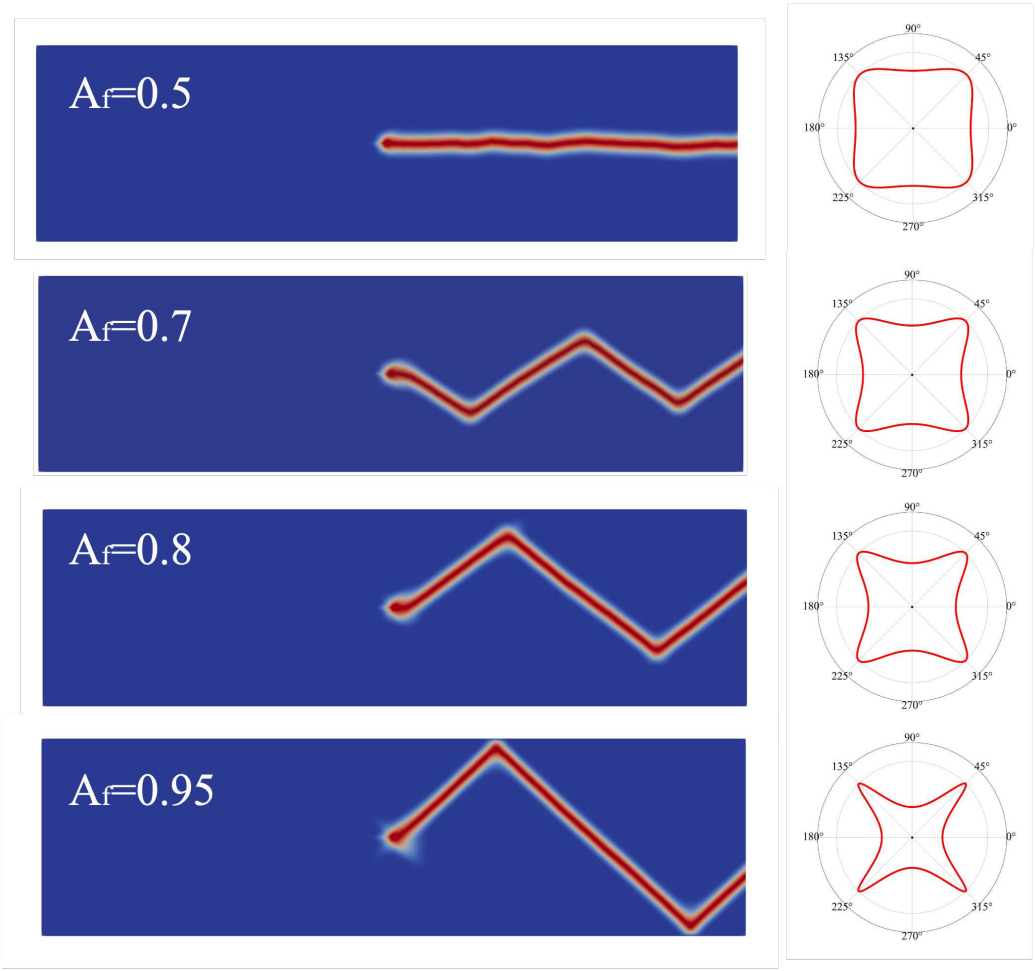

Figure 5.3 Snapshot of predicted numerical crack path in short specimen with different anisotropic coefficient A_f. In right shows the corresponding surface energy form.

We subsequently conducted numerical experiments, maintaining the anisotropic coefficient at a constant value of $A_f = 0.5$ and varying the material axis θ_0 within the range of $[0°, 45°]$. In Fig. 5.4, the black and green curves represent the GMERR predictions without and with the consideration of T-stress, respectively, while the black dots represent the numerically predicted angles corresponding to the material axis θ_0. Combining these results with the previous comparisons, we can draw the conclusion that accounting for the effect of T-stress becomes crucial when the system is not highly anisotropic. Additionally, it is worth noting that the choice of $s = \ell$ in eq. (3.8) yields satisfactory predictions using the GMERR criteria when compared to phase-field simulations.

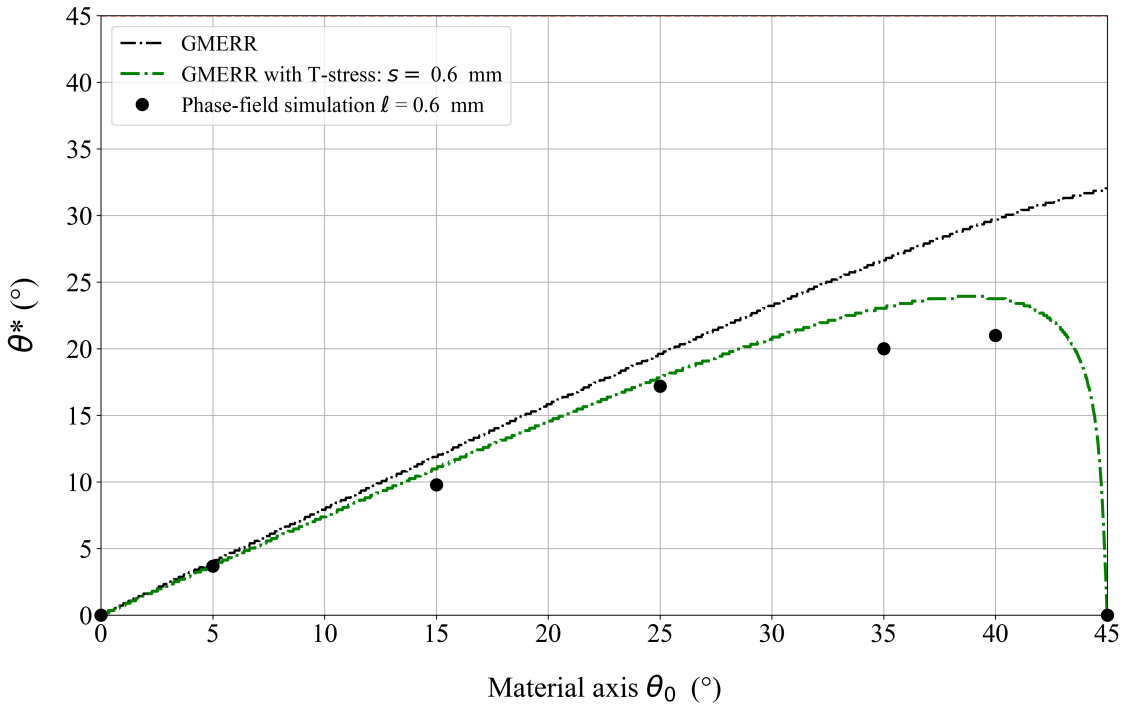

Figure 5.4 Comparison between numerical results with choice of ℓ=0.6 mm and GMERR prediction for short sample at fixed anisotropic coefficient A_f=0.5 with different material axis θ_0. With the black-dot line are the GEMRR prediction without T-stress, and green curve is the one take into account the T-stress.

5.1.1.2 Preliminary fracture experiments

Based on the sample geometry, we fabricated the short sample using the CAD model shown in fig. 5.5 (A). The sample has a thickness of 2.4 mm, comprising 16 layers. The upper and lower part was fixed in the grip as shown in fig. 5.5 (B) with 6 screw. During the experiments, a displacement was applied to the upper part along the y-axis, while the lower part remained fixed. We maintained a load rate of 0.5 mm/min, consistent with the one used for the CT sample.

In Fig. 5.5 (C), we present the experimental results for the sample with a 45° raster angle. We observed that the crack propagated along the weak plane until it reached the upper boundary. Interestingly, sometimes the crack propagated into the interface between the sample and the upper part instead of changing its direction to -45°. In some samples, we did observe an unstable crack propagation along -45°, which eventually formed a zig-zag crack path. Beside we have tried to increase the dimension of short sample with L = 50 mm. However, obtaining the zig-zag crack path systematically proved challenging in our fracture experiments. Most of the cracks ended with unstable

propagation along the interface between the sample and upper part. Due to the difficulty of realizing the boundary conditions applied to the short sample in experiments, we adopted an alternative concept by creating a thickness variation in the CT sample to reproduce the indestructible boundary condition in our numerical simulation.

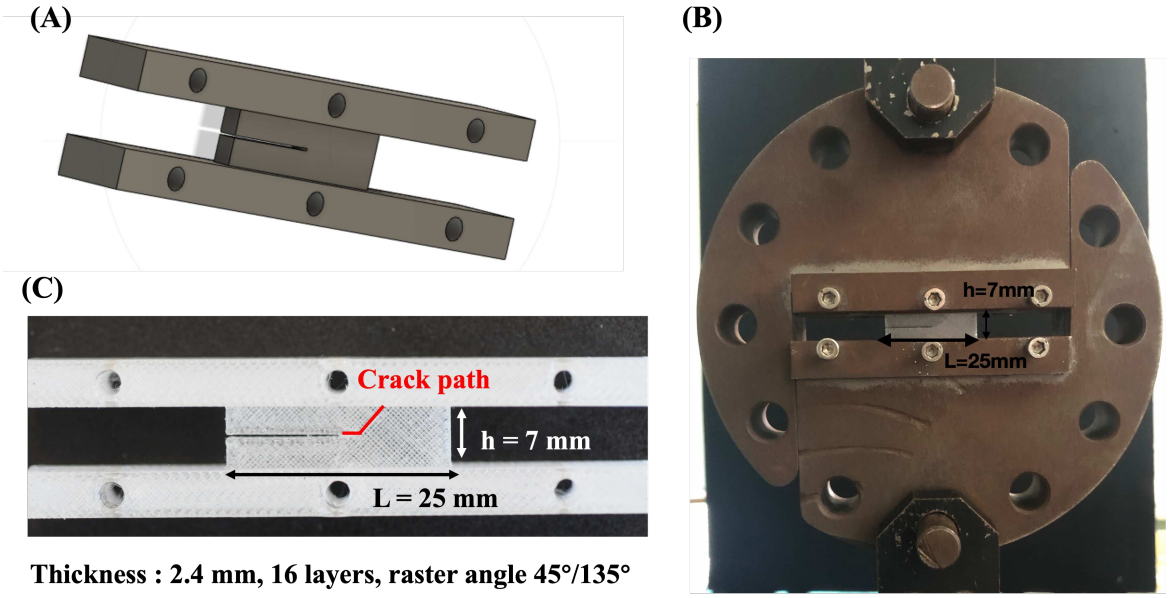

Figure 5.5 Fracture experiments on short sample: A) visualization of short sample in CAD software Fusion 360, B) experimental setup and C) experimental results for short sample with 45° raster angle

5.1.2 Zig-zag crack propagation in CT with variation in thickness

In the alternative sample configuration using a CT sample with a 25° raster angle and varying thickness, the experimental results (Fig. 5.6 (A) revealed an interesting crack propagation behavior. The middle of the CT sample was excavated to create a groove, and the crack was observed to propagate along the 25° direction initially. However, when the crack encountered a zone with a thickness mismatch, it formed a zig-zag path. Notably, the zig-zag crack path was observed to be in close proximity to the upper boundary, with a small amplitude, rather than zig-zag throughout the entire middle zone, these experimental results were consistently reproducible. To numerically simulate this behavior, the mismatch of thickness was represented by two indestructible boundaries in the 2D phase-field model. A regularization parameter was set to a minimum value (ℓ = 0.36 mm) to accurately capture the experimental zig-zag path. We opted for a

different value of ℓ deviating from the optimal value of 0.6 mm determined in previous section, with the intention of reducing the width of the damage field. This modification was made in consideration of relatively small height of the experimental zig-zag crack pattern shown in fig. 5.6 (A). As depicted in fig. 5.6 (B), the numerical simulation successfully replicated the experimental observed zig-zag crack path near the upper boundary.

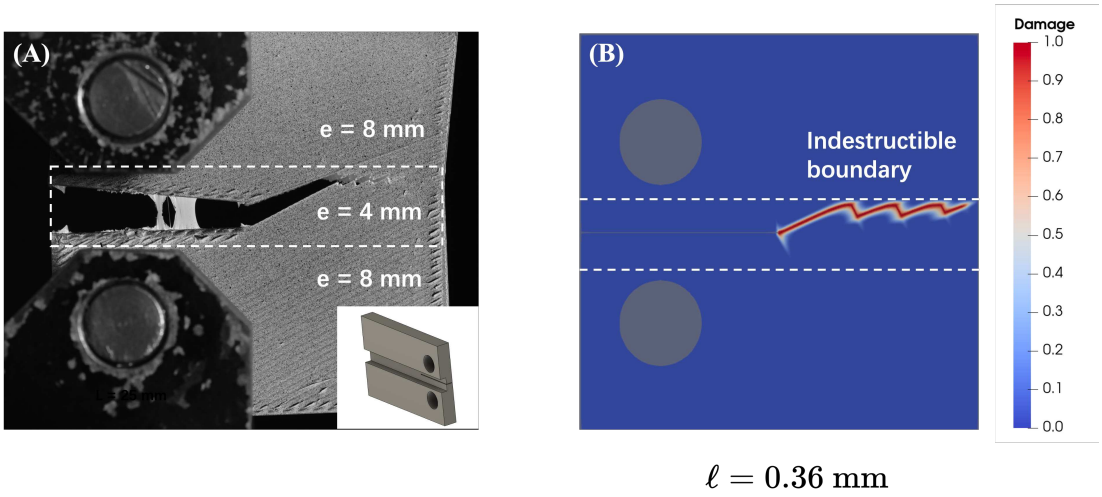

Figure 5.6 Zig-zag crack path in CT sample with varying thickness: (A) fracture experiments, where the middle zone featured a groove and was half as thick as the other parts of the sample. (B) snapshot of the damage field of the CT sample revealed that the upper and lower boundaries were assigned boundary conditions that prevented them from being damaged.

Nonetheless, employing a 2D model to simulate a 3D sample is unsuitable due to the discrepancy in thickness. It is noticed that the 3D effect near the interface boundary can not be produced in a 2D simulation. To gain deeper insights into the situation, we rewrite the energy functional eq. (1.42) using non-dimensional quantities as follows:

$$\widetilde{\mathbb{A}} = \frac{\mathbb{A}}{E_0},\ \tilde{\boldsymbol{\varepsilon}}(\tilde{\boldsymbol{u}}) = \frac{u_0}{L_0}\boldsymbol{\varepsilon}(\boldsymbol{u}),\ \widetilde{G}_{\mathrm{c}} = \frac{G_{\mathrm{c}}}{G_0},\ \tilde{\boldsymbol{u}} = \frac{\boldsymbol{u}}{u_0},\ \widetilde{\ell} = \frac{\ell}{L_0},\ \nabla^2\tilde{\alpha} = \frac{1}{L_0}\nabla^2\alpha,\ \mathrm{d}\widetilde{\Omega} = \frac{\mathrm{d}\Omega}{L_0^3} \tag{5.1}$$

The 3D problem is visualised in fig. 5.7: we designate the middle zone as Ω_1 with a thickness of e_1, and the remaining part as Ω_2 with a thickness e_2.

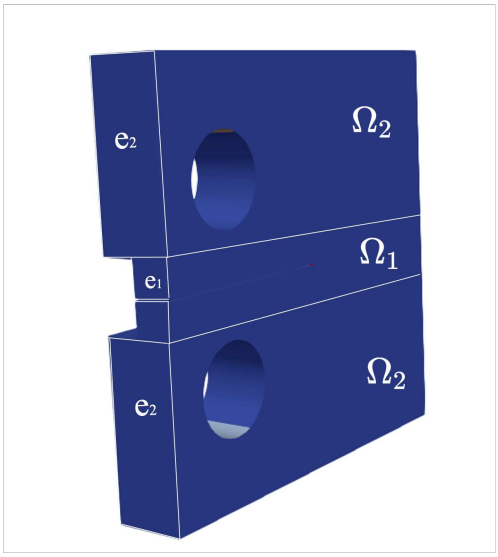

Figure 5.7 CT sample with a groove

The dimensionless energy functional of the 3D problem is denoted as follows:

$$\int_{\Omega_1} a(\tilde{\alpha}) W(\tilde{\boldsymbol{u}}) \mathrm{d}\tilde{\Omega}_1 + \int_{\Omega_2} W(\tilde{\boldsymbol{u}}) \mathrm{d}\tilde{\Omega}_2 + \frac{G_0 L^2}{E_0 u_0^2} \int_{\Omega_1} \frac{w(\tilde{\alpha})}{\tilde{\ell}_0} + \tilde{\ell}_0^3 \mathbb{C} \nabla^2 \tilde{\alpha} \cdot \nabla^2 \tilde{\alpha} \, \mathrm{d}\tilde{\Omega}_1 \tag{5.2}$$

Here, we denote ω_i as a 2D body, and its relation with the corresponding 3D body is given by $\Omega_i = e_i \cdot \omega_i$, where e_i represents the corresponding thickness. To extend a 2D problem into 3D, two assumptions are made:

1. **Crack from 2D to 3D**: $\Gamma(x) = \Gamma'(x') \cdot e_i(x_3)$ with $x = (x_1, x_2, x_3) \in \mathbb{R}^3$ and $x' = (x_1, x_2) \in \mathbb{R}^2$
2. **Displacement from 2D to 3D**: $\boldsymbol{u}(x) = \boldsymbol{u}'(x') \cdot e_i(x_3)$

The eq. (5.2) is therefore can be reformulated as follows:

$$\int_{\omega_1} a(\tilde{\alpha}) W(\tilde{\boldsymbol{u}}) \mathrm{d}\tilde{\omega}_1 + \frac{e_2}{e_1} \int_{\omega_2} W(\tilde{\boldsymbol{u}}) \mathrm{d}\tilde{\omega}_2 + \frac{G_0 L^2}{E_0 u_0^2} \int_{\omega_1} \frac{w(\tilde{\alpha})}{\tilde{\ell}_0} + \tilde{\ell}_0^3 \mathbb{C} \nabla^2 \tilde{\alpha} \cdot \nabla^2 \tilde{\alpha} \, \mathrm{d}\tilde{\omega}_1 \tag{5.3}$$

It was initially thought that the 3D problem could be effectively replaced with a simpler 2D model by assuming an elastic modulus $E_2 = \frac{e_2}{e_1} E_1$ for domain Ω_2 in numerical simulations, given that the ratio of thicknesses $\frac{e_2}{e_1}$ is 2. However, this assumption turned out to be incorrect due to the second assumption not holding at the interface, resulting in a significant 3D effect at that boundary. Consequently, the solution of the 2D displacement

field cannot be directly extended to 3D by merely multiplying it by the thickness. As a result, a 3D model becomes necessary to accurately simulate our CT sample with the groove. Unfortunately, the current computational power is insufficient to handle a 3D model with anisotropic surface energy.

5.1.3 Perspectives

In conclusion, the previously proposed sample configurations have proven to be defective, either due to experimental irreproducibility or the mismatch between numerical simulations and experimental reality. Consequently, both sample types introduced earlier are unsuitable for studying the phenomena of zig-zag crack propagation experimentally.

However, during our experimental investigation, we stumbled upon another type of CT sample that shows promise. By altering the printing method, we created successive layers that were not arranged orthogonally, instead, they formed an angle of less than 90 degrees. Fig. 5.8 presents this CT sample with a ± 15° raster angle, wherein we observed a pronounced zig-zag crack path oscillating between 15° and -15°. Although it can be recognized as a potential sample configuration to investigate the zig-zag crack propagation, it still requires further development of the numerical model with conform surface energy correspond to the arrangement of the threads.

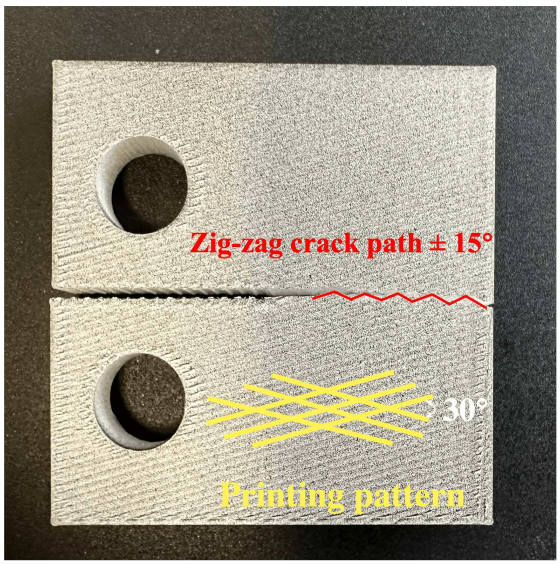

Figure 5.8 Zig-zag crack path in CT sample with successive layers arranged with an angle of 30°, red lines shows the zig-zag crack path along ± 15°.

5.2 Fatigue versus quasi-statics loading

One potential application of constructing an anisotropic surface energy is to gain control over the crack path, thereby ensuring the safety and reliability of components during their service life. In real-world scenarios, many components experience cyclic loading instead of monotonic loading. Therefore, understanding fracture behavior under cyclic loading, particularly the crack path, becomes crucial for ensuring the structural integrity of these components.

To our best knowledge, it is generally assumed that the crack propagation direction can be predicted in the same way for both quasi-static and fatigue propagation (Chen et al., 2015). However, this assumption lacks solid physical arguments and has not been proven to be valid, even for isotropic materials.

In our research, during the mode I pre-crack cyclic loading process, we observed even when the infill angle differs from 0°, we consistently obtained a straight pre-crack instead of propagation along the direction of the 'weak plane.' This discovery raised questions about the validity of the aforementioned assumption. To delve further into this phenomenon, we conducted fatigue tests using the samples which were used in fracture experiments presented in Chapter 2 to investigate the crack path under cyclic loading.

5.2.1 Experiments under cyclic loading

The fatigue experiments involved using both CT samples with a raster angle of 30° and CTS samples with a 45° raster angle and 15° loading angle. The samples were mounted in an Instron ElectroPuls E3000 testing machine, where pins were inserted into the holes, and the bottom was fixed securely. A sinusoidal cyclic force, ranging between 100 N (Fmin) and 220 N (Fmax), was applied to the samples at a frequency of 3 Hz. At the start of each cycle during the fatigue tests, we set a displacement threshold. When the measured displacement reached this threshold, indicating the completion of the load cycle, the test was momentarily paused, and an image was captured, with the maximum force set at Fmax = 220 N. The specimens underwent approximately $1.0\text{x}10^5$ to $1.5\text{x}10^5$ loading cycles, and about 20 images were captured during each experiment. The different crack propagation paths can be observed in fig. 5.9. For monotonic load, the crack followed the direction of infill angle, namely the 'weak plane', while for cyclic loading, the crack advances progressively in step with the cycle. For CT sample, the crack is observed to advance straight, and for CTS sample, it kinks but in a different direction than under monotonic load, the new direction is almost perpendicular to the direction of loading angle. The experimental results are reproducible with different raster angle.

Therefore, it can be concluded that, under cyclic loading, the crack path deviated from the direction of the printing threads.

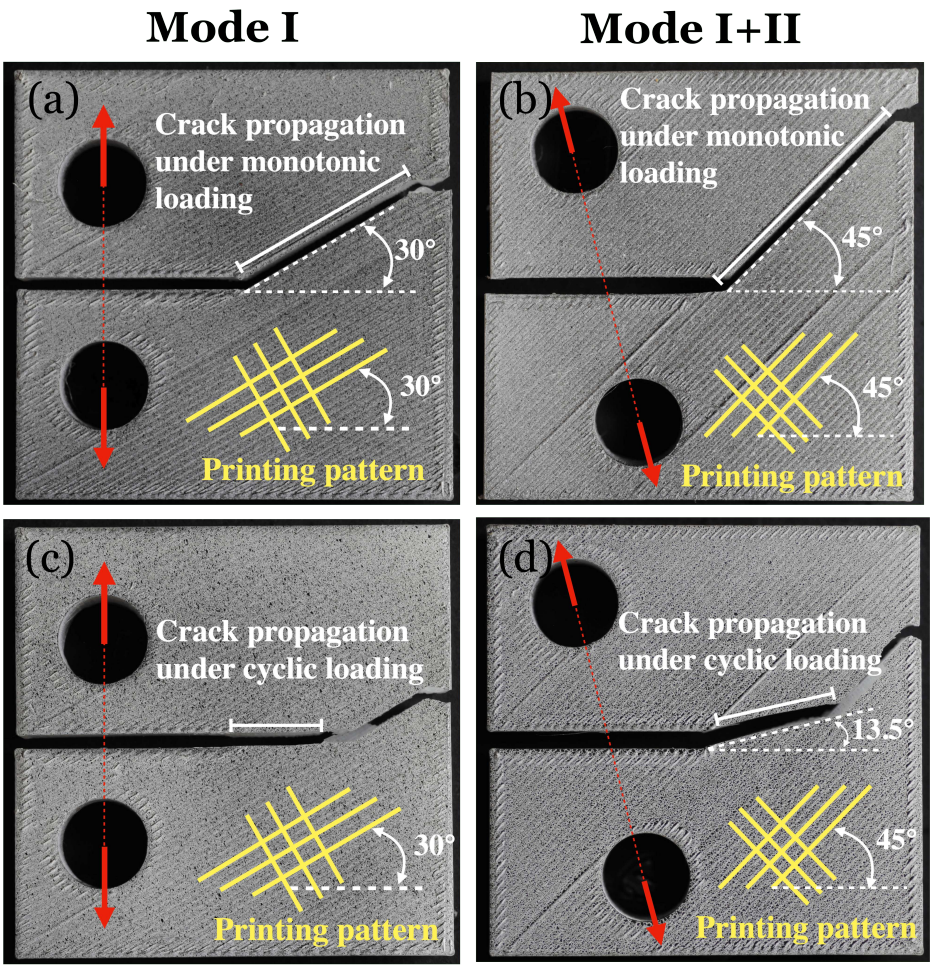

Figure 5.9 Different crack propagation path depending on the loading mode: first row (a, b) CT and CTS (loading angle 15°) sample under monotonic loading. second row (c, d) CT and CTS (loading angle 15°) sample under cyclic loading. Two different column represent two different loading mode.

To gain a deeper insight into the difference in crack paths under monotonic loading and cyclic loading, we conducted a comparison of the evolution of SIFs during crack propagation, as depicted in fig. 5.10. When subjected to monotonic load, the crack changed its direction, and a sudden increase in the SIF value was observed at the onset of propagation. This deviation from the expected behavior indicates that the PLS criteria as presented in Section 1.2.1.6 is not valid, since $K_{II} \neq 0$ during crack propagation. However, our previous findings indicated that the crack direction can be accurately predicted using the GMERR criterion, which involves adopting a non-convex form of the surface energy

$G_c(\theta)$.

In contrast, when examining fatigue crack propagation (as shown in the second row of fig. 5.10), the crack path followed the rules of isotropic material, and the PLS was satisfied, as K_{II} remained zero during crack propagation. This suggests that the anisotropic fracture toughness did not significantly influence the crack path in the case of cyclic loading.

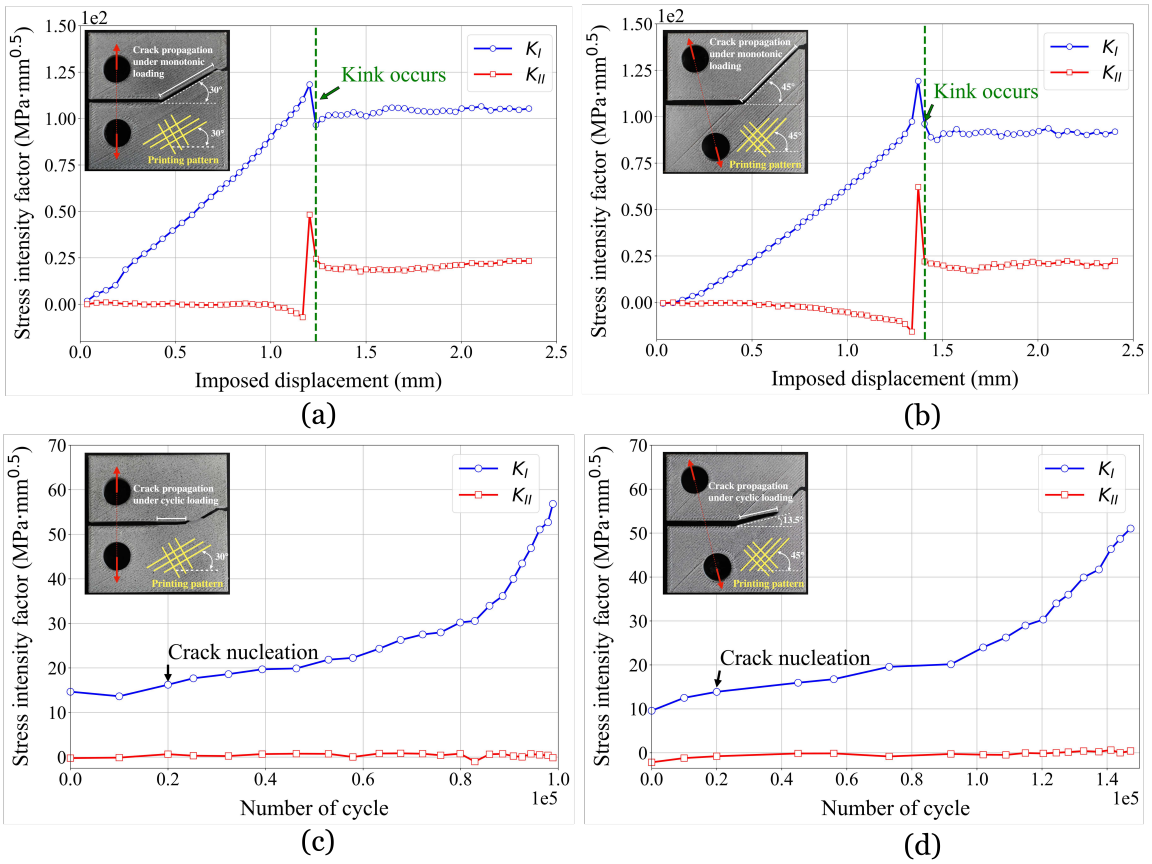

Figure 5.10 Evolution of SIFs measured by DIC: first row (a, b) CT and CTS sample under monotonic loading. second row (c, d) CT and CTS sample under cyclic loading. Two different column represent two different loading mode.

5.2.2 Numerical simulation: phase-field for fatigue fracture model with anisotropic surface energy

To computationally investigate the distinction between quasi-static and fatigue crack propagation paths in anisotropic media, the authors (cite our paper) conducted a study focusing on a mode I crack propagating into a direction of higher fracture toughness. The anisotropic model presented in (Mesgarnejad et al., 2020) was employed for this purpose.

To account for fatigue effects in the anisotropic model, the authors incorporated a recently developed phase-field model of fatigue (Mesgarnejad et al., 2019; Grossman-Ponemon et al., 2022). This novel approach allows the crack to grow below the Griffith threshold ($G < G_c$) by gradually degrading the fracture toughness. The energy function can be denoted as following:

$$\mathcal{E}_\ell[\boldsymbol{u},\alpha,\gamma](N) := \int_\Omega a(\alpha)W(\boldsymbol{u})\mathrm{d}\Omega + \frac{G_0}{4c_w\ell_0}\int_\Omega \gamma\left[w(\alpha)+\ell_0^2\underset{\sim}{\mathcal{A}}|\nabla\alpha|^2\right]\mathrm{d}\Omega - \int_{\partial_N\Omega}\boldsymbol{T}^d(N)\cdot\boldsymbol{u}\,\mathrm{d}s \tag{5.4}$$

where $\gamma(N,\boldsymbol{x})$ is the degradation function as a function of cycle number N and spatial position $\boldsymbol{x}$. For further details on the fatigue anisotropic phase-field model, we refer readers to (Mesgarnejad et al., 2020; Grossman-Ponemon et al., 2022).

Fig. 5.11 presents the outcomes of phase-field simulations, illustrating the different crack paths observed under two loading conditions. The first row represents monotonic loading, while the second row corresponds to cyclic loading. Moving from left to right, the anisotropic coefficient A increases. Under monotonic loading, as the anisotropic coefficient A rises and exceeds 3, the crack path gradually switches its direction towards the 'weak plane.' In contrast, when considering the fatigue model, the crack direction remains fixed at 0°, regardless of how the anisotropic coefficient evolves.

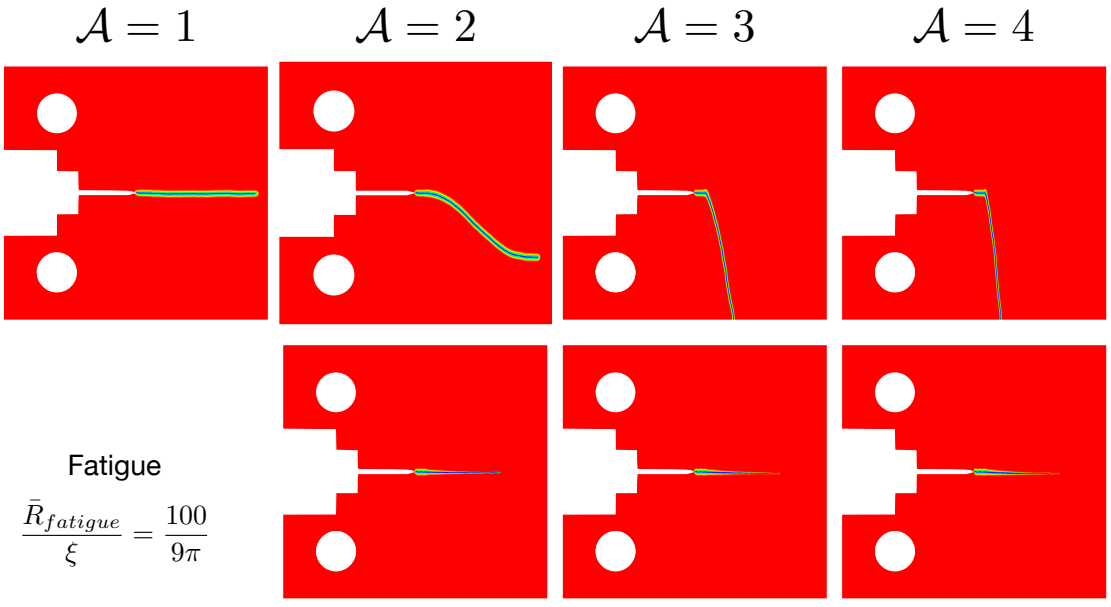

Figure 5.11 Numerical simulations: first row shows the case of monotonic loading, second row shows the case of cyclic loading, from left to right with the anisotropic coefficient A increases.

Both experimental and numerical results have consistently demonstrated a substantial disparity in crack paths between monotonic loading and cyclic loading conditions. Although the exact underlying reasons for this discrepancy are not yet fully clear, it is reasonable to consider the influence of the FPZ as a potential factor. As reported in a research on rocks has revealed that under cyclic loading, the FPZ length is approximately 60 % larger than that observed under monotonic loading (Le et al., 2014).

5.3 Conclusions

In this chapter, we carried out numerical experiments using the numerical parameters determined in Chapter 4. Our objective was to explore potential sample configurations for investigating zig-zag crack propagation. While the zig-zag crack path could be observed in numerical simulations, conducting corresponding fracture experiments presented significant challenges.

Another intriguing finding was the distinct fracture behavior exhibited by the printed samples under monotonic and cyclic loading. We observed this phenomenon in both experiments and numerical simulations. To understand the underlying reason for this difference, further investigation is necessary to provide a physical explanation.

Conclusion and Perspectives

Conclusion

This thesis explores crack propagation within printed samples that display isotropy in elasticity and anisotropy in fracture toughness. We used a combination of experimental, numerical, and theoretical approaches to examine the selection of crack paths in FDM-fabricated PC samples.

The experimental investigation is outlined in Chapter 2. By adopting the criss-cross printing pattern, the printed sample exhibits anisotropic fracture behavior. Following a pre-cracking procedure, we conduced fracture experiments under both Mode I and Mode I+II loading condition using CT and CTS samples. Through the examination of experimental findings, we deduced the existence of a prohibited direction in our printed sample, as evidenced by the consistent crack propagation along the printed direction. At a microscopic level, crack propagation occurs due to the fracture of the melt junction between two parallel adjacent threads. We used the DIC to determine the critical energy release rate G_c of the 'weak plane' by using the measured SIFs after crack kinking. Additionally, we noted that the printing direction also significantly influences the critical load associated with the fracture behavior.

To investigate anisotropic fracture behavior, we employed two numerical models based on the classical approach and variational approach. The numerical investigation comprises two main steps: which are outlined in Chapters 3 and 4. In Chapter 3, we focused on validating the numerical models, while Chapter 4 involves a comparison with experimental results. The numerical model based on the classic approach is implemented using Cast3M (2020). This model addresses the static elasticity problem and is employed to determine the SIFs after crack kinking. To establish its accuracy, we compared the numerical results with Amestoy-Leblond's formula, showcasing the model's capability in accurately determining SIFs after kinking. For the numerical model based on the variational approach, the numerical implementation was conducted using the open-source FEM software FEniCS (2019.1). This model is dedicated to solving the problem of

damage evolution. In the initial stages, we validated the implementation of the I-integral, which aids in segregating the SIFs K_I and K_{II} and determining the value of T-stress. Subsequently, we compared the predictions of the numerical crack path and the associated critical load with experimental data from relevant literature. This was done to validate the accuracy of the phase-field model. We started with isotropic and weakly anisotropic cases (second-order phase-field model), using the AT1 damage model. The results of the numerical predictions exhibited a good agreement with the provided experimental data. The validation of the AT1 phase-field model carries significant importance, as it serves as a smooth transition towards the higher-order phase-field model. In the theoretical aspects, we validated the prediction procedure of the GMERR by comparing the predicted crack path and critical stress with relevant experimental data.

In Chapter 4, we conducted a comprehensive comparison between the numerical outcomes and experimental data. This involved contrasting the calculated SIFs using the classical model with the SIF values obtained through DIC, aiming to validate the accuracy of experimental measurements. Furthermore, the numerical model founded on the classical approach was employed to derive the elastic constants of the printed sample by means of displacement field comparison.

Subsequently, we employed a higher-order phase-field model with strongly anisotropic surface energy to simulate crack propagation in our printed samples. We began by calibrating the numerical parameters and then proceeded to compare the anticipated crack path and relevant critical force with experimental results, revealing a notable degree of agreement between the two. Importantly, we demonstrated that these predictions can be effectively achieved through the application of the GMERR criteria within a LEFM framework. Additionally, informed by results of the numerical investigations, our exploration delved into a discussion concerning the selection of the regularization parameter ℓ in the context of the phase-field model. By conducting numerical experiments with different sample geometries (CT and CTS), we found that the regularization ℓ can be recognized as a material internal length which is close to the size of the printed thread.

In the final Chapter 5, we introduced a series of preliminary investigations aimed at identifying suitable sample configurations for observing zig-zag crack propagation. Furthermore, we made an intriguing discovery regarding the divergent fracture behaviors demonstrated by printed samples when subjected to both monotonic and cyclic loading conditions. To further elucidate this phenomenon, we employed a fatigue phase-field model featuring weakly anisotropic surface energy, successfully replicating the experimental results and enhancing our understanding of this intricate behavior.

Future work

Building upon the discoveries and conclusions presented in this thesis, certain aspects of the research are still in their preliminary stages. Consequently, in the subsequent discussion, we will outline a road-map for prospective investigations and future endeavors.

Zig-Zag crack path

Continuing in the vein of Chapter 5, we aim to explore conditions that could potentially induce zig-zag crack propagation. This objective can be accomplished through alterations to either the sample's geometry or the printing approach. On the experimental front, the modification of both sample geometry and printing strategies via 3D printing is readily attainable. However, the systematic observation of zig-zag crack propagation in fracture experiments necessitates further validation. The primary challenge in achieving this lies within the loading configuration. Despite its numerical observation in the phase-field model with a surfing boundary' condition, the practical realization of such a configuration in experimental settings is complex.

However, it has been observed that maintaining the current sample geometry while achieving a zig-zag crack path can be realized through modification in the printing strategy. Instead of constructing layers that are mutually orthogonal, we can achieve this by reducing the angle between two consecutive layers. From a numerical perspective, implementing such a modified printing pattern necessitates a corresponding adjustment to the form of the surface energy in the phase-field model. This adjustment transforms the cubic system into a orthorhombic system, leading to the introduction of nine anisotropic constants within the $\mathbb{C}$ matrix. Therefore, further research is necessary to investigate how adjusting anisotropic constants can transform surface energy into an orthorhombic system.

Measurement of anisotropic surface energy in the 'forbidden direction'

As outlined in this thesis, our assumption was that the surface energy form of the printed sample resembles that of a four-fold symmetric model, where the two infill angles correspond to the two weak planes'. While experimental observations indicate the presence of forbidden directions, determining the precise values of these forbidden directions' remains challenging, given that cracks cannot be guided into these directions.

According to the predictions derived from the GMERR criteria, the 'forbidden direction' can be experimentally determined through a specific loading configuration (yielding a negative T-stress) and by reducing the anisotropy of fracture toughness.

However, practically achieving a reduction in anisotropy through 3D printing is complex, and quantifying the degree of anisotropy into a specific numerical value poses difficulties. Moreover, if we were to reduce the anisotropy of the sample, the measured values of the 'forbidden directions' would no longer correspond to the sample studied within the scope of this thesis.

Therefore, drawing inspiration from fatigue testing, we recognize that under cyclic loading, the crack can readily be directed into the forbidden direction'. Interestingly, the surface energy generated in this process is indeed equivalent to the energy dissipated during fatigue testing. While measuring dissipated energy might pose challenges, this approach remains more viable than conducting traditional fracture experiments. Furthermore, the fatigue testing method offers another advantage: it enables us to access any direction of the surface energy pertaining to the printed sample by simply rotating the raster angle.

Fatigue phase-field model with four-fold symmetric surface energy

As detailed in Chapter 5, the experimental findings highlight a notable difference in crack paths under both monotonic and cyclic loading conditions. This phenomenon is also evident within the fatigue phase-field model with a weakly anisotropic model. However the numerical investigation incorporated with a weakly anisotropic surface energy, which doesn't fully align with the characteristics of the printed sample. Given the intricate nature of higher-order phase-field models incorporating strongly anisotropic surface energy, various numerical challenges, such as non-convergence of the nonlinear solver, can arise. Therefore, incorporating fatigue mechanisms within the strongly anisotropic phase-field model requires meticulous attention from a numerical point of view.

Furthermore, to gain a comprehensive understanding of the variance in crack paths between monotonic and cyclic loading, additional experimental investigation is imperative. One plausible explanation for the observed difference might arise from the variation in the size of the FPZ under these loading conditions. As a consequence, the propagation of cracks might not 'perceive' the anisotropy of fracture energy, leading to a different crack path.

Stability analysis by numerical simulation

The use of alternate minimization algorithm (Bourdin et al., 2008) in this study, which exclusively provides stationary points as solutions. As stated in (León Baldelli and Maurini, 2021), quasi-static evolution problems in fracture and the related softening damage models exhibit strong non-linearity, which can lead to the possibility of multiple solutions or no solutions at all. Hence, it becomes essential to perform numerical stability

and bifurcation analysis to identify the physically meaningful solution from multiple potential solutions.

In the work of León Baldelli and Maurini 2021, given a solution which satisfies the first-order condition shown in eq. (1.38), they checked the second-order local minimality conditions by detecting the sign of the eigenvalue to evaluate whether the returned solution is incrementally stable or not. For more details of definition of the second-order conditions refer to (León Baldelli and Maurini, 2021) and implementation in FEniCSx is available online [1].

Through the illustration of simple cases such as a 1D traction bar and a 2D thin film multifissuration problem, the study by León Baldelli and Maurini 2021 showcases the capability of their proposed algorithms identifying unstable evolution paths. In this context, we demonstrate the application of their code to a 2D problem involving a singularity. We use dimensionless pac-man sample and CT sample, as depicted in fig. 5.12. It's worth noting that our numerical experiments were conducted using an isotropic phase-field model. We suggest extending the stability analysis to include the anisotropic phase-field model in the future. As noted in Chambolle et al. 2009; Li and Maurini 2019, when the crack kinks, it will lead to a jump in both time and space, it would be beneficial to investigate whether the evolution becomes incrementally unstable during the crack kinking.

[1] https://github.com/kumiori/mec647

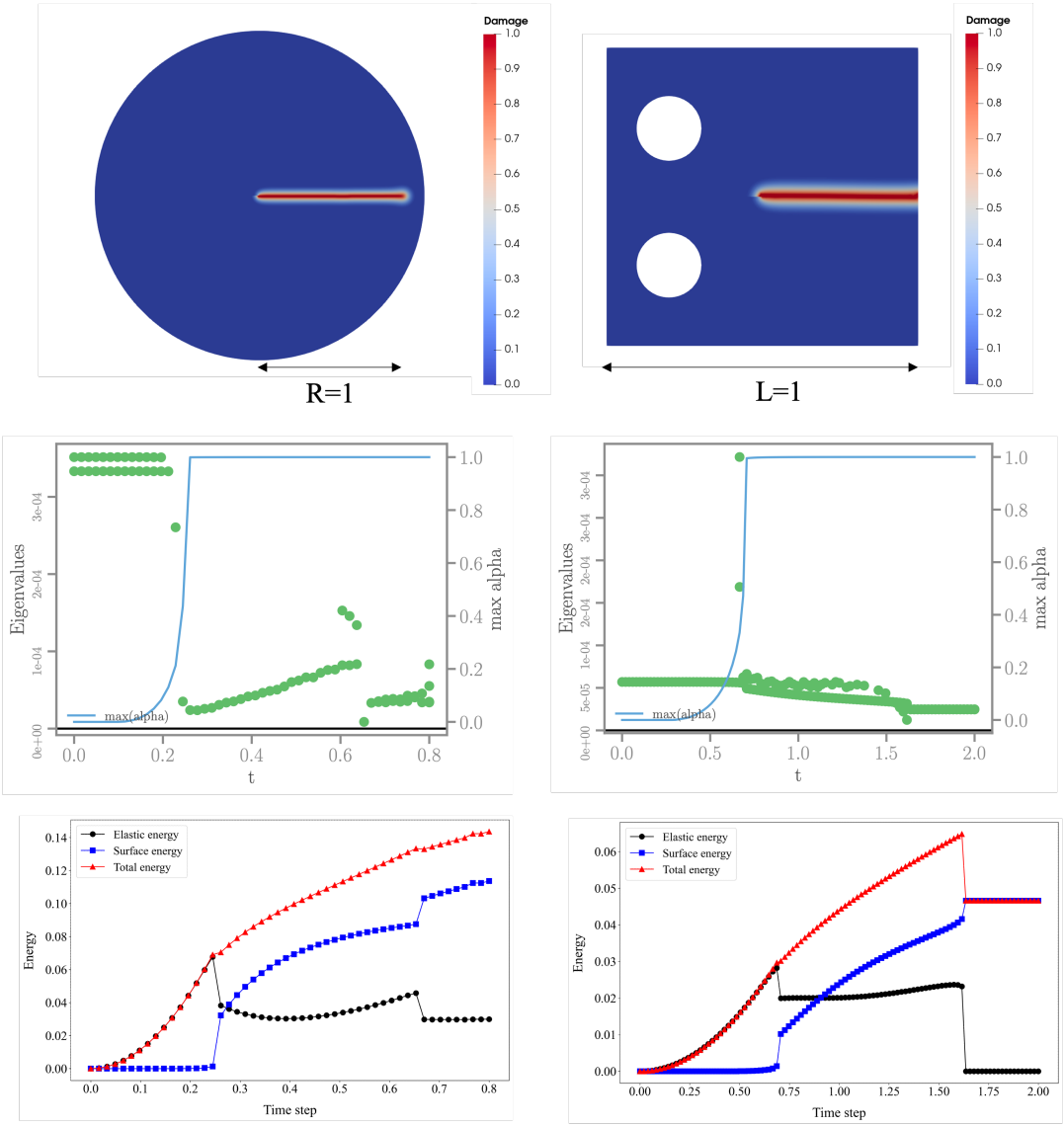

Figure 5.12 Application of stability analysis on pacman sample (left) and CT sample (right). First row shows the predicted crack path (in red), second row shows the computed eigenvalues with respect to time, and third row shows the plot of different energies with respect to time. (The mesh size used in numerical test: h = 0.01, and internal length $\ell = 0.03$)

Appendix A

The expression of Amestoy-Leblond's formula

The expression of Amestoy-Leblond's formula F_{pq} and G_p are denoted as follows (Amestoy and Leblond, 1992):

$$
\begin{aligned}
F_{11}(\varphi) =& 1 - \frac{3\pi^2}{8}\varphi^2 + \left(\pi^2 - \frac{5\pi^4}{128}\right)\varphi^4 + \left(\frac{\pi^2}{9} - \frac{11\pi^4}{72} + \frac{119\pi^6}{15360}\right)\varphi^6 + 5.07790\varphi^8 \\
& - 2.88312\varphi^{10} - 0.0925\varphi^{12} + 2.996\varphi^{14} - 4.059\varphi^{16} + 1.63\varphi^{18} + 4.1\varphi^{20} + o\left(\varphi^{22}\right) \\
F_{12}(\varphi) =& -\frac{3\pi}{2}\varphi + \left(\frac{10\pi}{3} + \frac{\pi^3}{16}\right)\varphi^3 + \left(-2\pi - \frac{133\pi^3}{180} + \frac{59\pi^5}{1280}\right)\varphi^5 + 12.313906\varphi^7 \\
& - 7.32433\varphi^9 + 1.5793\varphi^{11} + 4.0216\varphi^{13} - 6.915\varphi^{15} + 4.21\varphi^{17} + 4.56\varphi^{19} + o\left(\varphi^{21}\right) \\
F_{21}(\varphi) =& \frac{\pi}{2}\varphi - \left(\frac{4\pi}{3} + \frac{\pi^3}{48}\right)\varphi^3 + \left(-\frac{2\pi}{3} + \frac{13\pi^3}{30} - \frac{59\pi^5}{3840}\right)\varphi^5 - 6.176023\varphi^7 \\
& + 4.44112\varphi^9 - 1.5340\varphi^{11} - 2.0700\varphi^{13} + 4.684\varphi^{15} - 3.95\varphi^{17} - 1.32\varphi^{19} + o\left(\varphi^{21}\right) \\
F_{22}(\varphi) =& 1 - \left(4 + \frac{3\pi^2}{8}\right)\varphi^2 + \left(\frac{8}{3} + \frac{29\pi^2}{18} - \frac{5\pi^4}{128}\right)\varphi^4 \\
& + \left(-\frac{32}{15} - \frac{4\pi^2}{9} - \frac{1159\pi^4}{7200} + \frac{119\pi^6}{15360}\right)\varphi^6 + 10.58254\varphi^8 - 4.78511\varphi^{10} \\
& - 1.8804\varphi^{12} + 7.280\varphi^{14} - 7.591\varphi^{16} + 0.25\varphi^{18} + 12.5\varphi^{20} + o\left(\varphi^{22}\right);
\end{aligned}
\tag{A.1}
$$

$$
\begin{aligned}
G_1(\varphi) =& (2\pi)^{3/2}\varphi^2 - 47.933390\varphi^4 + 63.665987\varphi^6 - 50.70880\varphi^8 + 26.66807\varphi^{10} \\
& - 6.0205\varphi^{12} - 7.314\varphi^{14} + 10.947\varphi^{16} - 2.85\varphi^{18} - 13.7\varphi^{20} + o\left(\varphi^{22}\right) \\
G_2(\varphi) =& -2\sqrt{2\pi}\varphi + 12\sqrt{2\pi}\varphi^3 - 59.565733\varphi^5 + 61.174444\varphi^7 - 39.90249\varphi^9 \\
& + 15.6222\varphi^{11} + 3.0343\varphi^{13} - 12.781\varphi^{15} + 9.69\varphi^{17} + 6.62\varphi^{19} + o\left(\varphi^{21}\right)
\end{aligned}
\tag{A.2}
$$

where the unit of $\pi\varphi$ is in radians.

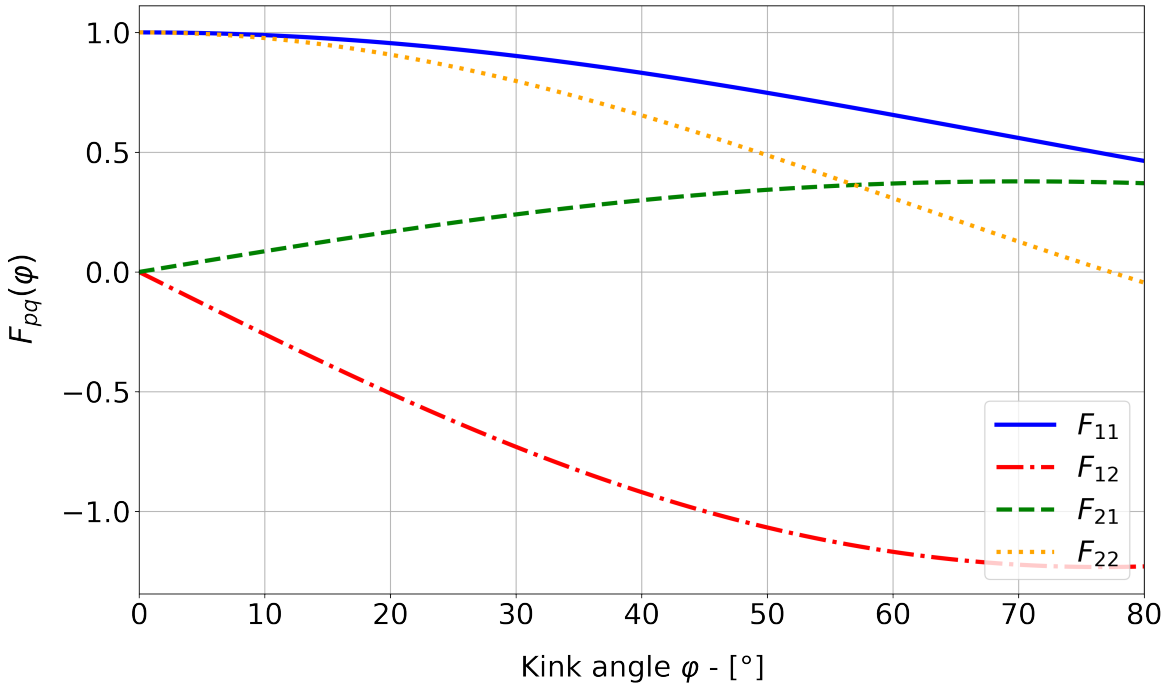

Figure A.1 Function of $F_{pq}(\varphi)$ with respect to the kink angle φ

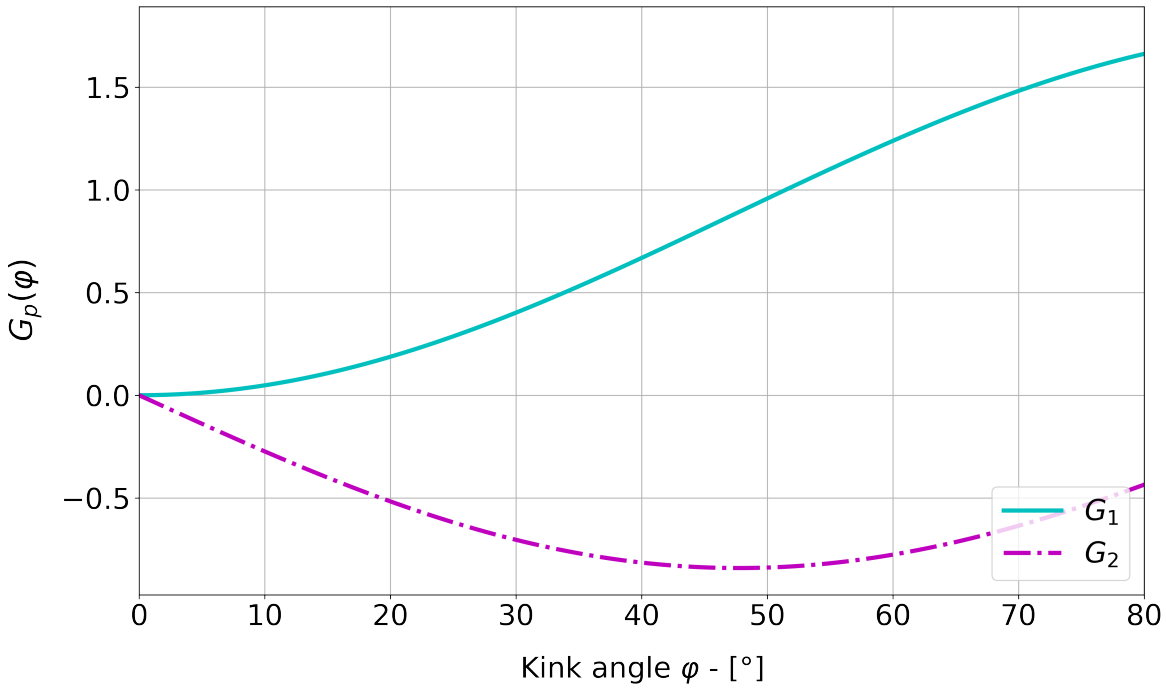

Figure A.2 Function of $G_p(\varphi)$ with respect to the kink angle φ

Appendix B

Python code for extracting near crack tip outer shell in Gcode

```
filename = "CT1.gcode"
#poisition of the nozzle : X 150, Y 145 (the nozzle begins at lower
   side of the crack tip)
phrase      = ";TYPE:WALL-OUTER"
line_number = []
read_file   = open(filename,"r")
# get the linenumber (outlayer at crack tip)
for number, line in enumerate(read_file):
    if phrase in line:
        line_number.append(number+10)
read_file.close()

print(line_number)
len(line_number)

#remove all the lines
with open(filename, "r") as infile:
    lines = infile.readlines()
with open(filename, "w") as outfile:
    for pos, line_ in enumerate(lines):
        if pos not in line_number:
            outfile.write(line_)
```

Listing B.1 Python example

Bibliography

Abaqus (2023). Page | Abaqus. https://www.3ds.com/products-services/simulia/products/abaqus/.

Abdollahi, A. and Arias, I. (2012). Phase-field modeling of crack propagation in piezoelectric and ferroelectric materials with different electromechanical crack conditions. *Journal of the Mechanics and Physics of Solids*, 60(12):2100–2126.

Ahn, S., Montero, M., Odell, D., Roundy, S., and Wright, P. K. (2002). Anisotropic material properties of fused deposition modeling ABS. *Rapid Prototyping Journal*, 8(4):248–257. Publisher: MCB UP Ltd.

Alessi, R. (2013). *Variational approach to fracture mechanics with plasticity.* These de doctorat, Palaiseau, Ecole polytechnique.

Alessi, R., Marigo, J. J., and Vidoli, S. (2015). Gradient damage models coupled with plasticity: Variational formulation and main properties. *Mechanics of Materials*, 80(PB):351–367.

Aliheidari, N., Christ, J., Tripuraneni, R., Nadimpalli, S., and Ameli, A. (2018). Interlayer adhesion and fracture resistance of polymers printed through melt extrusion additive manufacturing process. *Materials & Design*, 156:351–361. Publisher: Elsevier.

Allum, J., Moetazedian, A., Gleadall, A., and Silberschmidt, V. V. (2020). Interlayer bonding has bulk-material strength in extrusion additive manufacturing: New understanding of anisotropy. *Additive Manufacturing*, 34:101297. Publisher: Elsevier.

Ambati, M., Gerasimov, T., and De Lorenzis, L. (2015). Phase-field modeling of ductile fracture. *Computational Mechanics*, 55(5):1017–1040.

Ambrosio, L. and Tortorelli, V. M. (1990). Approximation of functional depending on jumps by elliptic functional via t-convergence. *Communications on Pure and Applied Mathematics*, 43:999–1036.

Amestoy, M. and Leblond, J. B. (1992). Crack paths in plane situations-II. Detailed form of the expansion of the stress intensity factors. *International Journal of Solids and Structures*, 29(4):465–501.

Ashby, M. F. (1989). Overview No. 80: On the engineering properties of materials. *Acta Metallurgica*, 37(5):1273–1293.

ASTM (1820). Standard test method for measurement of fracture toughness. Standard, American Society for Testing and Materials.

Ayatollahi, M. R., Nabavi-Kivi, A., Bahrami, B., Yazid Yahya, M., and Khosravani, M. R. (2020). The influence of in-plane raster angle on tensile and fracture strengths of 3D-printed PLA specimens. *Engineering Fracture Mechanics*, 237:107225.

Ayatollahi, M. R., Rashidi Moghaddam, M., Razavi, S. M., and Berto, F. (2016). Geometry effects on fracture trajectory of PMMA samples under pure mode-I loading. *Engineering Fracture Mechanics*, 163:449–461. Publisher: Elsevier Ltd.

Ayatollahi, M. R., Razavi, S. M. J., Rashidi Moghaddam, M., and Berto, F. (2015). Mode I Fracture Analysis of Polymethylmetacrylate Using Modified Energy-Based Models. *Physical Mesomechanics 2015 18:4*, 18(4):326–336. Publisher: Springer.

Bleyer, J. and Alessi, R. (2018). Phase-field modeling of anisotropic brittle fracture including several damage mechanisms. *Computer Methods in Applied Mechanics and Engineering*, 336:213–236. Publisher: Elsevier B.V.

Bonnet, d. M. and Frangi, A. (2007). Analyse des solides déformables par la méthode des éléments finis. *European Journal of Computational Mechanics*, 16(5):667–668.

Borden, M. J., Hughes, T. J., Landis, C. M., and Verhoosel, C. V. (2014). A higher-order phase-field model for brittle fracture: Formulation and analysis within the isogeometric analysis framework. *Computer Methods in Applied Mechanics and Engineering*, 273:100–118. Publisher: North-Holland.

Bourdin, B. (1998). *Une méthode variationelle en mécanique de la rupture*. PhD thesis, Université paris-nord.

Bourdin, B., Francfort, G. A., and Marigo, J. J. (2000). Numerical experiments in revisited brittle fracture. *Journal of the Mechanics and Physics of Solids*, 48:797–826.

Bourdin, B., Francfort, G. A., and Marigo, J. J. (2008). The variational approach to fracture. *The Variational Approach to Fracture*, pages 1–164. Publisher: Springer Netherlands ISBN: 9781402063947.

Bourdin, B., Larsen, C. J., and Richardson, C. L. (2011). A time-discrete model for dynamic fracture based on crack regularization. *International Journal of Fracture*, 168(2):133–143.

Bourdin, B., Marigo, J. J., Maurini, C., and Sicsic, P. (2014). Morphogenesis and propagation of complex cracks induced by thermal shocks. *Physical Review Letters*, 112(1):014301.

Bower, A. F. (2009). Applied mechanics of solids. *Applied Mechanics of Solids*, pages 1–795.

Brach, S. (2020). Effects of plasticity on the anisotropy of the effective fracture toughness. *International Journal of Fracture*, 226:181–196.

Brach, S., Hossain, M. Z., Bourdin, B., and Bhattacharya, K. (2019a). Anisotropy of the effective toughness of layered media. *Journal of the Mechanics and Physics of Solids*, 131:96–111.

Brach, S., Hossain, M. Z., Bourdin, B., and Bhattacharya, K. (2019b). Anisotropy of the effective toughness of layered media. *Journal of the Mechanics and Physics of Solids*, 131:96–111. Publisher: Pergamon.

Braides, A. (1998). *Approximation of Free-Discontinuity Problems*, volume 1694 of *Lecture Notes in Mathematics*. Springer, Berlin, Heidelberg.

Burger, M., Esposito, T., and Zeppieri, C. I. (2015). Second-Order Edge-Penalization in the Ambrosio–Tortorelli functional. *Multiscale Modeling & Simulation*, 13(4):1354–1389.

Cantrell, J., Rohde, S., Damiani, D., Gurnani, R., DiSandro, L., Anton, J., Young, A., Jerez, A., Steinbach, D., Kroese, C., and Ifju, P. (2017). Experimental Characterization of the Mechanical Properties of 3D Printed ABS and Polycarbonate Parts. In Yoshida, S., Lamberti, L., and Sciammarella, C., editors, *Advancement of Optical Methods in Experimental Mechanics, Volume 3*, Conference Proceedings of the Society for Experimental Mechanics Series, pages 89–105, Cham. Springer International Publishing.

Cavuoto, R., Lenarda, P., Misseroni, D., Paggi, M., and Bigoni, D. (2022). Failure through crack propagation in components with holes and notches: An experimental assessment of the phase field model. *International Journal of Solids and Structures*, 257:111798.

Chambolle, A., Francfort, G. A., and Marigo, J. J. (2009). When and how do cracks propagate? *Journal of the Mechanics and Physics of Solids*, 57(9):1614–1622.

Chen, C.-H., Cambonie, T., Lazarus, V., Nicoli, M., Pons, A., and Karma, A. (2015). Crack Front Segmentation and Facet Coarsening in Mixed-Mode Fracture. *Physical Review Letters*, 115(26):265503. arXiv:1509.05077 [cond-mat].

Chen, F. H. and Shield, R. T. (1977). Conservation laws in elasticity of the J-integral type. *Zeitschrift für angewandte Mathematik und Physik ZAMP*, 28(1):1–22.

Chen, L., Li, B., and de Borst, R. (2021). The use of Powell-Sabin B-Splines in a higher-order phase-field model for crack kinking. *Computational Mechanics*, 67(1):127–137.

Corre, T. and Lazarus, V. (2021). Kinked crack paths in polycarbonate samples printed by fused deposition modelling using criss-cross patterns. *International Journal of Fracture*.

Cotterell, B. and Rice, J. (1980). Slightly curved or kinked cracks. *International Journal of Fracture 1980 16:2*, 16(2):155–169.

cqadmin (2015). Stratasys 3D Printing Keeps NASA Satellite On Time and On Budget – FDM Strong Enough for Space. Section: 3D Printing / Additive Mfg.

Destuynder, P., Djaoua, P. E. M., Chesnay, L., and Nedelec, J. C. (1981). Sur une Interprétation Mathématique de l'Intégrale de Rice en Théorie de la Rupture Fragile. *Mathematical Methods in the Applied Sciences*, 3(1):70–87.

Erdogan, F. and Sih, G. C. (1963). On the Crack Extension in Plates Under Plane Loading and Transverse Shear. *Journal of Basic Engineering*, 85(4):519–525.

FEniCS (2022). FEniCS | FEniCS Project. https://fenicsproject.org/.

Fonseca, I. (1992). Lower semicontinuity of surface energies. *Proceedings of the Royal Society of Edinburgh: Section A Mathematics*, 120(1-2):99–115.

Francfort, G. A. and Marigo, J. J. (1998). Revisiting brittle fracture as an energy minimization problem. *Journal of the Mechanics and Physics of Solids*, 46:1319–1342.

Gardan, J., Makke, A., and Recho, N. (2018). Improving the fracture toughness of 3D printed thermoplastic polymers by fused deposition modeling. *International Journal of Fracture*, 210(1-2):1–15. Publisher: Springer Science and Business Media B.V.

Gechev, T. (2022). A short review of 3D printing methods used in the automotive industry.

Goldstein, R. V. and Salganik, R. L. (1974). Brittle fracture of solids with arbitrary cracks. *International Journal of Fracture*, 10(4):507–523.

Griffith, A. A. (1921). Vi. the phenomena of rupture and flow in solids. *Philosophical Transactions of the Royal Society of London. Series A, Containing Papers of a Mathematical or Physical Character*, 221:163–198.

Grossman-Ponemon, B. E., Mesgarnejad, A., and Karma, A. (2022). Phase-field modeling of continuous fatigue via toughness degradation. *Engineering Fracture Mechanics*, 264:108255.

Gupta, M., Alderliesten, R. C., and Benedictus, R. (2015). A review of T-stress and its effects in fracture mechanics. *Engineering Fracture Mechanics*, 134:218–241. Publisher: Elsevier Ltd.

Hakim, V. and Karma, A. (2005). Crack path prediction in anisotropic brittle materials. *Physical Review Letters*, 95(23):235501.

Hakim, V. and Karma, A. (2009). Laws of crack motion and phase-field models of fracture. *Journal of the Mechanics and Physics of Solids*, 57(2):342–368.

Hale, J. S., Brunetti, M., Bordas, S. P., and Maurini, C. (2018). Simple and extensible plate and shell finite element models through automatic code generation tools. *Computers & Structures*, 209:163–181.

Hossain, M. Z., Hsueh, C. J., Bourdin, B., and Bhattacharya, K. (2014). Effective toughness of heterogeneous media. *Journal of the Mechanics and Physics of Solids*, 71:15–32.

Hussain, M., Pu, S., and Underwood, J. (1973). Strain energy release rate for a crack under combined mode i and mode ii. *National Symposium on Fracture Mechanics*, pages 2–28.

Ingraffea, A. R. and Saouma, V. (1985). NUMERICAL MODELING OF DISCRETE CRACK PROPAGATION IN REINFORCED AND PLAIN CONCRETE. *Fract Mech of Concr, Struct Appl and Numer Calc*, pages 171–225. Publisher: Martinus Nijhoff Publ ISBN: 9024729602.

Irwin, G. R. (1957). Analysis of stresses and strains near the end of a crack traversing a plate. *Journal of Applied Mechanics*, 24:361–364.

Karma, A., Kessler, D. A., and Levine, H. (2001). Phase-field model of mode iii dynamic fracture. *Physical Review Letters*, 87:045501.

Kfouri, A. P. (1986). Some evaluations of the elastic T-term using Eshelby's method. *International Journal of Fracture*, 30(4):301–315.

Khosravani, M. R., Berto, F., Ayatollahi, M. R., and Reinicke, T. (2020). Fracture behavior of additively manufactured components: A review. *Theoretical and Applied Fracture Mechanics*, 109:102763. Publisher: Elsevier.

Kim, A., Bosnyak, C. P., and Chudnovsky, A. (1994). Effects of weathering, scale, and rate of loading on polycarbonate fracture toughness. *Journal of Applied Polymer Science*, 51(11):1841–1848. _eprint: https://onlinelibrary.wiley.com/doi/pdf/10.1002/app.1994.070511101.

Kizhakkinan, U., Rosen, D. W., and Raghavan, N. (2022). Experimental investigation of fracture toughness of fused deposition modeling 3D-printed PLA parts. *Materials Today: Proceedings*, 70:631–637. Publisher: Elsevier Ltd.

Le, J.-L., Manning, J., and Labuz, J. F. (2014). Scaling of fatigue crack growth in rock. *International Journal of Rock Mechanics and Mining Sciences*, 72:71–79.

Leblond, J. B. (1989). Crack paths in plane situations—I. General form of the expansion of the stress intensity factors. *International Journal of Solids and Structures*, 25(11):1311–1325.

Leevers, P. S. and Radon, J. C. (1982). Inherent stress biaxiality in various fracture specimen geometries. *International Journal of Fracture*, 19(4):311–325.

León Baldelli, A. A., Babadjian, J. F., Bourdin, B., Henao, D., and Maurini, C. (2014). A variational model for fracture and debonding of thin films under in-plane loadings. *Journal of the Mechanics and Physics of Solids*, 70(1):320–348.

León Baldelli, A. A., Bourdin, B., Marigo, J. J., and Maurini, C. (2013). Fracture and debonding of a thin film on a stiff substrate: Analytical and numerical solutions of a one-dimensional variational model. *Continuum Mechanics and Thermodynamics*, 25(2-4):243–268.

León Baldelli, A. A. and Maurini, C. (2021). Numerical bifurcation and stability analysis of variational gradient-damage models for phase-field fracture. *Journal of the Mechanics and Physics of Solids*, 152:104424.

Li, B. and Maurini, C. (2019). Crack kinking in a variational phase-field model of brittle fracture with strongly anisotropic surface energy. *Journal of the Mechanics and Physics of Solids*, 125:502–522.

Li, B., Peco, C., Millán, D., Arias, I., and Arroyo, M. (2015). Phase-field modeling and simulation of fracture in brittle materials with strongly anisotropic surface energy. *International Journal for Numerical Methods in Engineering*, 102(3-4):711–727.

Li, T., Marigo, J. J., Guilbaud, D., and Potapov, S. (2016). Gradient damage modeling of brittle fracture in an explicit dynamics context. *International Journal for Numerical Methods in Engineering*, 108(11):1381–1405.

Maloch, J., Hnátková, E., Žaludek, M., and Krátký, P. (2018). Effect of processing parameters on mechanical properties of 3D printed samples. *Materials Science Forum*, 919:230–235.

Mandal, T. K., Nguyen, V. P., and Wu, J. Y. (2022). On a new high order phase field model for brittle and cohesive fracture: numerical efficiency, length scale convergence and crack kinking. *Computational Materials Science*, 203:111079. Publisher: Elsevier.

Marigo, J.-J. (2010). Initiation of Cracks in Griffith's Theory: An Argument of Continuity in Favor of Global Minimization. *Journal of Nonlinear Science*, 20(6):831–868.

Marigo, J.-J. (2023). La mécanique de l'endommagement au secours de la mécanique de la rupture: l'évolution de cette idée en un demi-siècle. *Comptes Rendus. Mécanique*, 351(S3):1–21.

Marșavina, L., Vălean, C., Mărghitaș, M., Linul, E., Razavi, S. M. J., Berto, F., and Brighenti, R. (2022). Effect of the manufacturing parameters on the tensile and fracture properties of FDM 3D-printed PLA specimens. *Engineering Fracture Mechanics*, 274. Publisher: Elsevier Ltd.

Maurini, C., Bourdin, B., Gauthier, G., and Lazarus, V. (2013). Crack patterns obtained by unidirectional drying of a colloidal suspension in a capillary tube: Experiments and numerical simulations using a two-dimensional variational approach. *International Journal of Fracture*, 184(1-2):75–91.

McLouth, T. D., Severino, J. V., Adams, P. M., Patel, D. N., and Zaldivar, R. J. (2017). The impact of print orientation and raster pattern on fracture toughness in additively manufactured ABS. *Additive Manufacturing*, 18:103–109. Publisher: Elsevier.

Mesgarnejad, A., Bourdin, B., and Khonsari, M. M. (2013). A variational approach to the fracture of brittle thin films subject to out-of-plane loading. *Journal of the Mechanics and Physics of Solids*, 61(11):2360–2379.

Mesgarnejad, A., Imanian, A., and Karma, A. (2019). Phase-field models for fatigue crack growth. *Theoretical and Applied Fracture Mechanics*, 103:102282.

Mesgarnejad, A., Pan, C., Erb, R. M., Shefelbine, S. J., and Karma, A. (2020). Crack path selection in orientationally ordered composites. *Physical Review E*, 102(1):013004.

Molnár, G., Doitrand, A., Estevez, R., and Gravouil, A. (2020). Toughness or strength? Regularization in phase-field fracture explained by the coupled criterion. *Theoretical and Applied Fracture Mechanics*, 109:102736.

Moës, N., Dolbow, J., and Belytschko, T. (1999). A FINITE ELEMENT METHOD FOR CRACK GROWTH WITHOUT REMESHING. *INTERNATIONAL JOURNAL FOR NUMERICAL METHODS IN ENGINEERING Int. J. Numer. Meth. Engng*, 46:131–150.

Mumford, D. and Shah, J. (1989). Optimal approximations by piecewise smooth functions and associated variational problems. *Communications on Pure and Applied Mathematics*, 42:577–685.

Negri, M. (2020). Gamma-convergence for high order phase field fracture: Continuum and isogeometric formulations. *Computer Methods in Applied Mechanics and Engineering*, 362:112858.

Ngo, T. D., Kashani, A., Imbalzano, G., Nguyen, K. T., and Hui, D. (2018). Additive manufacturing (3d printing): A review of materials, methods, applications and challenges. *Composites Part B: Engineering*, 143:172–196.

Nguyen, T. T., Réthoré, J., and Baietto, M. C. (2017). Phase field modelling of anisotropic crack propagation. *European Journal of Mechanics, A/Solids*, 65:279–288.

Ortega, A., Maimí, P., González, E. V., and Ripoll, L. (2014). Compact tension specimen for orthotropic materials. *Composites Part A: Applied Science and Manufacturing*, 63:85–93.

Owen, D. R. J. and Fawkes, A. J. (1983). *Engineering fracture mechanics: numerical methods and applications*. Pineridge Press, Swansea, U.K.

ParaView (2023). ParaView - Open-source, multi-platform data analysis and visualization application. https://www.paraview.org/.

Pham, K., Amor, H., Marigo, J.-J., and Maurini, C. (2011). Gradient Damage Models and Their Use to Approximate Brittle Fracture. *International Journal of Damage Mechanics*, 20(4):618–652.

Pham, K. H., Ravi-Chandar, K., and Landis, C. M. (2017). Experimental validation of a phase-field model for fracture. *International Journal of Fracture*, 205:83–101.

Réthoré, J. (2015). Automatic crack tip detection and stress intensity factors estimation of curved cracks from digital images. *International Journal for Numerical Methods in Engineering*, 103(7):516–534.

Rezaeian, P., Ayatollahi, M. R., Nabavi-Kivi, A., and Mohammad Javad Razavi, S. (2022). Effect of printing speed on tensile and fracture behavior of ABS specimens produced by fused deposition modeling. *Engineering Fracture Mechanics*, 266:108393. Publisher: Pergamon.

Rice, J. R. (1968). A Path Independent Integral and the Approximate Analysis of Strain Concentration by Notches and Cracks. *Journal of Applied Mechanics*, 35(2):379–386.

Roux, S., Réthoré, J., and Hild, F. (2009). Digital image correlation and fracture: An advanced technique for estimating stress intensity factors of 2D and 3D cracks. *Journal of Physics D: Applied Physics*, 42(21).

Scherer, J.-M., Brach, S., and Bleyer, J. (2022). An assessment of anisotropic phase-field models of brittle fracture. *Computer Methods in Applied Mechanics and Engineering*, 395:115036.

Schreiber, C., Kuhn, C., Müller, R., and Zohdi, T. (2020). A phase field modeling approach of cyclic fatigue crack growth. *International Journal of Fracture*, 225(1):89–100.

Sekerka, R. F. (2005). Analytical criteria for missing orientations on three-dimensional equilibrium shapes. In *Journal of Crystal Growth*, volume 275, pages 77–82. North-Holland. Issue: 1-2 ISSN: 00220248.

Shanmugam, V., Das, O., Babu, K., Marimuthu, U., Veerasimman, A., Johnson, D. J., Neisiany, R. E., Hedenqvist, M. S., Ramakrishna, S., and Berto, F. (2021). Fatigue behaviour of FDM-3D printed polymers, polymeric composites and architected cellular materials. *International Journal of Fatigue*, 143:106007. Publisher: Elsevier.

Sih, G. C. (1974). Strain-energy-density factor applied to mixed mode crack problems. *International Journal of Fracture*, 10(3):305–321.

Singh, D., Singh, R., and Boparai, K. S. (2018). Development and surface improvement of FDM pattern based investment casting of biomedical implants: A state of art review. *Journal of Manufacturing Processes*, 31:80–95.

Takei, A., Roman, B., Bico, J., Hamm, E., and Melo, F. (2013). Forbidden directions for the fracture of thin anisotropic sheets: An analogy with the wulff plot. *Physical Review Letters*, 110:144301.

Tanné, E., Li, T., Bourdin, B., Marigo, J. J., and Maurini, C. (2018). Crack nucleation in variational phase-field models of brittle fracture. *Journal of the Mechanics and Physics of Solids*, 110:80–99.

Teichtmeister, S., Kienle, D., Aldakheel, F., and Keip, M. A. (2017). Phase field modeling of fracture in anisotropic brittle solids. *International Journal of Non-Linear Mechanics*, 97:1–21. Publisher: Elsevier Ltd.

Timoshenko, S. and Goodier, J. (1951). *Theory of Elasticity*. McGraw-Hill Book Company, 2 edition.

Triclot, J., Corre, T., Gravouil, A., and Lazarus, V. (2023). Key role of boundary conditions for the 2D modeling of crack propagation in linear elastic Compact Tension tests. *Engineering Fracture Mechanics*, 277:109012.

Williams, M. L. (1952). Stress Singularities Resulting From Various Boundary Conditions in Angular Corners of Plates in Extension. *Journal of Applied Mechanics*, 19(4):526–528.

Wilson, Z. A. and Landis, C. M. (2016). Phase-field modeling of hydraulic fracture. *Journal of the Mechanics and Physics of Solids*, 96:264–290.

Wu, J. Y. and Chen, W. X. (2021). Phase-field modeling of electromechanical fracture in piezoelectric solids: Analytical results and numerical simulations. *Computer Methods in Applied Mechanics and Engineering*, 387:114125.

Wu, J. Y., Nguyen, V. P., Nguyen, C. T., Sutula, D., Sinaie, S., and Bordas, S. P. (2020). *Phase-field modeling of fracture*, volume 53. Academic Press Inc.

Xia, L., Yvonnet, J., and Ghabezloo, S. (2017). Phase field modeling of hydraulic fracturing with interfacial damage in highly heterogeneous fluid-saturated porous media. *Engineering Fracture Mechanics*, 186:158–180.

Xu, Z. K., Wang, B., Zhang, P., and Zhang, Z. F. (2021). Short fatigue crack growth behavior in 18Ni marageing steel. *Materials Science and Engineering: A*, 807:140844.

Yau, J. F., Wang, S. S., and Corten, H. T. (1980). A Mixed-Mode Crack Analysis of Isotropic Solids Using Conservation Laws of Elasticity. *Journal of Applied Mechanics*, 47(2):335–341.

Yu, H. and Kuna, M. (2021). Interaction integral method for computation of crack parameters K–T – A review. *Engineering Fracture Mechanics*, 249:107722.

Zou, R., Xia, Y., Liu, S., Hu, P., Hou, W., Hu, Q., and Shan, C. (2016). Isotropic and anisotropic elasticity and yielding of 3D printed material. *Composites Part B: Engineering*, 99:506–513. Publisher: Elsevier Ltd.

ECOLE DOCTORALE

Titre : Propagation de fissures dans des milieux élastiques avec énergie de surface anisotrope : expériences, simulations numériques et mécanique de la rupture élastique linéaire

Mots clés : Fabrication additive, Rupture, Champ de phase, Energies surface anisotropie

Résumé : La fabrication additive attire une attention croissante en raison de ses avantages en termes de flexibilité de modélisation et de facilité de conception de microstructures complexes. Nous avons constaté qu'en manipulant la stratégie d'impression, les échantillons imprimés par dépôt de fusion de polycarbonate peuvent présenter un comportement fortement anisotrope en termes de résistance à la rupture, tout en conservant des propriétés isotropes en termes d'élasticité.
Le focus de cette thèse est d'explorer le comportement en matière de rupture dans des milieux élastiques isotropes présentant une ténacité de rupture anisotrope, en utilisant une combinaison d'investigations expérimentales et de simulations numériques. Dans la partie expérimentale, nous examinons la propagation des fissures dans diverses conditions de chargement en utilisant des géométries d'échantillons variées, englobant à la fois le Mode I et le Mode I+II. Dans la partie numérique, nous adoptons la modélisation de la fissuration fragile par champ de phase basée sur l'approche variationnelle, en utilisant des données expérimentales pour l'étalonnage et l'identification des paramètres numériques. À travers ces méthodologies complètes, notre objectif est de favoriser une compréhension plus profonde de l'interaction entre les motifs d'impression et la sélection des trajectoires de fissures. Cette compréhension a des implications significatives pour guider et gérer la propagation des fissures dans les composants fabriqués par fabrication additive. De plus, nous adoptons les critères classiques basés sur le taux de restitution d'énergie maximale généralisé pour améliorer notre compréhension de la sélection des trajectoires de fissures et de la force critique correspondante.
Dans la dernière partie de cette thèse, nous présentons quelques investigations préliminaires concernant l'éventuelle émergence d'un motif de fissure en Zig-Zag dans des spécimens imprimés en 3D. De plus, nous plongeons en profondeur dans le comportement de rupture des spécimens imprimés sous chargement cyclique, offrant une comparaison exhaustive entre les observations expérimentales et les prévisions numériques.

Title : Crack propagation in elastic media with anisotropic surface energy : experiments, numerical simulations and linear elastic fracture mechanics

Keywords : Additive manufacturing, Fracture, Phase field modeling of brittle fracture, Anisotropic surface energy

Abstract : Additive manufacturing is receiving increasing attention due to its advantages in terms of modelling flexibility and allowing to easily design complex micro-structures. Through the manipulation of the printing strategy, we observed that fused deposition of polycarbonate can result in printed samples showcasing a distinct anisotropic behavior in fracture toughness, all the while retaining isotropic properties in elasticity.
This thesis is dedicated to investigating fracture behavior within isotropic elastic media with anisotropic fracture toughness. The approach involves a combination of fracture experiments and numerical simulations. In the experimental part, we examine crack propagation under various loading conditions using diverse sample geometries, encompassing both Mode I and Mode I+II loading condition. In the numerical part, we adopt the phase-field modeling of brittle fracture based on a variational approach, using experimental data for calibrating and identification of the numerical parameters. Through these comprehensive methodologies, our objective is to foster a deeper comprehension of the interplay between printing patterns and the selection of crack paths. This understanding holds significant implications for guiding and controlling crack propagation in additive manufacturing-produced components. Besides, we adopted the classical based criteria Generalized Maximum Energy Release Rate to enhance our understanding of crack path selection and the relevant critical force.
In the last part of this thesis, we presents some preliminary investigations regarding the potential emergence of Zig-Zag crack patterns in 3D printed specimens. Additionally, we delve extensively into the fracture behavior of printed specimens under cyclic loading, offering a comprehensive comparison between experimental observations and numerical forecasts.

Institut Polytechnique de Paris
91120 Palaiseau, France